The influence of trees on air quality in a street canyon

Investigating the effect of leaf area density and seasonality on the dispersion of particulate matter emitted in a street canyon

Master thesis

Simon van der Windt

TU Delft

The influence of trees on air quality in a street canyon

Investigating the effect of leaf area density and seasonality on the dispersion of particulate matter emitted in a street canyon

by

Simon van der Windt

Student Name	Student Number
Simon van der Windt	5102316

Supervisors S. van der Linden, C. García-Sánchez, A. Patil, J. Sousa

Date Thursday 8th January, 2026
Faculty: Faculty of Civil Engineering and Geosciences, Delft

TU Delft

Abstract

Long-term exposure to hazardous pollutants in the air is a problem in urban areas all over the world. In European countries, where regulations have been sharpened over the years, an estimated 200,000 to 300,000 people die prematurely every year due to bad air quality. Many more people experience negative health effects, like respiratory and cardiovascular diseases. In the Netherlands as well, air quality has improved over the years. Yet still, most of the country exceeds the WHO standards for most pollutants. In an effort to bring the negative impact of air pollution down to 0, many urban planners suggest planting trees as a potential mitigation strategy. However, the impact of trees on air quality is not fully understood.

This thesis investigates how the leaf area density or LAD of trees in a street canyon affects the dispersion of pollutants emitted in said canyon. It does so with a Reynolds-Averaged Navier-Stokes model in the OpenFOAM v7 software. A street canyon with an aspect ratio of 1:1 is considered, with a row of trees running through the middle. For four different LAD values, the impacts on canyon concentrations are examined. The results for mean concentrations on the facades and within the canyon are computed and visualised for three different wind directions: one parallel to the canyon, one perpendicular to the canyon, and one at a 45° angle. This was also done for multiple street lengths to investigate the impact of the street boundaries.

The results for this LAD investigation are used to determine monthly averages and seasonal effects. Therefore, the results are subjected to daily KNMI meteorological data. This method utilises wind parameters, direction and speed, to estimate canyon concentrations. Two different types of trees are considered: deciduous trees, which lose their leaves in winter, and coniferous trees, which are evergreens.

It is found that an increase in LAD causes an increase in pollution for parallel wind and angled wind, especially near the boundaries. This is mainly due to the reduced wind speeds within the canyon, limiting dilution. For parallel wind, recirculation zones caused by trees cause the canyon concentrations to accumulate. For perpendicular wind, lower pollutant concentrations are found with higher LAD, due to enhanced vertical transport and reduced accumulation resulting from limited lateral transport.

The seasonal impact of deciduous and coniferous trees is very LAD-dependent when taking yearly averages. Depending on the chosen LAD value, deciduous trees are up to 17-23% worse than a case with no trees, and coniferous trees are up to 28-36% worse, although for low LAD values the impact is small.

Nomenclature

Abbreviations

Abbreviation	Description
CFD	Computational Fluid Dynamics
DNS	Direct Numerical Simulation
LES	Large Eddy Simulation
RANS	Reynolds-Averaged Navier-Stokes
$PM_{2.5}$	Particulate matter of diameter <2.5 μm

Table 1: Abbreviations with their descriptions

Symbols

Symbol	Units	Description
U	$m \cdot s^{-1}$	Flow velocity vector
t	s	Time
ρ	$kg \cdot m^{-3}$	Air density
p	$m^2 \cdot s^{-2}$	Pressure divided by air density
ν	m^2/s	Viscosity
ν_t	$m^2 \cdot s^{-1}$	Turbulent viscosity
k	$m^2 \cdot s^{-2}$	Turbulent kinetic energy
ε	$m^2 \cdot s^{-3}$	Turbulent kinetic energy dissipation rate
$S_{U_i}, S_k, S_\varepsilon$	m/s	Source/sink terms for U_i, k and ε
C_d	–	Leaf drag coefficient
LAD	m^2/m^3	Leaf area density
κ	–	Von Karman constant (=0.41)
C	$kg \cdot m^{-3}$	Pollutant concentration
$U_{C,eff}$	$m \cdot s^{-1}$	Effective velocity vector of pollutant C
S_C	$kg/m^3/s$	Source of pollutant
$Sc_{(t)}$	–	(Turbulent) Schmidt number
J	$kg/m^3 \cdot m/s$	Mass flux of pollutants
C_e, C_w	$kg \cdot m^{-3}$	Concentration of the pollutants emitted on the eastern/western side of the trees

Table 2: Symbols with their respective units and descriptions

Contents

1 Introduction

1.1. Problem Introduction

Over 57% of people live in urban environments, and the number is still growing (Our World in Data, 2025). Most cities are coping with bad air quality. Long-term exposure to higher pollution has serious health effects, like respiratory diseases and cardiovascular diseases, and it impacts people's organs (European Environment Agency, 2024c). Every 10 $\mu g/m^3$ increase in $PM_{2.5}$ results in 8% more air quality related hazards (J. Chen and Hoek, 2020; Weichenthal et al., 2022).

In Europe, an estimated 200,000 to 300,000 people die prematurely every year, of whom the death is attributed to air pollution-related causes (European Environment Agency, 2024b). Even though most cities have improved their air quality over the past years, with cleaner vehicles (RIVM, 2025c) and stricter regulations, 96% of the European urban population is still exposed to $PM_{2.5}$ levels above WHO guidelines (European Environment Agency, 2024a). For other pollutants like PM_{10}, O_3 and NO_2 the percentages are 83%, 94% and 88%, respectively (numbers from 2022) (European Environment Agency, 2024a).

In the Netherlands, the air in the whole country exceeds the WHO guidelines for $PM_{2.5}$ (RIVM, 2025b) and in most populated areas also for PM_{10} (RIVM, 2025a) and NO_2 (RIVM, 2025d). In general, air quality is the worst in densely populated areas. Many of these areas are also poorer neighbourhoods. Therefore, poor people are often prone to worse air quality (Venderbos, Hosper, and van Loenen, 2023). This problem is also found outside the Netherlands, like in Brussels (de Rooij, 2022), or in the US (Jbaily et al., 2022; Mikati et al., 2018; Bell and Ebisu, 2012; Rentschler and Leonova, 2022).

In their 'Pathway to a Healthy Planet for All', the European Union has formulated the target to reduce the health impact of air pollution by 55% by 2030 in terms of premature deaths (European Commission, 2021). By 2050, all water, air and soil pollution should be below harmful levels. Although prevention of pollution is stated as the most important way to achieve this goal, controlling the exposure of humans and the environment to pollution is also a key factor in minimising harm. This can be done through technical measures and solutions in the urban landscape, such as trees.

Most cities already plant trees for various reasons, mainly for aesthetic and climate reasons, but also for air quality (Wang and Akbari, 2016; European Urban Initiative, 2022; United States Environmental Protection Agency, 2024). However, the effect of trees on air quality is not properly understood. Trees can have positive effects on deposition, for example, where particles are taken out of the air onto the leaves. This is because the tree structure allows for a very high surface area per unit of volume. However, they also have aerodynamic effects that can negatively affect air quality (Vranckx et al., 2015). Trees form a barrier between the air inside and outside the street canyon (Vos et al., 2013). This can either worsen or improve air quality, depending on the type of source and aerodynamics (Grylls and van Reeuwijk, 2022). Turbulence-induced dispersion can be decreased (worsening air quality) or increased (improving air quality) by the presence of trees. Especially for lower wind speeds, trees have a negative effect (A. Jeanjean, Monks, and Leigh, 2016). These aerodynamic effects are suggested to be dominant with regard to air quality (Vos et al., 2013). Therefore, it is important to study this impact of trees more thoroughly. Quantifying the effects of different parameters is essential to design our urban landscapes better.

1.2. Research Question

Previous studies have researched the effect of trees in CFD models with idealised street canyons. Some of these include air quality, like studies by Vranckx et al. (2015) (RANS) and Grylls and van Reeuwijk (2022) (LES). Fu, Pađen, and García-Sánchez (2024) researches the effect of the level of detail in the model and LAD on wind speed. It does not incorporate air quality, but it provides the framework for street canyon flow influenced by the presence

of different types of trees. Similarly, Vos et al. (2013) have researched the effects of different vegetation types. These studies showed increased concentrations for $PM_{2.5}$. Jin et al. (2014) have also found this increase, but with on-site measurements, confirming the negative effect of trees on air quality under certain conditions. Some CFD studies use a real-life domain (an existing cityscape) like the one by A. Jeanjean, Monks, and Leigh (2016). They show that wind speed determines whether trees benefit air quality or not.

What is missing is a large-scale study with varying parameters, investigating their sensitivities and impacts. The first varied parameter is *leaf area density* (LAD), which is the area of leaves per unit of volume $\left(m^2/m^3\right)$. This research also distinguishes between two vegetation types: deciduous trees, which lose their leaves in winter, and coniferous trees, which do not. How these parameters influence the mass fluxes within a street canyon through aerodynamic alterations is still a subject about which little is known.

This thesis will focus on the question: ***How does urban vegetation impact local air quality in an urban environment?*** This question will be answered by investigating the effects of trees on dispersion in a Computational Fluid Dynamics (CFD) model that will be explained in chapter 2. Using this CFD model, the following sub-questions will be researched:

1. How great is the influence of Leaf Area Density (LAD) on locally emitted $PM_{2.5}$ levels?
2. What are the concentration differences between a case with deciduous trees and one with coniferous trees, considering seasonal changes?

1.3. Report structure

The report is structured as follows. chapter 2 describes the methods used for answering the research questions, including an explanation of the used model. The setup of the model and its parameters, and the decisions made for analysing the results are elaborated in chapter 3. The results from the model are shown in chapter 4. This includes an in-depth analysis, that will then be discussed in chapter 5. Finally, conclusions are drawn in chapter 6.

2
Methods

This research investigates the aerodynamic effects of trees using *Computational Fluid Dynamics* (CFD) modelling in OpenFOAM v7 (OpenCFD Ltd 2025 and KEYSIGHT, 2025). CFD allows for complex simulations that cannot be easily replicated in real-life experiments, such as wind tunnels, or solved analytically (G. Chen et al., 2014). It is expensive and can take decades for trees to grow, so gathering quantitative field data is hard. CFD modelling enables these calculations without the need for actual measurements. This comes at the cost of a lack of real-life data to substantiate the conclusions, but previous studies have verified the methods. OpenFOAM was chosen because it is a free software that provides flexible post-processing options.

2.1. Governing equations

The basic incompressible Navier-Stokes governing equations for momentum and mass are as follows:

$$\underbrace{\frac{\partial U_i}{\partial t}}_{\text{Storage}} + \underbrace{U_j \frac{\partial U_i}{\partial x_j}}_{\text{Advection}} = \underbrace{-\frac{1}{\rho}\frac{\partial p}{\partial x_i}}_{\text{Pressure gradient}} - \underbrace{\delta_{i3} g}_{\text{Gravity}} + \underbrace{\nu \frac{\partial^2 U_i}{\partial x_j^2}}_{\text{Viscous stress}} \tag{2.1}$$

$$\frac{\partial U_j}{\partial x_j} = 0 \tag{2.2}$$

The Navier-Stokes equations are based on Newton's second law ($F = ma$), applied to a fluid. The storage term describes the inertia of the air or its resistance to change in velocity. The advection term represents the bulk transport of momentum. The pressure gradient term describes the acceleration of air due to pressure differences. The gravity term g is multiplied by the Kronecker Delta function to result in only a downward acceleration. Lastly, the viscous stress term describes how fluid viscosity ν, which acts as an internal friction, causes diffusion in momentum.

These equations can only be solved analytically for very simple and idealised flows. For turbulent flow in an atmospheric environment, an alternative approach is necessary to perform calculations. There are three main ways to achieve this, all balancing accuracy (detail) with computing time.

- *Direct Numerical Simulation* (DNS)
- *Large Eddy Simulation* (LES)
- *Reynolds-Averaged Navier Stokes* (RANS)

DNS is the most computationally expensive simulation type. It is the only method that does not introduce additional approximations other than those from numerical algorithms (G. Chen et al., 2014). It resolves the equations for eddies down to the smallest scale, the Kolmogorov length scale, resulting in the most detailed solution. Solving for this scale requires a very fine grid and a large number of time steps, making it unfeasible for large-scale atmospheric applications (Schatzmann and Leitl, 2011; IdealSimulations, s.d.).

Like DNS, LES resolves the equations for eddies directly, but only the large ones. These large eddies have the most energy and are most dependent on geometries. Smaller eddies tend to be more similar to each other and can therefore be modelled (IdealSimulations, s.d.). LES applies a filter that cuts off turbulent scales smaller than a certain scale (G. Chen et al., 2014). This reduces computation times, since the smallest eddies are computationally

the most expensive and require the finest mesh (Fidelis, s.d.). LES obtains detailed results with a smaller computation time compared to DNS, which is why it is often used in academic contexts. Still, however, the computation times are too long for the scope of this study.

The last approach is RANS. RANS takes the time-averaged equations, drastically reducing computation times compared to DNS and LES, and introducing a Reynolds stress term to model turbulence (IdealSimulations, s.d.). This yields the least detailed results of the three, but has the advantage of flexibility, allowing for the comparison of many different scenarios with each other. Also, since air quality standards are typically based on a large timescale (years), the results do not need to be as detailed as possible. Mean flows are sufficient for engineering applications (IdealSimulations, s.d.). Due to the large amount of modelling, RANS is greatly dependent on empirical correlations (G. Chen et al., 2014). Another downside of (steady) RANS is the input of neutral boundary layer conditions, resulting in steady-state solutions. Although this is not a realistic assumption for the atmospheric boundary layer, which is inherently unsteady, steady RANS is very useful for time-averaged results. This is based on the assumption that, averaged over larger time scales, the solution is statistically steady (Schatzmann and Leitl, 2011). There are ways to implement unsteady conditions using URANS (Unsteady RANS), but this approach was not chosen. Due to the advantage of running more simulations, the inaccuracy is accepted, and the RANS solver was chosen.

2.2. Model

This section describes all of the equations and inputs for the OpenFOAM model. This work largely builds on previous work by Fu, Pađen, and García-Sánchez (2024). Equations, model constants, and parameters used in that paper are also used in this research.

2.2.1. Governing equations RANS

The RANS approach makes use of Reynolds decomposition. This method takes a variable, say U_i, and splits it in a time-averaged component $\overline{U_i}$ and a fluctuating component U_i':

$$U_i = \overline{U_i} + U_i' \tag{2.3}$$

such that:

$$\overline{U_i'} = 0 \tag{2.4}$$

Applying this decomposition to the incompressible Navier-Stokes equations and then time-averaging yields the following equations for conservation of momentum and mass:

$$\overline{U_j}\frac{\partial \overline{U_i}}{\partial x_j} = -\frac{1}{\rho}\frac{\partial \overline{p}}{\partial x_i} + \nu\frac{\partial^2 \overline{U_i}}{\partial x_j \partial x_j} - \frac{\partial \overline{U_i' U_j'}}{\partial x_j} + S_{U_i} \tag{2.5}$$

$$\frac{\partial \overline{U_j}}{\partial x_j} = 0 \tag{2.6}$$

Here, $\overline{U_i}$ represents the time-averaged velocity components, ρ is the air density, $\overline{p}$ is the time-averaged pressure, ν is the kinematic viscosity of air, and S_{U_i} is the source/sink term due to the presence of leaves. This will be further elaborated in subsection 2.2.2.

The second to last term in Equation 2.5 is $\overline{U_i' U_j'}$, which represents the Reynolds stress. This term for turbulent flow gives too many unknowns to solve with the limited number of equations we have, which is known as the closure problem. Therefore, it needs to be closed with a turbulence model. A $k-\varepsilon$ model is used (Launder and Spalding, 1974), as it is most widely utilized in atmospheric boundary layer models (Hargreaves and Wright, 2007). The Reynolds stress is first approximated using the Boussinesq hypothesis (Blazek, 2005):

$$\overline{U_i' U_j'} = \frac{2}{3}k\delta_{ij} - 2\mu_t \overline{S_{ij}} \tag{2.7}$$

Here, k is the turbulent kinetic energy and $\overline{S_{ij}}$ is the Reynolds-Averaged strain tensor, which is equal to:

$$\overline{S_{ij}} = \frac{1}{2}\left(\frac{\partial \overline{U_i}}{\partial x_j} + \frac{\partial \overline{U_j}}{\partial x_i}\right) \tag{2.8}$$

Turbulent dynamic viscosity μ_t is computed as:

$$\mu_t = \rho \nu_t \tag{2.9}$$

where:

$$\nu_t = C_\mu \frac{k^2}{\varepsilon} \tag{2.10}$$

where C_μ is equal to 0.09. The equations for turbulent kinetic energy k and turbulent dissipation rate ε in the $k-\varepsilon$ model are (Launder and Spalding, 1974):

$$\overline{U_j}\frac{\partial k}{\partial x_j} = \frac{\partial}{\partial x_j}\left[\left(\nu + \frac{\nu_t}{\sigma_k}\right)\frac{\partial k}{\partial x_j}\right] + P_k - \varepsilon + S_k \tag{2.11}$$

$$\overline{U_j}\frac{\partial \varepsilon}{\partial x_j} = \frac{\partial}{\partial x_j}\left[\left(\nu + \frac{\nu_t}{\sigma_\varepsilon}\right)\frac{\partial \varepsilon}{\partial x_j}\right] + C_{\varepsilon 1}\frac{\varepsilon}{k}P_k - C_{\varepsilon 2}\frac{\varepsilon^2}{k} + S_\varepsilon \tag{2.12}$$

Here, ν_t is turbulent kinematic viscosity, P_k is the turbulent production term for the generation of turbulence (Franklin, 2024) given by:

$$P_k = -\rho \overline{U_i' U_j'} \frac{\partial \overline{U_i}}{\partial x_j} \tag{2.13}$$

and σ_k, σ_ε, $C_{\varepsilon 1}$, and $C_{\varepsilon 2}$ are model constants equal to 1.0, 1.3, 1.44, and 1.92, respectively (Launder and Spalding, 1974). The source/sink terms for U_i, k and ε are given in subsection 2.2.2.

2.2.2. Adding trees

As stated, this research builds on previous work by Fu, Pađen, and García-Sánchez (2024). It makes use of the treeFoam solver for incompressible flow. Tree stems are modelled as impenetrable walls, whereas canopies are treated as porous zones with sink terms (S_{U_i}) and source terms (S_k and S_ε) representing tree drag in the momentum and turbulence equations. Equation 2.14 describes the sink term for momentum, and Equation 2.15 and Equation 2.16 describe the source/sink terms for turbulence (Kenjereš and ter Kuile, 2013). Whether the trees act as a source or sink for k and ε depends on the polarities of the values between the brackets.

$$S_{U_i} = -C_d \; LAD \; U_i \, |U_i| \tag{2.14}$$

$$S_k = C_d \; LAD \; \left(\beta_p |U_i|^3 - \beta_d \, |U_i| \, k\right) \tag{2.15}$$

$$S_\varepsilon = C_d \; LAD \left(C_{\varepsilon_4}\beta_p |U_i|^3 \frac{\varepsilon}{k} - C_{\varepsilon_5}\beta_d \, |U_i| \, \varepsilon\right) \tag{2.16}$$

Here, the drag coefficient C_d is set constant at 0.2 (Gromke, Blocken, et al., 2015). Some studies vary C_d with LAD for different vegetation types (Xue and Li, 2017), but for this study, only leaf area density LAD is altered to isolate its effects. U_i is the velocity component in the direction of x_i and $|U|$ is the magnitude of the wind speed vector. β_p is the fraction of mean kinetic energy that is converted into turbulent kinetic energy. Often, a value of 1 is used. β_d usually ranges between 4-6.5 and is set to be 5.1. It is the coefficient for the short-circuiting of turbulent cascade. C_{ε_4} and C_{ε_5} are model constants and are both set to 0.9. All of these parameters were chosen by Fu, Pađen, and García-Sánchez (2024) based on a report by Buccolieri et al. (2018).

2.2.3. Boundary conditions

For inflow in the neutral atmospheric boundary layer, the equations 2.17 to 2.19 are used. These assume no vertical velocity, constant pressure, and constant shear stress.

$$U(z) = \frac{u_*}{\kappa} \ln \frac{z - d + z_0}{z_0} \tag{2.17}$$

This wind velocity U is given a user-defined direction. u_* is calculated for reference velocity $U_{ref} = 4.97$ ms^{-1} at $z_{ref} = 10$ m height, which corresponds roughly to the mean wind speed measured at 10 m height in Rotterdam (KNMI, 2025; Fu, Pađen, and García-Sánchez, 2024). The von Karman constant κ is equal to 0.41. A roughness length $z_0 = 0.2$ m was chosen after Fu, Pađen, and García-Sánchez (2024), representing a roughly open to rough landscape according to the Davenport-Wieringa roughness classification, updated by Blocken (2015). Displacement height d is equal to 0. The inflow boundary conditions for k and ε after Patil and García-Sánchez (2025) are:

$$k(z) = \frac{{u_*}^2}{\sqrt{C_\mu}} \sqrt{C_{\varepsilon 1} \ln \left(\frac{z - d + z_0}{z_0} \right) + C_{\varepsilon 2}} \tag{2.18}$$

$$\varepsilon(z) = \frac{{u_*}^3}{\kappa \, (z - d + z_0)} \sqrt{C_{\varepsilon 1} \ln \left(\frac{z - d + z_0}{z_0} \right) + C_{\varepsilon 2}} \tag{2.19}$$

2.2.4. Scalar transport

The model was adjusted to include the transport of scalar C. The governing equation for the conservation of scalar quantities (Itokazu et al., 2025; A. P. Jeanjean et al., 2017) shown in Equation 2.20 contains a factor α_t:

$$\frac{\partial C}{\partial t} + U_j \frac{\partial C}{\partial x_j} = \alpha_t \frac{\partial^2 C}{\partial x_j^2} + S_C \tag{2.20}$$

This α_t is the effective diffusivity that is made up of a diffusion coefficient and an eddy diffusion coefficient (A. P. Jeanjean et al., 2017):

$$\alpha_t = \frac{\nu}{Sc} + \frac{\nu_t}{Sc_t} \tag{2.21}$$

Here, viscosity ν is divided by the molecular Schmidt number. Since there is no molecular diffusion taking place for solids like PM, the molecular Schmidt number Sc is set to 1.0, so this first term is just ν. The turbulent Schmidt number Sc_t varies between 0.2-1.3 in most studies (Tominaga and Stathopoulos, 2007). For a street canyon with an avenue of trees and the species $PM_{2.5}$, turbulent Schmidt number $Sc_t = 0.5$ was chosen (Gromke and Blocken, 2015; A. P. Jeanjean et al., 2017). S_C is the source term. This source is modelled as a specific injection of C in fvOptions with a value of 1000 (units of mass per unit of volume).

Equation for scalar flux

The convection-diffusion equation (Socolofsky and Jirka, 2002) is used to determine the flux of particles. This is based on Equation 2.20 for C that is used in OpenFOAM. A version with simplified notations is shown as follows:

$$\frac{\partial C}{\partial t} + \nabla \left(U_{wind} C \right) - \nabla \left(\alpha_t \nabla C \right) = S \left(C \right) \tag{2.22}$$

This α_t term is dominated by the turbulent viscosity, as $\nu_t \gg \nu$ in general. Mass flux J is defined in the following equation:

$$\frac{\partial C}{\partial t} + \nabla J = S \left(C \right) \tag{2.23}$$

For the steady-state solution $\frac{\partial C}{\partial t} = 0$, we find:

$$\nabla J = S\,(C) \tag{2.24}$$

Now we can split J into two terms: J_{adv}, due to advection, and J_{diff}, due to diffusion. Rewriting for J instead of ∇J gives the following equation:

$$J = J_{adv} + J_{diff} = U_{wind} C - \alpha_t \nabla C \tag{2.25}$$

We can also calculate particle velocity. Since the flux at a certain point in space is the product of particle concentration and the effective particle velocity, we can write:

$$J = C \cdot U_{C,eff} \tag{2.26}$$

Hence, we find for the effective velocity $U_{C,eff}$ of a particle:

$$U_{C,eff} = U_{wind} - \frac{\alpha_t}{C} \nabla C \tag{2.27}$$

This effective velocity is used to describe trends in pollutant transport, like effective velocity profiles. It is also useful to determine the impact of diffusive flux when compared with only advective fluxes.

2.3. Idealised canyon

The influence of the trees is first investigated using a single idealised canyon. This street canyon consists of two rows of buildings of 18 m height. The street is also 18 m wide, resulting in an aspect ratio of 1, which is the average for a city like Rotterdam (Theeuwes et al., 2014). The street canyon is modelled at three different lengths to approach one of infinite length:

- *Single*: 180 m
- *Double*: 360 m
- *Triple*: 540 m

The base length is 180 m as shown in Figure 2.1. All visualisations will be of this *single* case, because this allows for the most up-close look. The *double* and *triple*-length cases are essentially two or three of this *single*-length street placed after each other.

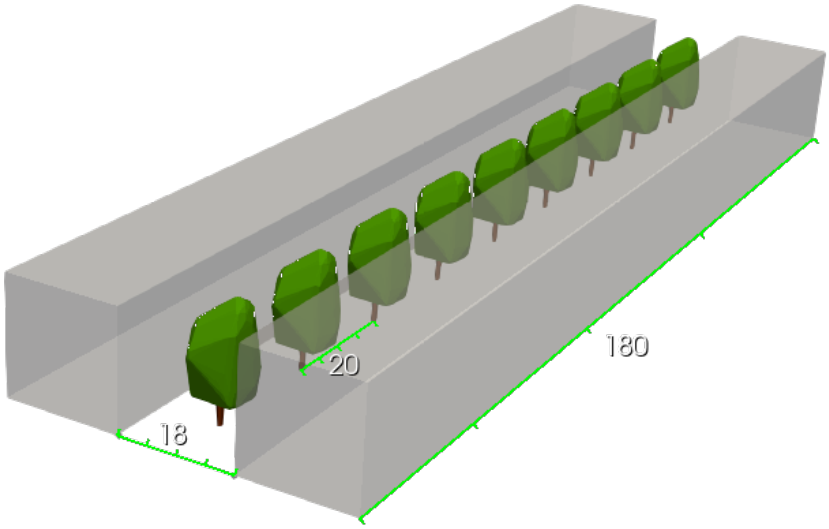

Figure 2.1: Street canyon geometries (single-length)

The open ends of the canyon have a significant influence on the behaviour in the canyon. By increasing the length, a section is created that is far enough away for other phenomena to take place. That section could be deemed representative of an infinite-length canyon and is different per street length and wind direction. The influence of the boundaries is investigated in section 4.1.

Through the middle of the street runs a line of trees at 20 m intervals. This gives nine trees in the single-length case, and 17 and 27 trees in the double-length and triple-length cases, respectively. The trees are 18 m high with an 8 m wide canopy 4 m above the ground, see Figure 2.2. As a result, 7% of the total volume within the canyon is occupied by leaves. The same geometries were used for coniferous and deciduous trees.

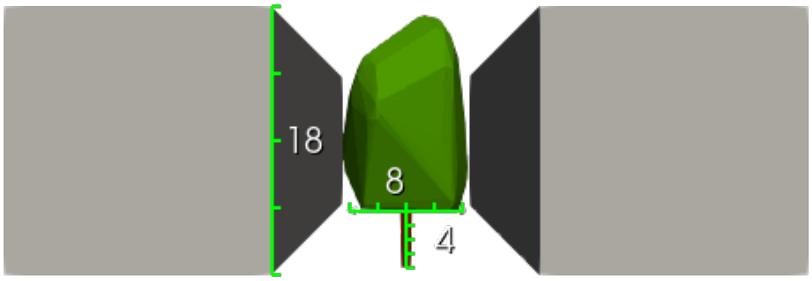

Figure 2.2: Tree geometries

There are two pollutant sources modelled as volume sources along the length of a canyon, representing road emissions. Its centres are 1 m from the ground, 3 m from the trunks and 6 m from the facades of the sides of the buildings, see Figure 2.3. The injections of C in these volume sources are treated separately in the model. This enables a distinct investigation of the dispersion of pollutants $C_{e(ast)}$ and $C_{w(est)}$. For most investigations in this study, only C_e is considered.

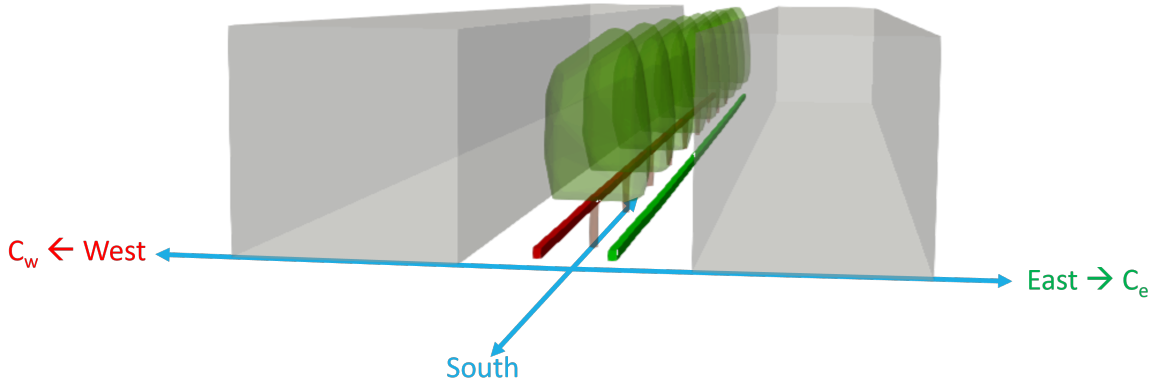

Figure 2.3: Rectangular cuboid volume sources, with in green the eastern road and in red the western road

2.3.1. Mesh

The mesh was created using the blockMesh and snappyHexMesh dictionaries in OpenFOAM. The blockMesh was created using the cylindrical blockMeshDict.m4 by Madadi-Kandjani (2016), modified to satisfy wake development constraints from Blocken (2015). It is based on a square with side lengths defined as $2s$ around the domain, where s is a user-defined input. It is ensured that the square fully encompasses the street canyon, plus extra space on all sides. Based on the height H_{max} of the tallest building (18 m in this case), it automatically generates a cylinder around the square of radius $15H_{max}+2s$, and height $6H_{max}$, as the outflow boundary should be at least $15H_{max}$ away from the buildings, and the clearance to the top needs to be at least $5H_{max}$ from the highest building (Blocken, 2015). Using snappyHexMesh, the grid was refined to obtain a finer mesh around the buildings, the trees and the terrain. A visualisation of the grid is shown in Figure 2.4.

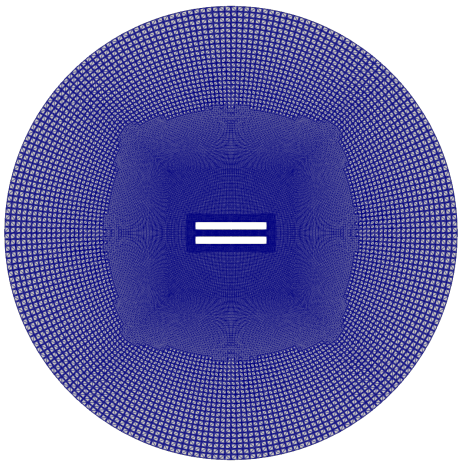

Figure 2.4: Mesh at 10 m height

2.4. Simulations

To answer sub-question 1, simulations are run in the idealised canyon for different wind directions and different LAD values. The wind directions vary from parallel to the street direction, perpendicular to the street, and at a 45° angle. The LAD values vary from 0.2 to 2.2 (Lalic and Mihailovic, 2004), with values of 0.2, 1.0 and 2.2 m^2/m^3. The case with no trees is modelled as an LAD of 0. The tree stems are kept in this case, so the same mesh can be used for all cases. An overview of all simulations can be found in Appendix A.

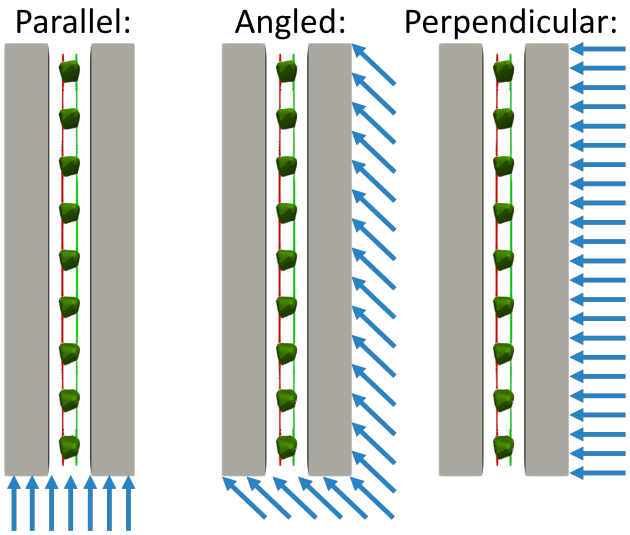

Figure 2.5: Wind directions parallel, angled and perpendicular to the street

2.5. Post-processing

2.5.1. Convergence

First, the validity of the results is checked for convergence. This is done with the *residuals* and *probes* methods. The residuals r show the error between the left-hand side of the equation and the right-hand side $\vec{r} = \vec{b} - A\vec{x}$ (OpenCFD, 2023), while the probes show the actual value at user-defined points. For these probes, locations at both facades, in the middle of the canyon and halfway up the buildings were chosen. The output files show a list of values for each iteration. If the residuals tend to 0, and the gradient of the probe values tends to 0, convergence is achieved. The plots for residuals and probes are shown in Appendix B.

2.5.2. Mesh

To compare the results of different simulations, the OpenFOAM results are exported as a *.vtk*-file. These files contain all the data of the mesh and the values of all variables in each cell. They are all resampled onto a grid with 9 m × 9 m × 9 m cells outside of the canyon and 1 m × 1 m × 1 m cells for the region inside the canyon + 18 m in each direction, converting the data from cell data to point data. This is done to ensure the mesh is neatly aligned with the x-, y-, and z-axes. It also greatly reduces the number of cells, speeding up further calculations. A sketch is shown in Figure 2.6. Appendix D gives more information about how all axes are defined.

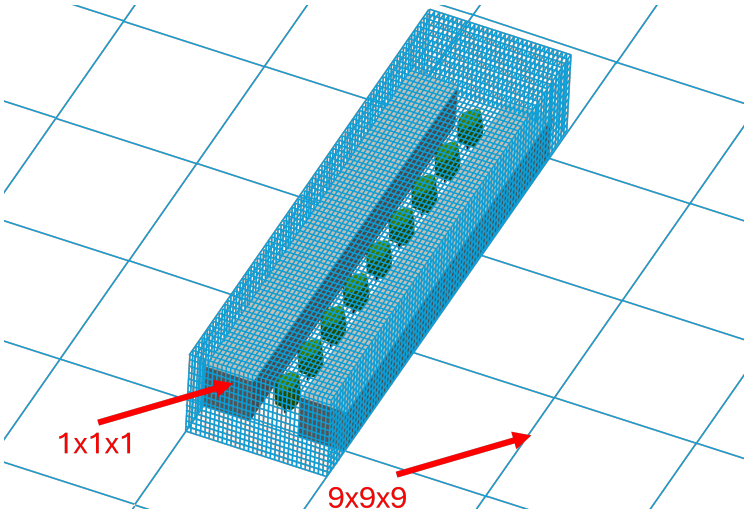

Figure 2.6: Resampling mesh (not to scale)

2.5.3. Plots

Finally, the influence of LAD is quantified and plotted. Since the injection of C is done using an arbitrary number, the raw values of C do not give any useful information. Therefore, the results are normalised by the $LAD = 0$ case for each respective wind direction.

2.6. Seasonality

To answer subquestion 2, the results from the simulations are subjected to meteorological data from KNMI (2025). These datasets contain daily measurements from 50 weather stations around the Netherlands. The oldest ones have measured wind since the early 1900s, but most stations started in either the 1950s or the 1980s/1990s. For the purpose of this research, wind direction ϕ_{KNMI} and speed are the most important parameters. An example table of the data looks as follows:

Table 2.1: Data as extracted from KNMI (2025) (station 344 in Rotterdam)

Date	ϕ_{KNMI} (°)	**Wind speed** (m/s)	ϕ_{region}	$C_{LAD=0}$	$C_{LAD=0.2}$	$C_{LAD=1.0}$	$C_{LAD=2.2}$
1958-06-14	52	1.5					
1958-06-15	133	1.0					
1958-06-16	83	1.5					
...	...	...					
2025-11-20	235	2.3					
2025-11-21	103	1.9					
2025-11-22	184	5.7					

2.6.1. Data processing

The wind directions are given in degrees with respect to north. 0° and 360° correspond to north, 90° to east, 180° to south and 270° to west. Since the street canyon is also directed north by default (see Figure 2.7), the daily wind directions can be related to the wind directions relative to the canyon, as defined in section 2.4. For this, the 360° data at a 1° resolution is classified into eight regions of 45° resolution, which can also be seen in Figure 2.7. The angle regions corresponding to each date are shown in Table 2.2.

Table 2.2: The angle region is added to the table

Date	ϕ_{KNMI} (°)	**Wind speed** (m/s)	ϕ_{region}	$C_{LAD=0}$	$C_{LAD=0.2}$	$C_{LAD=1.0}$	$C_{LAD=2.2}$
1958-06-14	52	1.5	45				
1958-06-15	133	1.0	135				
1958-06-16	83	1.5	90				
...	...	...	...				
2025-11-20	235	2.3	225				
2025-11-21	103	1.9	90				
2025-11-22	184	5.7	180				

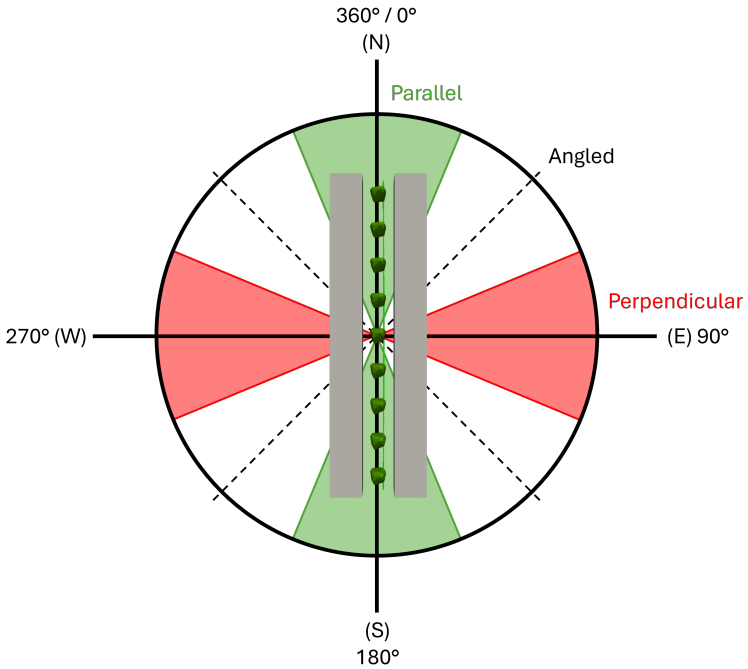

Figure 2.7: All angles in red correspond to perpendicular wind, in green to parallel wind and in white to angled wind.

The OpenFOAM simulations only use three angles: 180° for parallel wind, 135° for angled wind and 90° for perpendicular wind. Due to the symmetries in the street canyon, the simulations from three directions are sufficient to use for the eight defined regions. For this, it is assumed that the trees are also symmetrical, which is not exactly true, but the asymmetries are negligible.

There is, however, one more important asymmetry to consider. Since the sources are not located in the middle of the street canyon, perpendicular winds at angles 90° and 270° should give different (asymmetrical) distributions of both C_e and C_w across the canyon. For this reason, results for C_e and C_w are interchanged based on the wind direction. This is under the assumption that the behaviour of C_e under 270° wind (which is unknown) is the same as the behaviour of C_w under 90° wind (which is known), but mirrored, like in Figure 2.8. This is also considered for the other angles. An overview can be seen in Table 2.3.

Of course, the street direction does not need to be aligned north-south. Street canyons of different orientations are accounted for by rotating the frame of reference from the KNMI stations. A clockwise rotation of the street, say $\phi_{street} = 45°$, is modelled by a counter-clockwise rotation of the measured wind direction ϕ_{KNMI} by 45°. The resulting value of $\phi_{relative}$ is then used to assign the angle region.

$$\phi_{relative} = \phi_{KNMI} - \phi_{street} \tag{2.28}$$

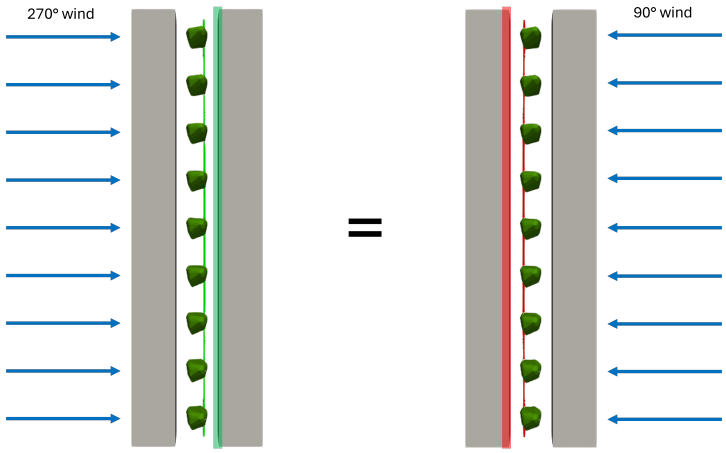

Figure 2.8: The effects of 270° wind on the concentration of C_e (green) on the eastern facade is unknown. However, the concentration of C_w (red) on the western facade is known for 90° wind. It is assumed that due to symmetries, these are the same and can be interchanged.

Table 2.3: Depending on the wind direction, the scalar that is treated as C_e is different

Angle region (°)	Angle OpenFOAM	Scalar used for C_e
0 / 360	Parallel	C_w
45	Angled	C_e
90	Perpendicular	C_e
135	Angled	C_e
180	Parallel	C_e
225	Angled	C_w
270	Perpendicular	C_w
315	Angled	C_w

2.6.2. Scalar input and seasonality

The determined angles and scalars are coupled for each LAD with their corresponding value for two metrics C. One is the mean C_e at the eastern facade at a height of 2 m. The second metric is the mean C_e for the volume below 2 m. The value of the simulated C metric is then scaled with wind speed according to Equation 2.31. This equation assumes the values of C are proportional to U^{-1} for high Reynolds numbers (Martín et al., 2024; Schatzmann and Leitl, 2011). Schatzmann and Leitl (2011) give a formula to compute the normalised value of C at any location:

$$C^* = \frac{CUH}{Q/L} \tag{2.29}$$

Here, H is the characteristic building height, and Q/L is the source strength. When scaling the value of C with wind speed, these parameters do not change. This results in the following equation, relating C for the simulated case with a new case of different wind speed via this value of C^*:

$$\frac{CU_{actual}H}{Q/L} = C^* = \frac{C_{simulated}U_{ref}H}{Q/L} \tag{2.30}$$

U_{ref} = 4.97 m/s at 10 m and the value of U_{actual} is the one from the dataset, which was also taken at 10 m. Rewriting yields:

$$C = C_{simulated}\frac{U_{ref}}{U_{actual}} \tag{2.31}$$

The example lines in the table can be seen in Table 2.4. Note that these values by themselves are meaningless. Only by comparing them to each other can meaningful conclusions be drawn.

Table 2.4: The mean values of C_e below 2 m corresponding to the angle region, wind speed and LADs are added to the table

Date	ϕ_{KNMI} (°)	**Wind speed** (m/s)	ϕ_{region}	$C_{LAD=0}$	$C_{LAD=0.2}$	$C_{LAD=1.0}$	$C_{LAD=2.2}$
1958-06-14	52	1.5	45	792.5	871.0	861.1	826.0
1958-06-15	133	1.0	135	1188.8	1306.6	1291.7	1238.9
1958-06-16	83	1.5	90	663.2	660.4	655.1	652.1
...	...	...	...	...	...	...	...
2025-11-20	235	2.3	225	500.4	589.6*	591.4*	585.3*
2025-11-21	103	1.9	90	523.6	521.3*	517.2*	514.8*
2025-11-22	184	5.7	180	267.8	266.7*	470.5*	500.9*

Finally, the data is adjusted to seasonal changes for deciduous trees. In the months of November to March, the trees are assumed to be leafless. In these time periods, all values in the last three columns (marked with a *) are set to the value of the $C_{LAD=0}$ column. These are used to compare monthly differences between deciduous and coniferous cases:

Table 2.5: The seasonal effect of deciduous trees is incorporated by setting $C_{LAD>0}$ values to those of $C_{LAD=0}$ in November to March

Date	ϕ_{KNMI} (°)	**Wind speed** (m/s)	ϕ_{region}	$C_{LAD=0}$	$C_{LAD=0.2}$	$C_{LAD=1.0}$	$C_{LAD=2.2}$
1958-06-14	52	1.5	45	792.5	871.0	861.1	826.0
1958-06-15	133	1.0	135	1188.8	1306.6	1291.7	1238.9
1958-06-16	83	1.5	90	663.2	660.4	655.1	652.1
...	...	...	...	...	...	...	...
2025-11-20	235	2.3	225	500.4	500.4	500.4	500.4
2025-11-21	103	1.9	90	523.6	523.6	523.6	523.6
2025-11-22	184	5.7	180	267.8	267.8	267.8	267.8

For the final results of this section, three cases are compared. A case without trees, a case with coniferous trees, and a case with deciduous trees. Since deciduous trees generally have a greater LAD than coniferous trees (Lalic and Mihailovic, 2004), this is included in the plots of the results. Three scenarios are compared: coniferous trees with $LAD = 0.2$ versus deciduous trees with $LAD = 1.0$, coniferous trees with $LAD = 0.2$ versus deciduous trees with $LAD = 2.2$, and coniferous trees with $LAD = 1.0$ versus deciduous trees with $LAD = 2.2$.

3
Method verification

In this chapter, some assumptions are verified. Firstly, the resampling mesh is checked for influence. Then, it is researched which values of LAD are actually needed for further simulations in order to draw conclusions. Lastly, it is checked how fluxes can be calculated most accurately on the boundaries of the street canyon.

3.1. Resampling mesh

As stated in section 2.4, the *.vtk* files are resampled onto a Cartesian grid. To ensure that the resampling mesh does not significantly influence the results, the resolution of this grid was tested for the mean C. This was done with a resolution parameter for the fine mesh that represents the number of cells per meter in each direction. The results are shown in Table 3.1.

Table 3.1: Tested resolutions in number of cells per meter.

Resolution (#cells/m)	0.2	0.4	0.6	0.8	1.0	1.2	1.4	1.6	1.8	2.0
Mean C in canyon	138	124	123	127	124	126	125	124	125	124

The resolution of the mesh does not significantly affect the results after a resolution of 0.4 cells per meter. Still, a resolution of 1 cell per meter in each direction was chosen to balance between computing time and the detail of the graphs.

3.2. LAD values

Since trees have LAD values varying from 0.2 to 2.2 m^2/m^3 (Lalic and Mihailovic, 2004), it needs to be considered for which LADs to run simulations. For this, some first simulations were run for the 180 m 'single' length case with LAD intervals of 0.4 m^2/m^3. Normalised values of C_e were plotted over a line on the facades at 1.75 m height, as shown in Figure 3.1 for one facade. The left column shows the values for the east facade, close to the source, and the right column shows those for the west facade, on the other side of the street.

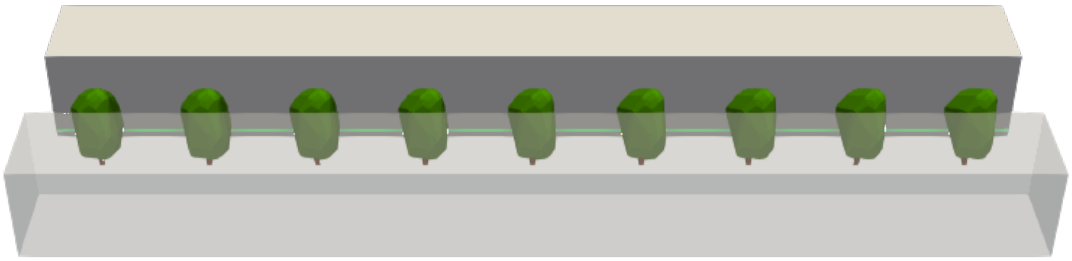

Figure 3.1: Line at 1.75 m at which C_e values are taken

As can be seen in Figure 3.2, different LAD values give relatively predictable behaviour. The greater the value for LAD, the more extreme the responses for C_e. This is for all three wind directions. The lines indicate that the behaviour of $LAD = 0.6$, for example, lies predictably between those of $LAD = 0.2$ and $LAD = 1.0$. The same is true for the other lines. Therefore, a selection of LAD values is made for which further simulations need to be run. The chosen values are 0 m^2/m^3, representing no leaves; 0.2 m^2/m^3, to investigate the effects of a very low LAD; 1.0 m^2/m^3, because it is a very general LAD value and gives fairly average results; and 2.2 m^2/m^3, to investigate the most extreme case. For all other values of LAD, it is assumed that the results will be somewhere in between.

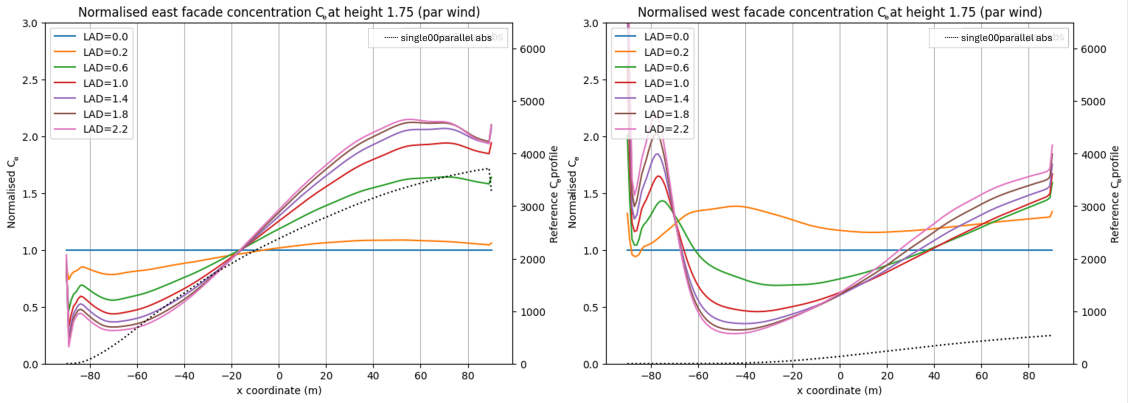

(a) Parallel

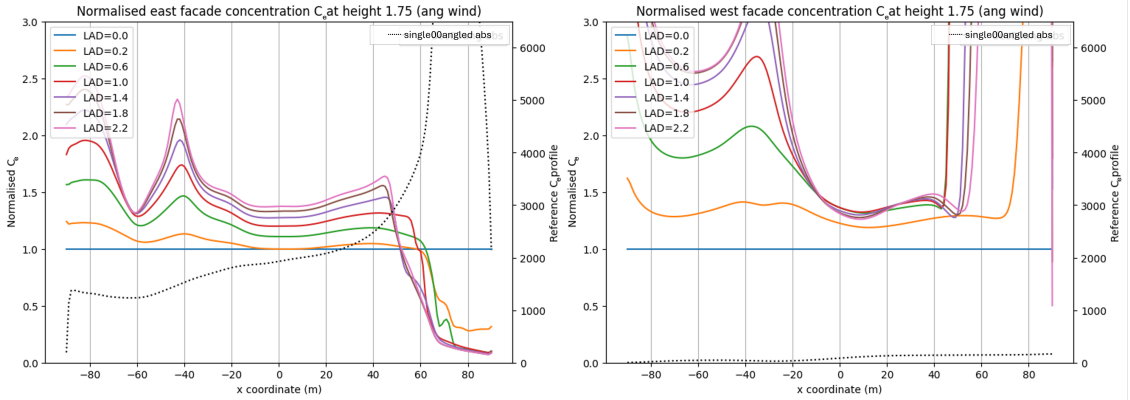

(b) Angled

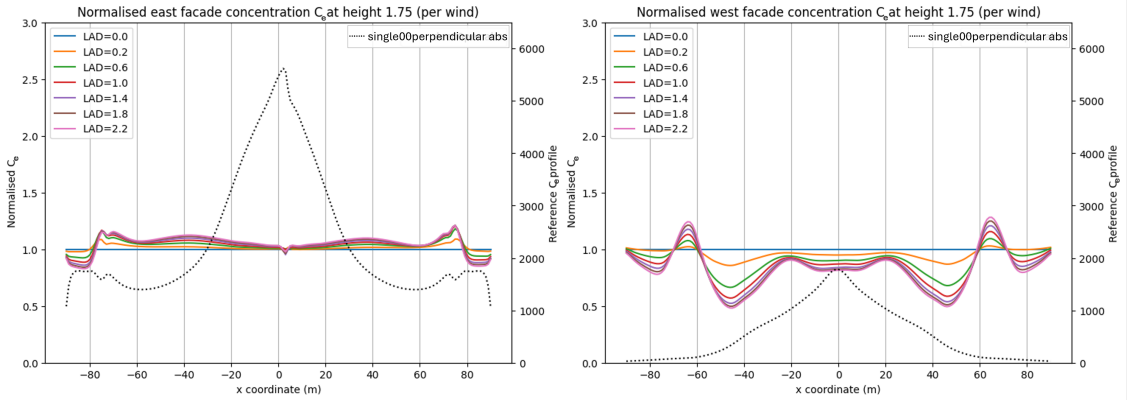

(c) Perpendicular

Figure 3.2: Facade concentrations of C_e at 1.75 m height for each wind direction and both facades. The concentrations are normalised by the values for $LAD = 0$, of which the values are shown in the dotted line and the axis on the right-hand side of the figures. The left column is for the east side, close to the source. The right column is for the west side, on the other side of the trees.

3.3. Pollutant ventilation

As described in Equation 2.25, the transport is the sum of two components for J, an advective mass flux and a diffusive mass flux. Divided by the value of C, it gives the effective particle velocity $U_{C,eff}$ (Equation 2.27), which is used for the calculations, as it allows for easy comparison between the particle movements and air flow U. To see how much the two differ, the transport out of the canyon was researched. The mass fluxes on each boundary (south end, top and north end) were calculated with the value for concentration C_e and either U_{wind} or $U_{C,eff}$. The respective surface areas A of these boundaries are $A_{south} = A_{north} = 324$ m^2 and $A_{top} = 3240$ m^2. The mass fluxes from all other boundaries are also calculated. Except for some numerical inconsistencies, these are practically 0 there, because there is no flow possible through the buildings or the ground. In the following tables, positive values represent mass flux out of the canyon.

Table 3.2: Mass fluxes from all boundaries for parallel wind and $U = U_{wind}$

LAD	NORTH	EAST	SOUTH	WEST	TOP	BOTTOM	TOTAL	ERROR (%)
0.0	85137.0	-2.8	-233.8	-2.3	-1802.1	0.0	83095.9	-15.8
0.2	71841.3	-6.7	-238.9	-6.0	-1911.3	0.0	69678.5	-29.4
1.0	70747.7	-9.5	-251.5	-7.8	-2593.1	0.0	67886.9	-31.2
2.2	69752.4	-10.1	-259.3	-8.2	-2637.8	0.1	66839.2	-32.3

Table 3.3: Mass fluxes from all boundaries for angled wind and $U = U_{wind}$

LAD	NORTH	EAST	SOUTH	WEST	TOP	BOTTOM	TOTAL	ERROR (%)
0.0	37759.4	-105.0	-2958.0	124.3	35802.9	0.0	70623.6	-28.5
0.2	22224.2	-123.8	-3032.9	171.9	38103.6	0.0	57343.2	-41.9
1.0	7106.9	-193.8	-3919.2	421.3	38794.7	0.0	42210.9	-57.2
2.2	6030.5	-221.7	-4211.4	300.6	38301.5	0.0	40201.7	-59.3

Table 3.4: Mass fluxes from all boundaries for perpendicular wind and $U = U_{wind}$

LAD	NORTH	EAST	SOUTH	WEST	TOP	BOTTOM	TOTAL	ERROR (%)
0.0	-1118.2	-71.1	-1118.8	48.1	30984.3	0.0	28724.1	-70.9
0.2	-1036.2	-78.4	-1037.5	50.3	31681.9	0.0	29580.4	-70.0
1.0	-831.9	-91.5	-834.4	58.7	33602.2	0.0	31904.1	-67.7
2.2	-703.8	-89.9	-705.8	65.8	34588.3	0.0	33156.7	-66.4

The errors are calculated with the theoretical value of 98705.7 (mass/volume/time). This is the value that is injected into the canyon in the OpenFOAM model for the single-length case. For the equilibrium, everything that is put into the system must also come out. It is clear that calculating the fluxes solely based on wind speed is not the most accurate method, as turbulent diffusion plays a significant role. That is also evident from the calculations with $U_{C,eff}$:

Table 3.5: Mass fluxes from all boundaries for parallel wind and $U = U_{C,eff}$

LAD	NORTH	EAST	SOUTH	WEST	TOP	BOTTOM	TOTAL	ERROR (%)
0.0	85272.2	-0.5	-162.4	-0.4	8430.9	0.0	93539.7	-5.2
0.2	72046.1	0.7	-163.6	0.5	22039.4	0.0	93923.2	-4.8
1.0	70734.9	-0.8	-166.4	-0.7	22868.3	0.0	93436.2	-5.3
2.2	69364.2	-0.2	-167.9	-0.3	24900.0	0.0	94098.1	-4.7

Table 3.6: Mass fluxes from all boundaries for angled wind and $U = U_{C,eff}$

LAD	NORTH	EAST	SOUTH	WEST	TOP	BOTTOM	TOTAL	ERROR (%)
0.0	38523.7	-92.9	-1720.6	144.6	52347.6	0.0	89202.3	-9.6
0.2	25383.9	-105.4	-1754.9	203.0	65016.5	0.0	88743.3	-10.1
1.0	11174.6	-168.4	-2253.4	499.3	76468.7	0.0	85721.9	-13.2
2.2	8932.5	-190.7	-2435.7	358.1	78949.8	0.0	85616.2	-13.3

Table 3.7: Mass fluxes from all boundaries for perpendicular wind and $U = U_{C,eff}$

LAD	NORTH	EAST	SOUTH	WEST	TOP	BOTTOM	TOTAL	ERROR (%)
0.0	142.3	-58.9	141.8	58.9	86233.1	0.0	86517.3	-12.3
0.2	184.8	-65.7	178.6	61.2	85851.1	0.0	86210.2	-12.7
1.0	222.0	-76.9	216.3	70.8	85163.3	0.0	85596.4	-13.3
2.2	229.8	-74.5	229.7	79.3	84887.9	0.0	85354.4	-13.5

Now, the errors are much smaller, which suggests that the diffusive fluxes are indeed very significant. Especially for perpendicular wind, the errors were reduced from 70% to 13%. Still, however, this error is not equal to 0. In this instance, the issue is numerical complications resulting from resampling the OpenFOAM mesh onto the Python mesh. The calculations are heavily influenced by the points representing the sides of the buildings. To reduce this, the borders of the bounding box were extended, as depicted in Figure 3.3. Extending the bounding box of the canyon by one cell, or 1 m in this case, reduces the error to around 2-3% in most cases.

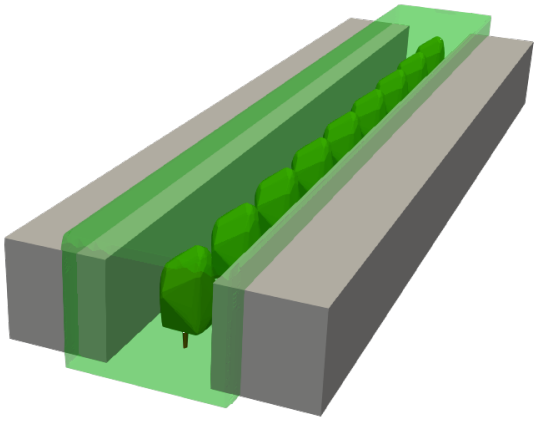

Figure 3.3: The bounding box is extended by one cell (1 m) to reduce numerical complications on the sides of the buildings (not to scale)

Table 3.8: Mass fluxes from all boundaries for parallel wind and $U = U_{C,eff}$ with extended bounding box

LAD	NORTH	EAST	SOUTH	WEST	TOP	BOTTOM	TOTAL	ERROR (%)
0.0	91995.4	-788.5	-6.3	-299.4	7563.3	0.0	98464.5	-0.2
0.2	79682.5	-644.0	-6.9	-294.9	20589.5	0.0	99326.4	0.6
1.0	81184.3	-1379.2	-8.4	-486.6	21734.6	0.0	101045.7	2.4
2.2	81166.4	-1562.9	-9.4	-532.0	23828.5	0.0	102892.8	4.2

Table 3.9: Mass fluxes from all boundaries for angled wind and $U = U_{C,eff}$ with extended bounding box

LAD	NORTH	EAST	SOUTH	WEST	TOP	BOTTOM	TOTAL	ERROR (%)
0.0	43908.7	772.9	87.3	4715.5	50995.5	0.0	100479.8	1.8
0.2	28900.2	996.5	108.2	6248.1	64063.2	0.0	100316.4	1.6
1.0	14714.6	552.9	197.5	8696.6	77021.0	0.0	101183.6	2.5
2.2	11705.1	496.4	259.4	8514.9	80587.7	0.0	101565.6	2.9

Table 3.10: Mass fluxes from all boundaries for perpendicular wind and $U = U_{C,eff}$ with extended bounding box

LAD	NORTH	EAST	SOUTH	WEST	TOP	BOTTOM	TOTAL	ERROR (%)
0.0	511.7	1158.8	511.3	9483.2	88558.7	0.0	100223.8	1.5
0.2	529.6	1192.6	523.4	9379.6	88866.9	0.0	100492.3	1.8
1.0	508.1	1257.5	505.3	9116.1	89431.9	0.0	100819.9	2.1
2.2	481.6	1295.2	487.6	8976.6	89633.5	0.0	100876.7	2.2

4
Results

This chapter describes the results obtained from the simulations. Different occurring phenomena are explained and quantified. These depend on the length of the simulated canyon. Then, the effect of LAD is reported for the pollutant concentrations and the mass transport. Lastly, the yearly results for different tree types are researched.

4.1. Influence of canyon length

Before analysing quantitative results, some qualitative differences are reported concerning the occurring phenomena in the results that are dependent on the length of the canyon in the model.

4.1.1. Boundary effects for perpendicular wind

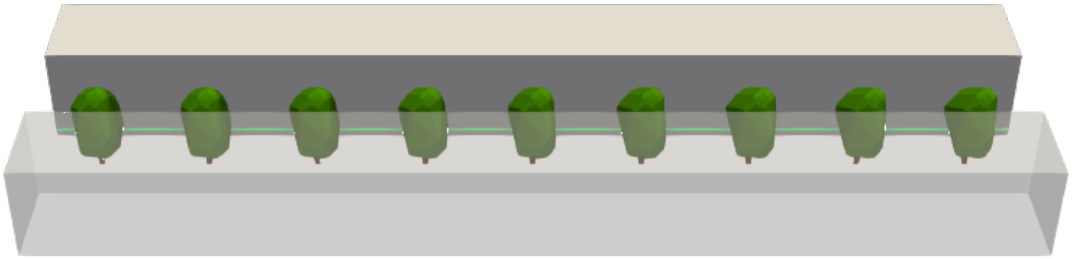

Figure 4.1: Line at 1.75 m at which C_e values are taken. The values are taken for both facades, and the source is on the eastern side.

The first phenomenon concerns the effects of the open street ends. This is already prevalent for the normal length case of 180 m and most noticeable for perpendicular wind. When plotting the facade values of C_e on both concentrations, again for a height of 1.75 m, different regions form, which can be seen in Figure 4.2.

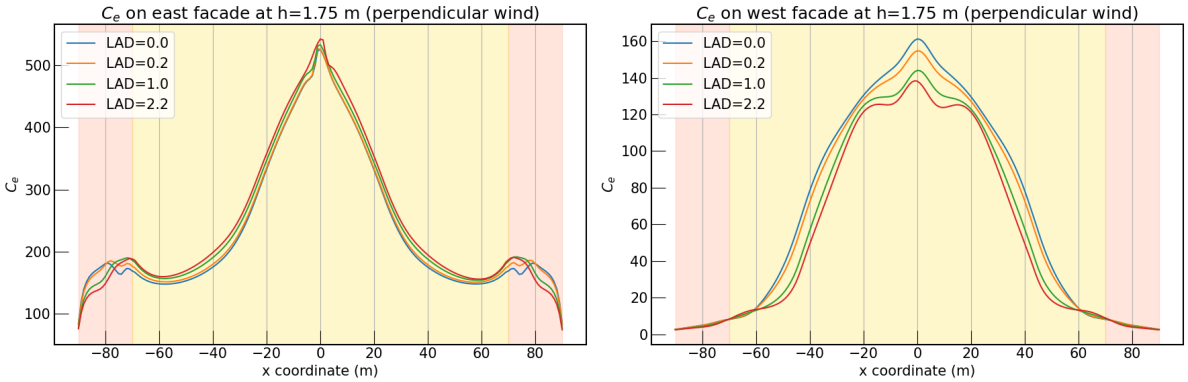

Figure 4.2: Different regions form with different behaviour for the dispersion of C_e

Near the ends of the canyon, regions of 40 m are well-mixed, resulting in a relatively constant pollutant concentration. These are marked red in the figure. In the yellow region between these ends, the influence of fresh air entering from the side is diminishing, and therefore, C_e tends to another equilibrium. This equilibrium state, if reached, is representative of an infinite length canyon, as making the street longer would not alter the behaviour of C_e in this section. For the 180 m street, this equilibrium is not yet reached.

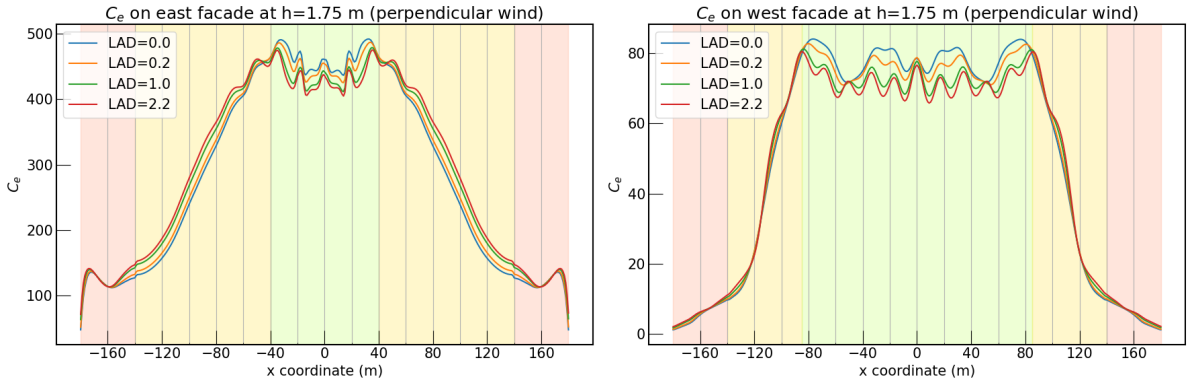

Figure 4.3: In the double-length case, a new region forms in the middle of the canyon

With the double-length case, shown in Figure 4.3, the effects of individual trees start to appear as shown in the green region. There are clear spikes in concentrations at the locations of trees (at the vertical grid lines). In this region, the influence of LAD has also flipped. In the outer regions, higher LAD results in higher C_e values on the facades at 1.75 m. However, within the tree influence zone, increasing LAD leads to a decrease in facade C_e.

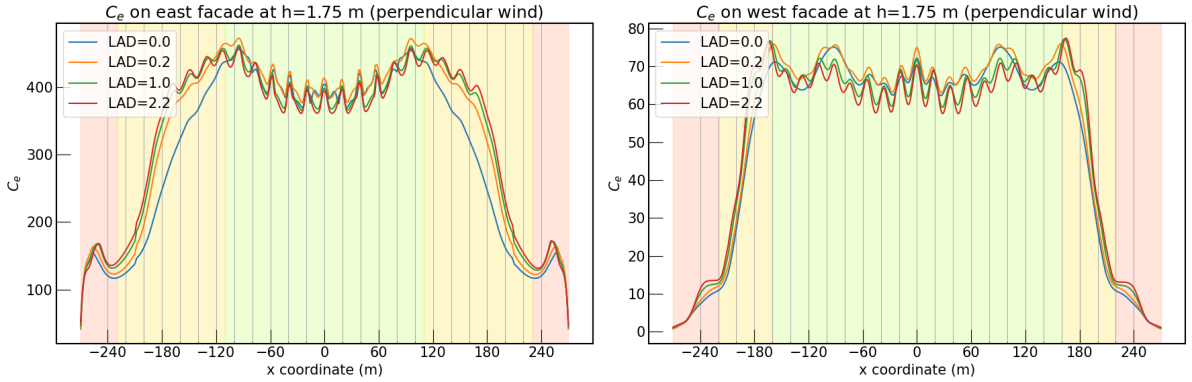

Figure 4.4: In the triple-length case, the green region has expanded

These described phenomena are also present in Figure 4.4 for the triple-length case. The green zone with significant tree impact has now grown, but has the same properties. For this length, there are no new regions compared to the double-length case.

4.1.2. Boundary effects for parallel wind

Another phenomenon occurs with parallel wind. This is not yet clearly present in the single-length case.

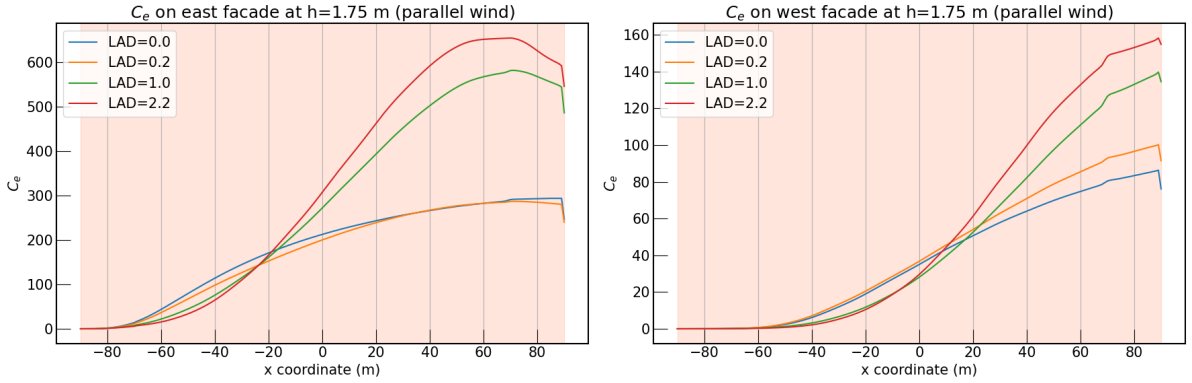

Figure 4.5: For parallel wind, there is only one region in the single-length case

As shown in Figure 4.5, the concentrations of C_e on the facades grow as the wind blows through the canyon. This is to be expected, as the C_e is injected uniformly along the street and accumulates in the direction of the air flow. Near the end of the street, there is a dip in C_e, which can be explained by an acceleration in the flow. Since there are no obstructions in the model after the street canyon geometry, a low-pressure zone forms due to higher wind speeds, which sucks in air from its surroundings, diluting the polluted air. The entire canyon can be considered a single zone, marked red.

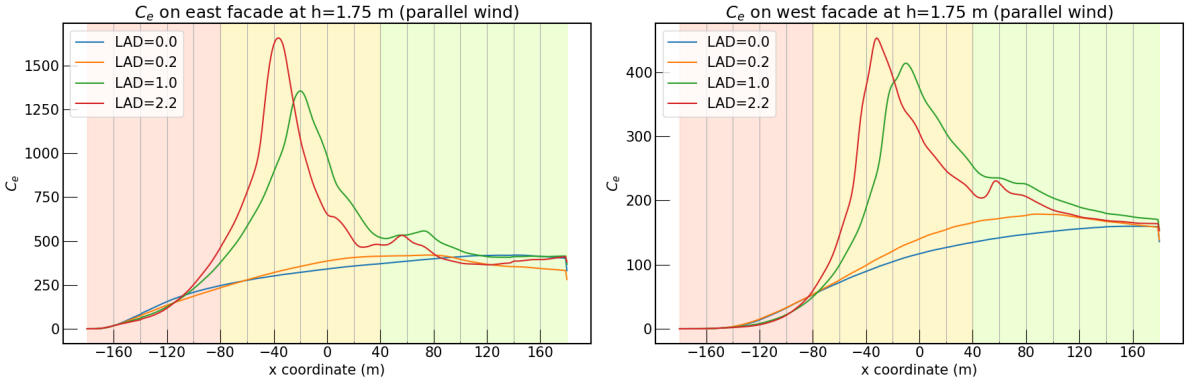

Figure 4.6: With the double-length street, there is a sudden spike in C_e on the facade

For the double-length case in Figure 4.6, an interesting thing happens in the yellow zone between 100 m and 200 m from the street's entrance. Here, for sufficiently high LAD values, a recirculation zone forms, as shown by the streamlines in Figure 4.7.

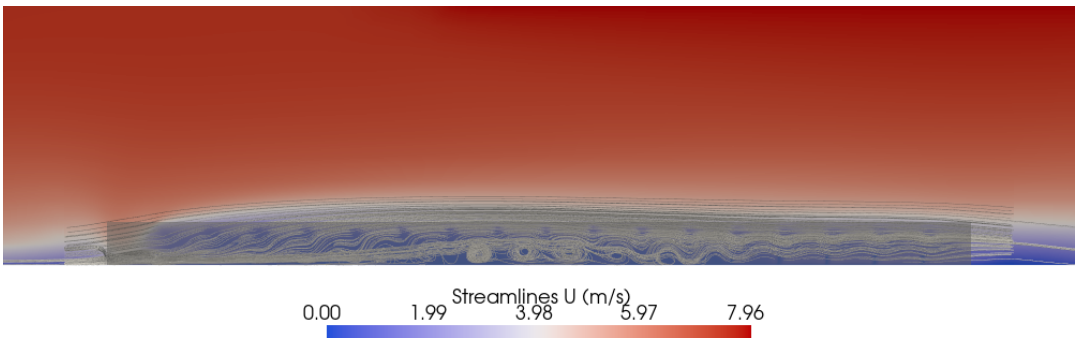

(a) Streamlines

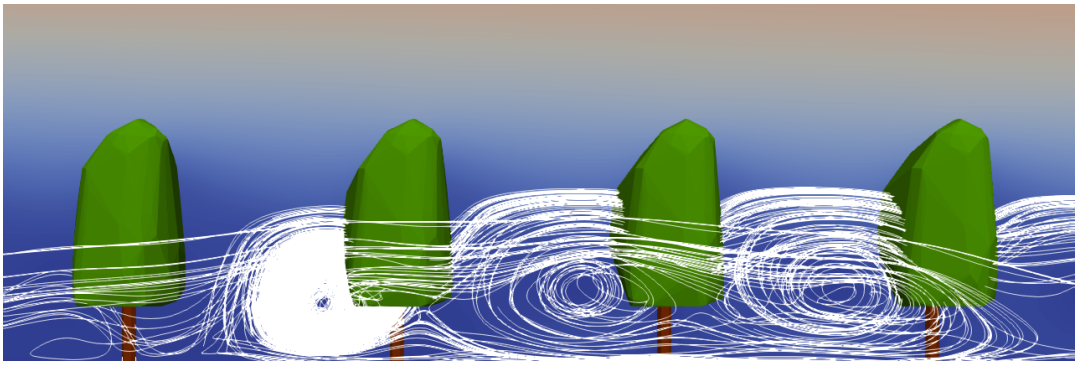

(b) The recirculations occur mainly between trees

Figure 4.7: Recirculation zones in the streamlines of the double-length case with $LAD = 2.2$ and parallel wind.

These recirculations cause the C_e to accumulate in these regions, which explains the spikes in Figure 4.6. They are created by the wind that is forced up by trees upon entering the canyon, see Figure 4.8. This effect is stronger for higher LAD values, which explains why it does not happen for LADs 0 and 0.2, and why the spike occurs

sooner in the $LAD = 2.2$ case. After around 150 m, the air starts to re-enter the canyon, after which the tree canopy accelerates the flow downwards, as seen in the blue values in Figure 4.8. The difference in the air first being forced upwards, and then moving back down, creates a region in which air flow is reversed near the ground. After this zone, the flow stabilises and shows similar behaviour throughout the rest of the street, marked in green. The effect of trees is still visible in the streamlines.

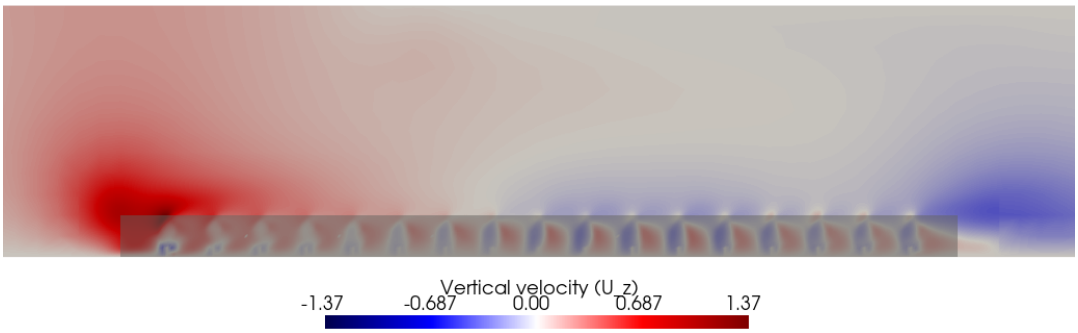

Figure 4.8: Vertical velocity component of wind speed for double-length case and parallel wind ($LAD = 2.2$). The positive direction (red values) is upwards, and the blue values indicate downward winds.

Looking back, this is also almost happening for the single-length case, but it has no time to fully develop due to the acceleration effects at the end of the street. This does explain why the facade values of C_e are significantly higher for LADs 1.0 and 2.2 in Figure 4.5. The acceleration at the end of the street prevents the recirculations from forming, even though the same downward flow is occurring after said distance of about 150 m in Figure 4.9.

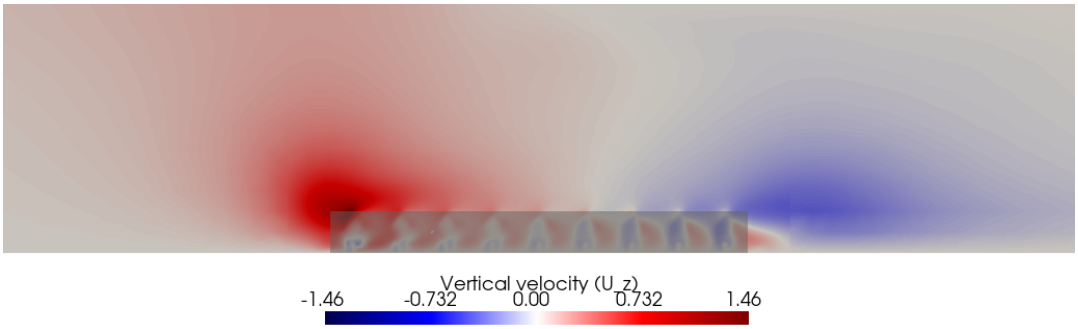

Figure 4.9: Vertical velocity component of wind speed for single-length case and parallel wind ($LAD = 2.2$)

Similarly to the case of perpendicular wind, the parallel case does not introduce new phenomena with the tripled length of the street canyon. The only difference is that the longer street allows the accumulation process to occur again in the green region after the big recirculation spike, as shown in Figure 4.10.

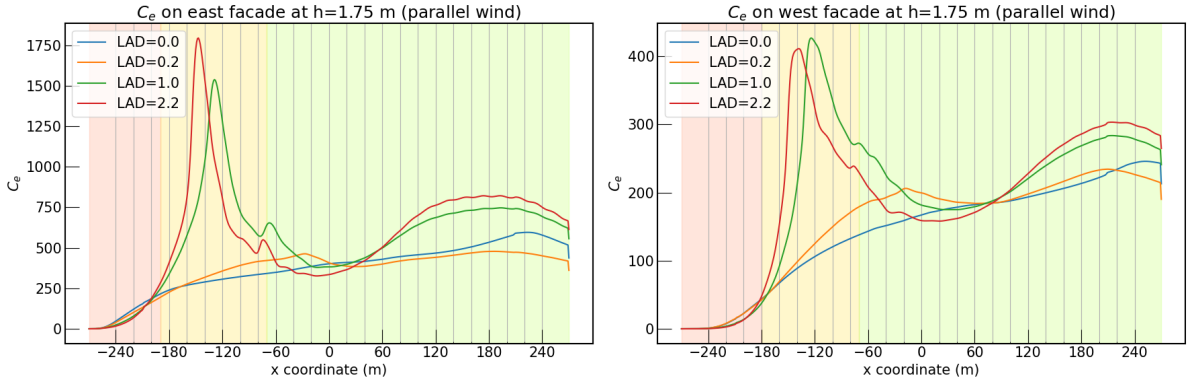

Figure 4.10: The last region of C_e behaves similarly to the single-length case where the pollutants accumulate in the direction of the wind

4.1.3. Boundary effects for angled wind

The angled wind cases for the three lengths show behaviour from both scenarios, with an entering zone in red, accumulation in the direction of the wind into a spike due to recirculation in yellow, and the effects of individual trees visible in green, as shown in Figure 4.11 to Figure 4.13. There is one more new phenomenon, which is recirculation near the end of the canyon for the single-length case. This is very specific for just this case and for specific LADs, so no general conclusions can be drawn from this.

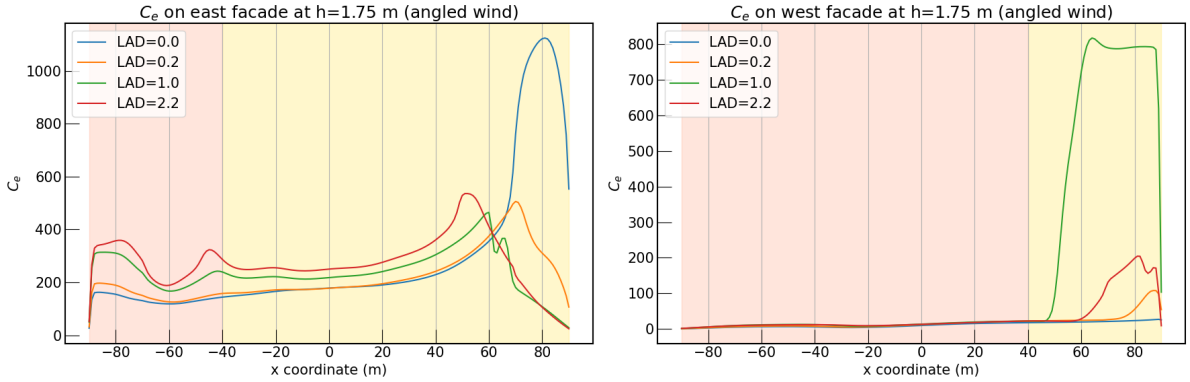

Figure 4.11: For angled wind and specific LAD values, a recirculation spike occurs at the exit of the street.

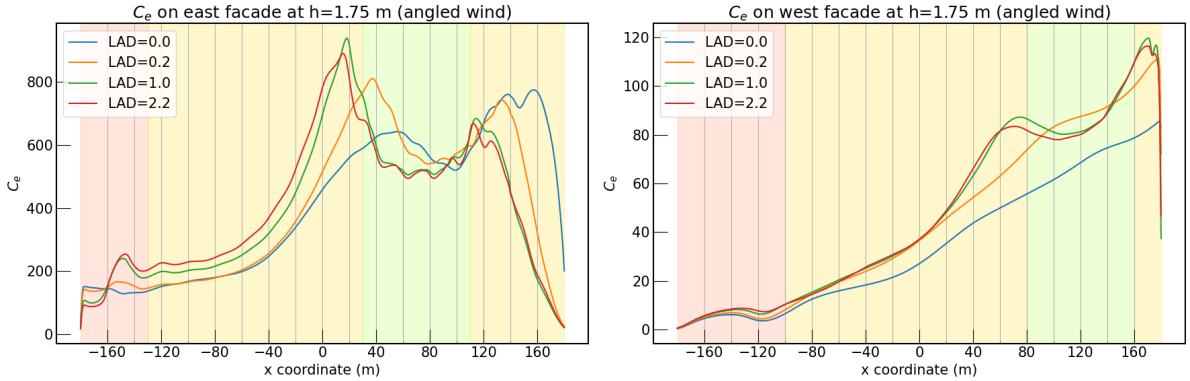

Figure 4.12: With the double-length street, the peak at the end has disappeared, and it shows the characteristics of parallel wind and perpendicular wind

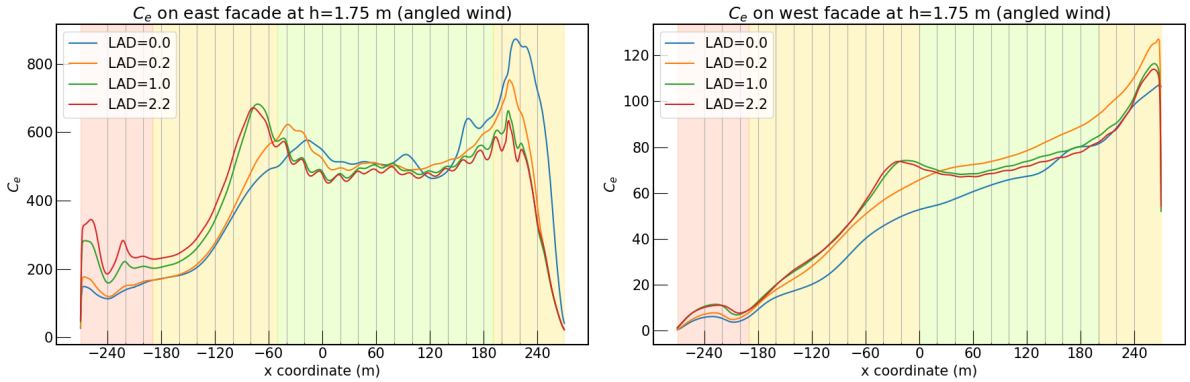

Figure 4.13: With the triple-length street, there are no new behaviours

Since all phenomena are prevalent in the double-length case, and additional post-processing calculations are significantly quicker than those of triple-length, the rest of this chapter will discuss only the results from this length.

4.2. Mean C

In Figure 4.14b, the mean C_e value at 1.75 m height is plotted per LAD value and for all wind directions. This 'nose height' is the height representative of the height of the air we breathe. The mean was first calculated for the full length and width of the canyon, as shown in Figure 4.14a. All values are normalised with that of $LAD = 0$ and perpendicular wind. The reference value of this case is shown in yellow.

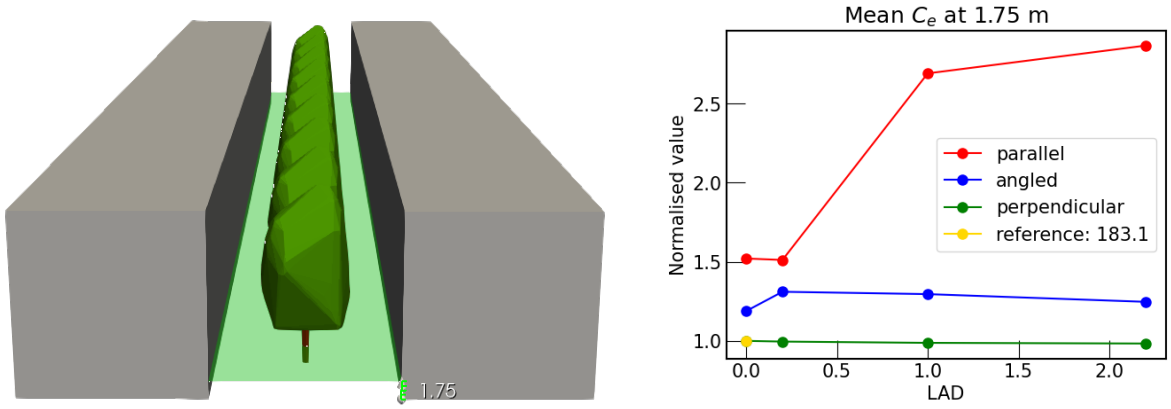

(a) Horizontal slice at 1.75 m at which the mean was taken

(b) Normalised values of mean C_e

Figure 4.14: Normalised values of mean C_e at *nose height*, for all wind directions and all LADs

In the case of parallel wind, the trees hinder the upward transport of the pollutants. Additionally, as reported in section 4.1, for the higher LAD values, recirculation zones are observed with a sudden increase in C_e. Hence, the jump in the mean slice C_e. Increasing LAD also decreases the ventilation in the canyon. Figure 4.15 shows the wind speed profiles with height along the length of the canyon. Higher LAD values result in lower wind speeds everywhere. Decreasing wind speed means a smaller volume of fresh air enters the canyon, which limits dilution. Interestingly, the mean value for C_e stays relatively constant for $LAD = 0.2$ compared to the 0-case. The regions near the ends of the street, where $LAD = 0.2$ causes a decrease in C_e, cancel out the portion in the middle, where the C_e values are higher for the $LAD = 0.2$ case.

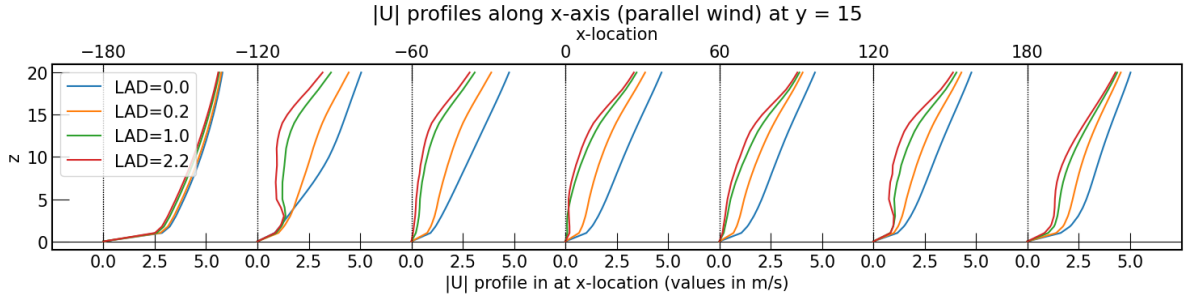

Figure 4.15: Wind speed profiles along the canyon for parallel wind

For perpendicular wind, the line is more or less flat. It even has a slight negative slope, indicating that an increase in LAD would mean a slight decrease in mean C_e at nose height. This is not true for the entire canyon. An increase in LAD means an increase in C_e on the side of the source, where the wind is coming from, and a decrease on the other side of the trees, see Figure 4.16a. For this figure, the C_e values are normalised with the $LAD = 0$ case. Blue values indicate lower concentrations with LAD and red indicate higher concentrations. Only in the middle section of the canyon (the tree influence zone marked in green in Figure 4.3), the value of C_e decreases with LAD over the full width of the street. This can also be seen in Figure 4.16b.

The slight decrease in C_e with LAD can be explained by the increased efficiency of vertical transport around the trees, due to the geometries of the canyon and the trees. As shown in Figure 4.17, these geometries create a vortex spanning the size of the canyon that circles around the trees. This flow allows for more pollutants to exit the canyon.

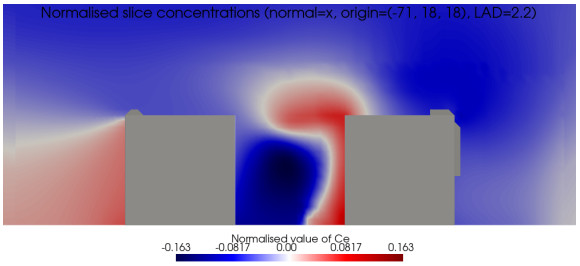

(a) Values of C_e normalised for perpendicular wind and LAD = 2.2 with those of LAD = 0 at 70 m from the centre

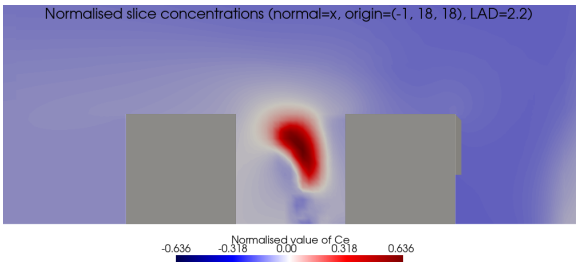

(b) Values of C_e normalised for perpendicular wind and LAD = 2.2 with those of LAD = 0 at the centre

Figure 4.16: Normalised values of C_e at different slices in the street canyon for perpendicular wind (right to left)

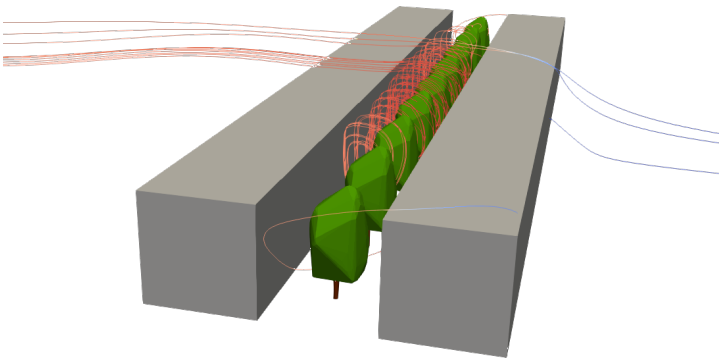

Figure 4.17: The street canyon allows for a rotational flow around the trees. Increasing LAD likely enhances this phenomenon.

Since the boundary effects can be very significant, the same plots are made for the zones in the street that were marked green in Figure 4.3, Figure 4.6 and Figure 4.12. The green zones differ for both facades. However, since the values of the green zone at the eastern facade are significantly higher than those at the western facade, these x-values were used. Thus, x-regions [40, 180], [30, 110] and [-40, 40] were used for parallel, angled and perpendicular wind, respectively. The values are again normalised with those for perpendicular wind and LAD = 0, and they are shown in Figure 4.18.

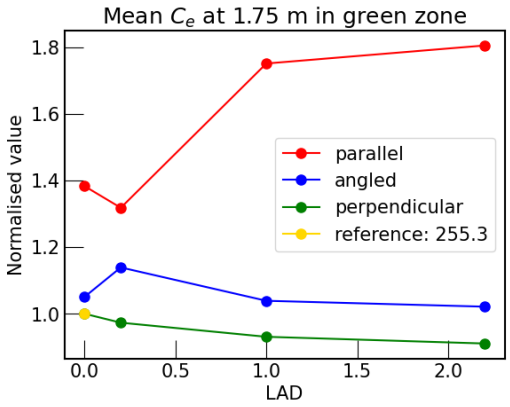

Figure 4.18: Normalised values of mean C_e at *nose height*, for all wind directions and all LADs but only the green zones

There are some interesting differences now. There is still a strong increase for parallel wind and higher LADs. However, a low LAD of 0.2 results in lower air pollution than the LAD = 0 case. All values are still significantly (30%-80%) higher than for the reference. With angled wind, the LAD = 0.2 case behaves differently, resulting in higher air pollution. Contrary to the parallel wind results, C_e decreases with LAD after this low LAD value. The values for angled wind are 2%-13% higher than the reference. For perpendicular wind, C_e decreases with LAD with up to 10%.

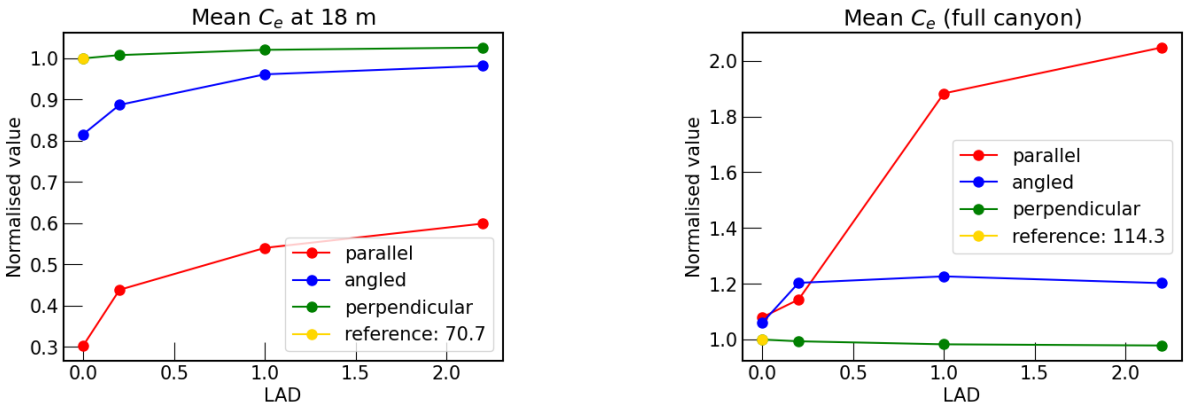

(a) Normalised mean values of C_e at 18 m

(b) Normalised mean values of C_e within the entire canyon

Figure 4.19: Normalised values of C_e at the top of the canyon and within the entire canyon

At 18 m height, the trends are similar, with increasing mean C_e for increasing LAD, see Figure 4.19a. This time, it is also the case for perpendicular wind. This increase is in all cases due to the decrease in flux in the x-direction (parallel to the canyon). This will be further explored in section 4.4.

Figure 4.19b shows the average C_e value in the canyon, normalised by the value of $LAD = 0$ for perpendicular wind. While angled wind is only 20% worse than perpendicular wind, the air quality for parallel wind can be up to twice as bad for this street canyon.

4.3. Facade concentrations

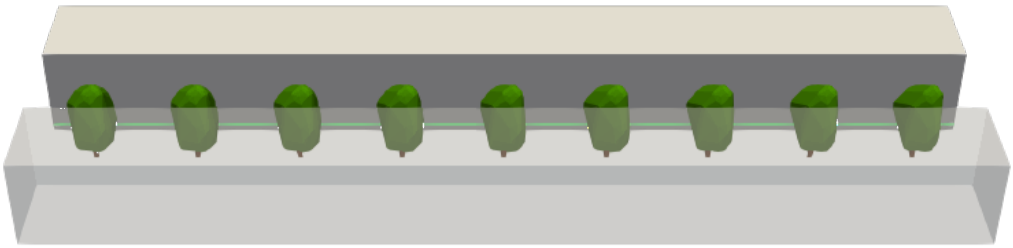

Figure 4.20: Line at 1.75 m at which C_e values are taken. The values are taken for both facades, and the source is on the eastern side.

The normalised concentrations of C_e at 1.75 m height are shown in Figure 4.21 for each wind direction and both sides of the street. The reference profile is that for $LAD = 0$ and is shown in the dotted lines. The non-normalised plots have already been discussed in section 4.1. It is no surprise that some of the features discussed are also relevant in the normalised plots, like the recirculation-induced spikes for parallel wind (Figure 4.21a). C_e values reach over five times as high in this region, with most values being at least two times as high for LADs 1.0 and 2.2. The trends for the normalised values are similar on the west facade, but the absolute values there are two to three times lower than on the east facade, according to the reference profiles.

Figure 4.21b shows the normalised lines for angled wind. The behaviour can be best explained with the velocity profiles for this wind direction, which are shown in Figure 4.22. They are taken at the y-value of the source. At the beginning of the street, the wind velocity is reduced most drastically by the presence of trees, which also results in higher facade concentrations. From the $x = 0$ point onwards, the wind speed profiles for LADs 1.0 and 2.2 are very similar. The normalised facade values of C_e are also almost identical in this region.

Like the parallel wind cases, a spike in C_e occurs after some distance. For angled wind, it might be due to a combination of the trees and the buildings, as the spike is also present for the $LAD = 0$ case. For the higher LADs, the spike is stronger and occurs earlier in the street, also referencing back to Figure 4.12. There is no significant recirculation in this region, even for high LAD. Therefore, the normalised values do not exceed 2 here. These normalised values of 1.5-2 are similar to those found earlier in the street, which were due to the decreased wind speed.

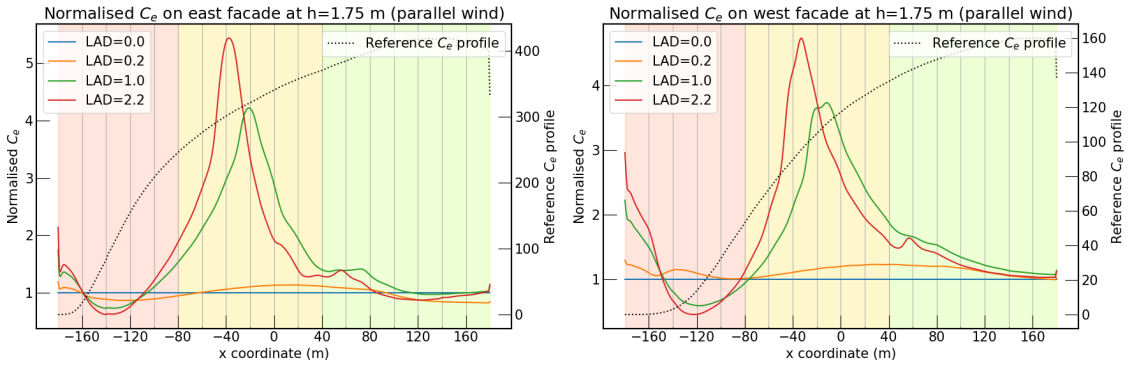

(a) Parallel

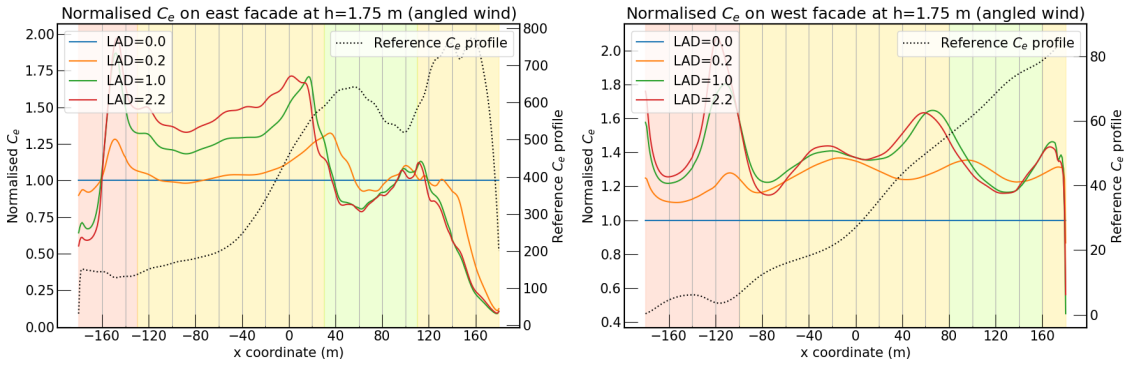

(b) Angled

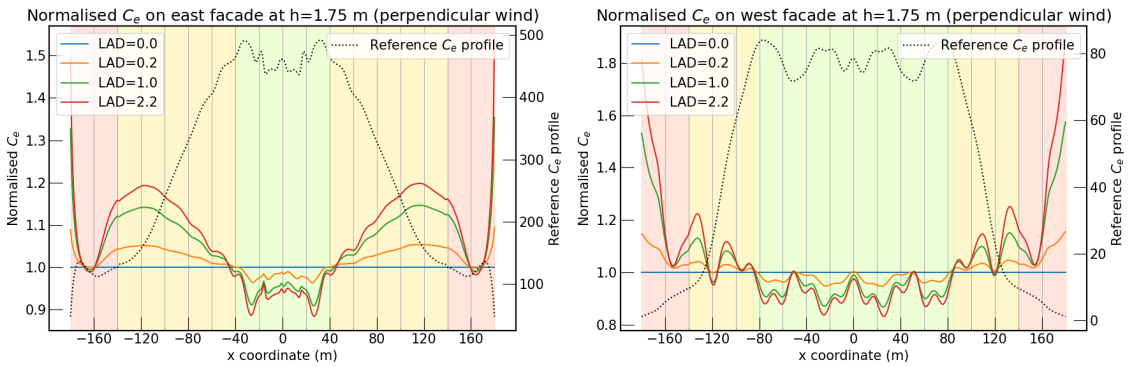

(c) Perpendicular

Figure 4.21: Normalised facade concentrations C_e at 1.75 m height for each wind direction and both facades

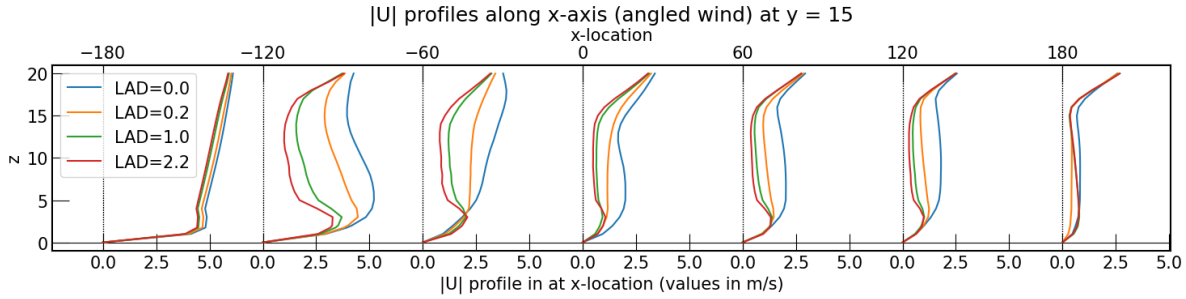

Figure 4.22: Wind speed profiles along the canyon for angled wind

A final interesting thing to note about angled wind is the slight influence of trees on the normalised lines. It shows very subtle spikes at the locations of the trees, which become more pronounced with an increase in LAD. This is not visible, however, on the west facade. There, the absolute values of C_e are also much smaller than on the east facade.

As for the mean concentrations in section 4.2, the trees cause a decrease in air pollution for perpendicular wind, although small, as visible in Figure 4.21c. In the regions in the middle of the street, where the influence of the open boundaries at the ends is smallest, the influence of the trees becomes more pronounced. Although the absolute values of C_e are highest in this region, they are 10-15 % lower at the trees' locations.

Figure 4.23 shows the average facade concentrations C_e varying with height. This was done for both sides of the canyon. Averages were taken over the full length of the canyon. As can be seen, the biggest influence of LAD is found for parallel wind and the source-side facade. For angled wind, a significant impact is found for the concentrations on the west facade. This impact, however, is one order of magnitude lower than that of parallel wind in terms of absolute values (12 vs. 200). In the other cases, averaging over the whole length of the canyon diminishes the effect of LAD, with most lines almost overlapping each other. The same trend with LAD is still evident as in the previous graphs. Higher LAD results in higher mean C_e on the facades, except for the west facade and perpendicular wind. This means that varying the height from which the lines in Figure 4.21 are taken does not alter the trends in absolute or normalised values.

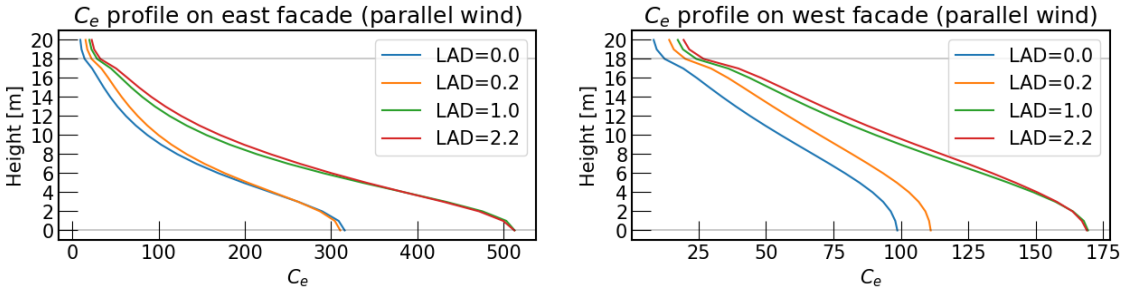

(a) Parallel

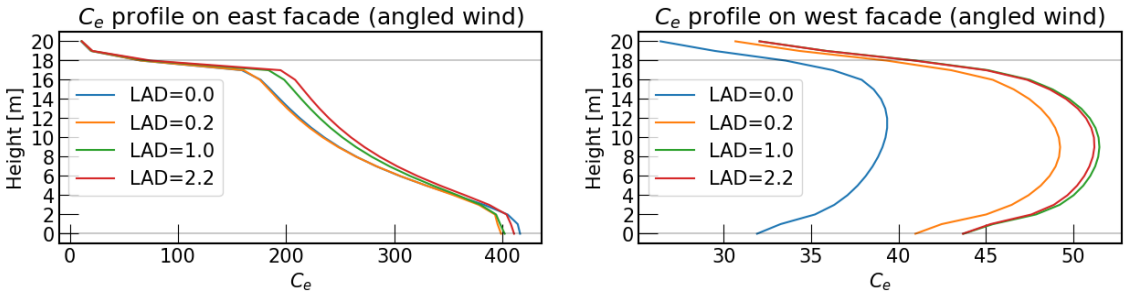

(b) Angled

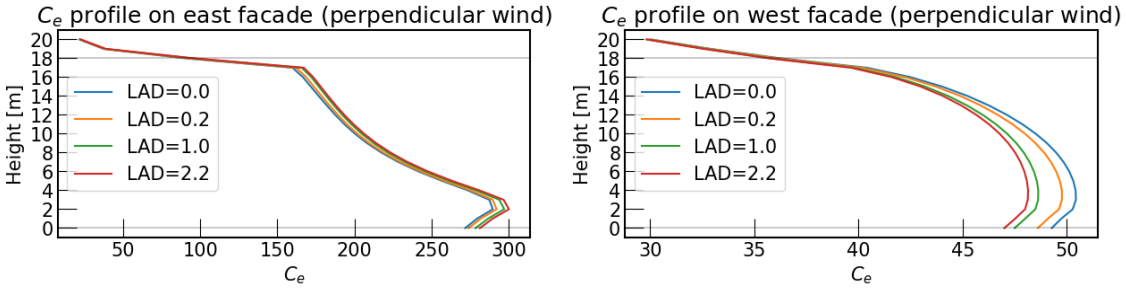

(c) Perpendicular

Figure 4.23: Mean facade values of C_e over the height of the buildings on both sides of the street. The means were taken over the full length of the street.

4.4. Mass flux

4.4.1. Mass flux out of canyon

To calculate mass fluxes out of the canyon, an extended boundary box is used, as explained in section 3.3, and illustrated in Figure 4.24. This gives a total of six boundaries (including the terrain), but for the purpose of this research, we are only interested in the mass fluxes at the borders of the canyon. These are both street ends and the top. Therefore, certain assumptions are made. In the example picture, the western outlet is split into three parts. The flux that passes through the orange part, for example, is assumed to have left through the southern end of the canyon. These values are added together. The same is done for the light blue part and the top flux, as well as the red part and the north flux. The same assumptions apply to the eastern boundaries.

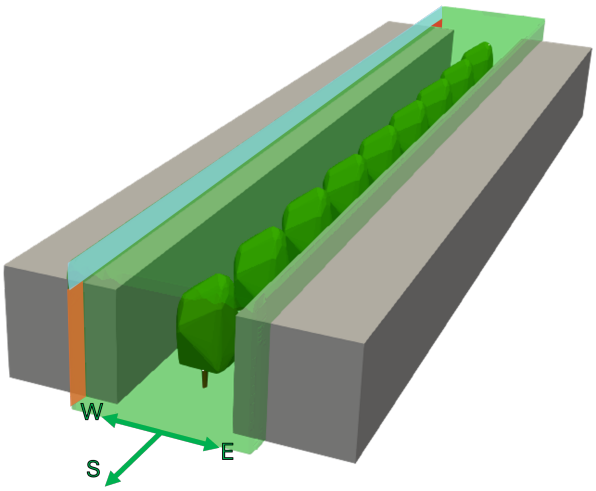

Figure 4.24: The bounding box is extended by 1 m and split into different sections

For each of the three boundaries, the mass flux into the canyon and out of the canyon is determined and plotted in Figure 4.25. For easier comparison, all values are normalised such that the net mass flux adds to 100.

For all wind directions, the amount of C_e that leaves through the top of the canyon grows with LAD. For parallel wind, the mass flux through the top almost doubles. This might sound like a good thing, as it could suggest that less pollution will remain in the canyon. However, it is a consequence of decelerated flow within the canyon. This is what allows more pollution to accumulate. Less pollution is able to leave the canyon through the ends, so the flux at the top increases. As shown in Figure 4.19b, the mean concentrations in the canyon grow with LAD, confirming that the increased vertical flux is not a sign of improved vertical ventilation.

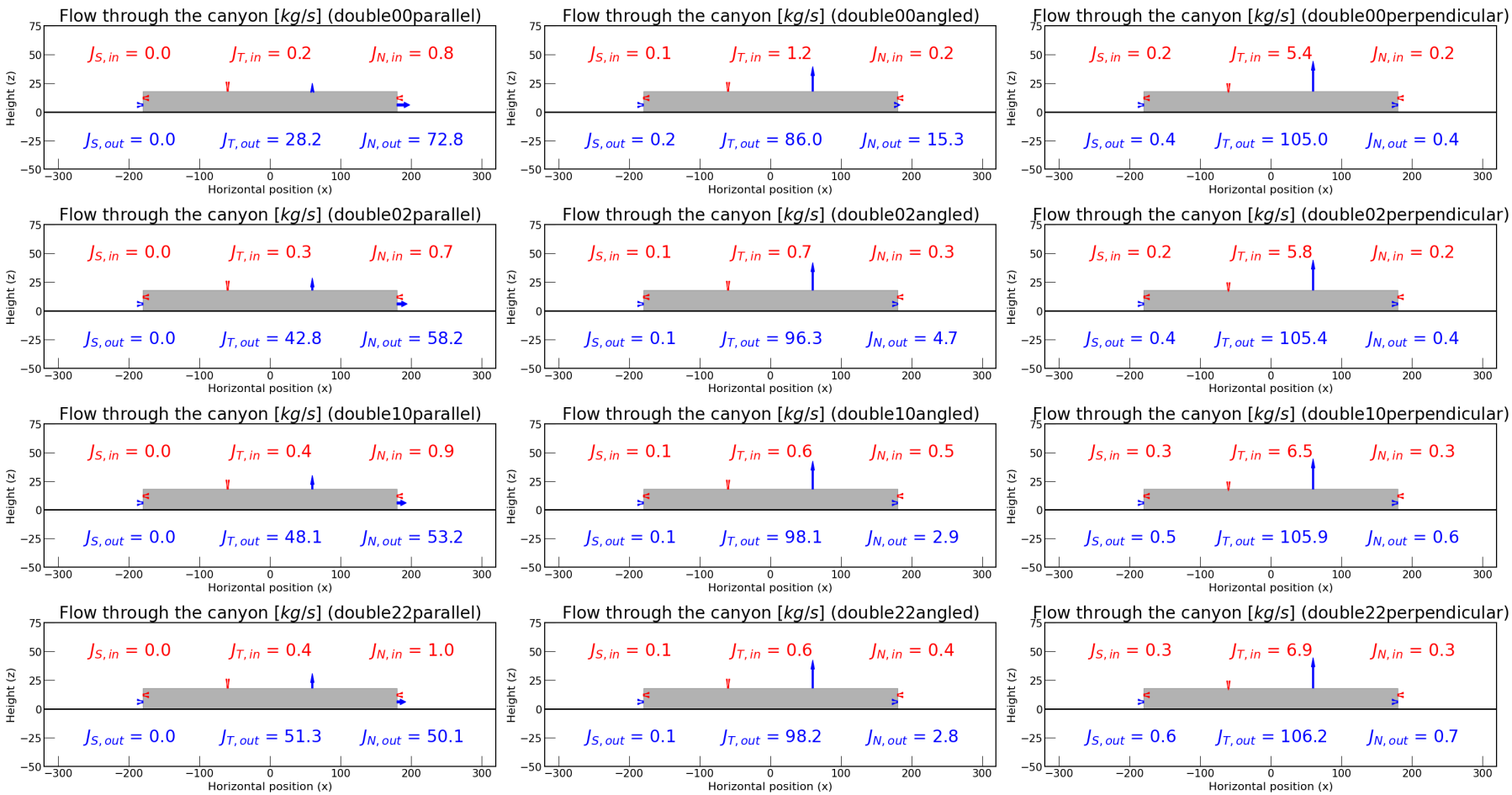

Figure 4.25: Mass fluxes into and out of all boundaries. Left column: parallel wind, middle column: angled wind, right column: perpendicular wind. The LAD increases per row.

Figure 4.25 also shows the amount of C_e that enters the canyon on each boundary. This is recirculating pollution. Paradoxically, the cases with the highest flux re-entering the canyon (higher LADs for perpendicular wind and lower LADs for parallel wind) have the best air quality according to the mean C_e. The high flux is in this case caused by high vertical particle velocities. Plotting the vertical velocities of particles for perpendicular wind at 2 m from the walls (Figure 4.26 and Figure 4.27) shows that the velocities are slightly higher with LAD in the regions with the highest concentrations. In these plots, that is for the x-locations from [-54, -18, 18, 54]. This is also in the zone where the influence of trees is most clear (as seen in Figure 4.3). These increased velocities increase the ventilation efficiency. This was also evident from Figure 4.19, where perpendicular wind is the only wind direction for which an increased concentration C_e at 18 m is paired with a decreased mean canyon concentration.

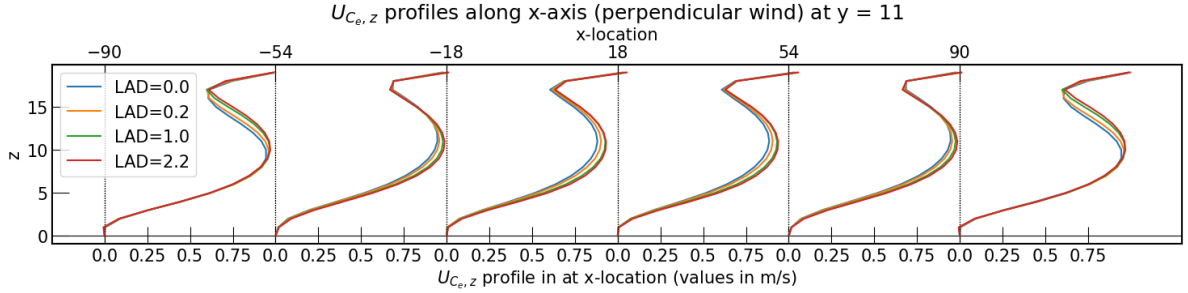

Figure 4.26: Vertical component of particle velocity U_{C_e} with height and for different x-locations along the canyon, 2 m from the eastern building

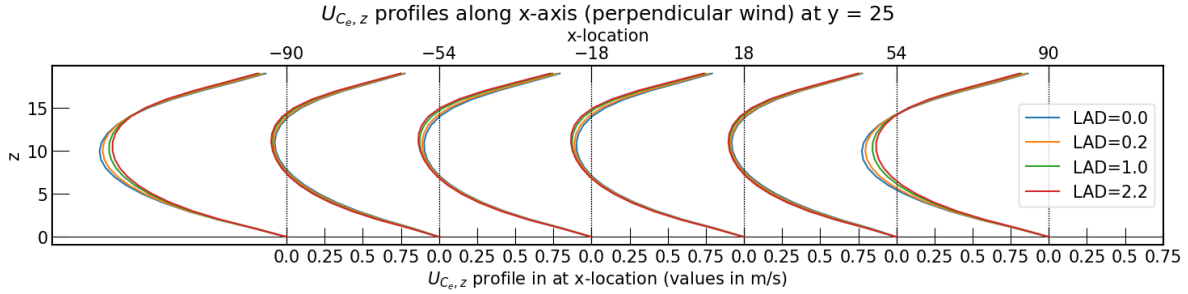

Figure 4.27: Vertical component of particle velocity U_{C_e} with height and for different x-locations along the canyon, 2 m from the western building

This vertical component of the particles is not the only reason less accumulation of C_e takes place. The lateral velocity component is also important. As can be seen in Figure 4.28, the velocities in x-direction are directed inward. The red regions indicate movement to the right, whereas the blue regions indicate movement to the left. Zooming in on the section between $x = -90$ and $x = 0$ and plotting the lateral velocity profiles, we see that lateral transport of C_e reduces with LAD (Figure 4.29).

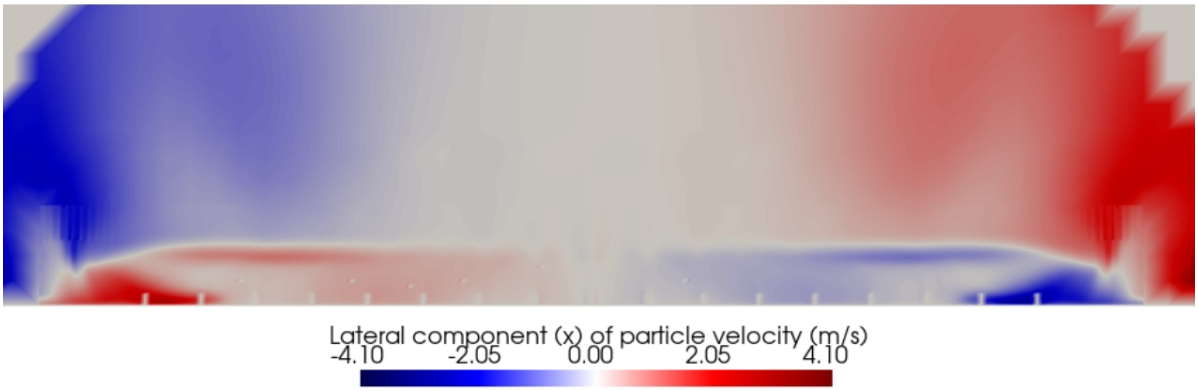

Figure 4.28: Lateral component of particle velocity $U_{C_e,x}$ for perpendicular wind and $LAD = 0$

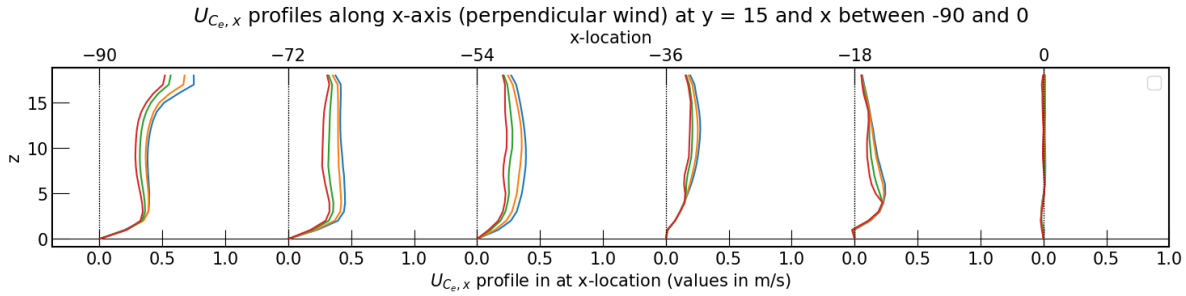

Figure 4.29: Lateral component of particle velocity (along x-axis) for different LADs and perpendicular wind

This is lastly shown in Figure 4.30, where most regions within the canyon are blue. This indicates lower lateral flux. Together with the improved vertical mixing, this is why the concentrations found for perpendicular wind are lower with higher LAD.

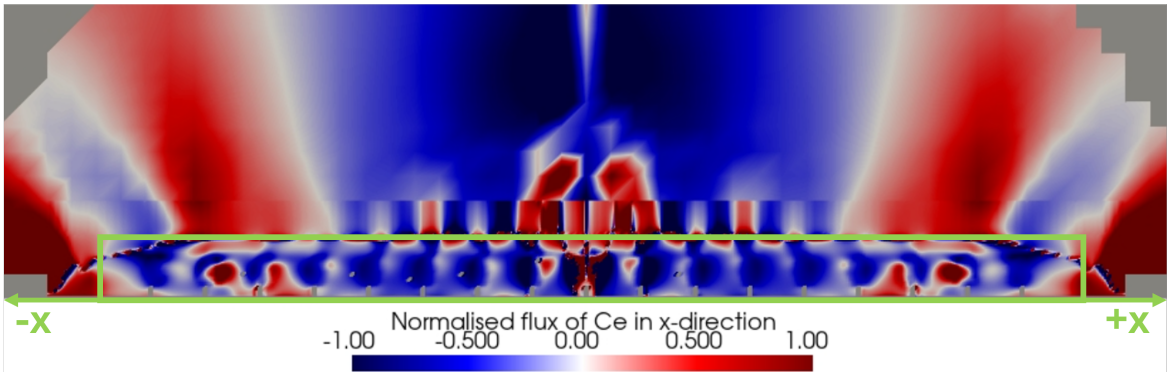

Figure 4.30: In most places within the canyon (green outline), a lower lateral flux is observed. LAD = 2.2 with perpendicular wind normalised by LAD = 0.

Making the same plot for parallel wind results in Figure 4.31. Here as well, reduced lateral transport is observed. In this case, however, this is not a good thing, as parallel wind relies on lateral transport for ventilation, contrary to the perpendicular case.

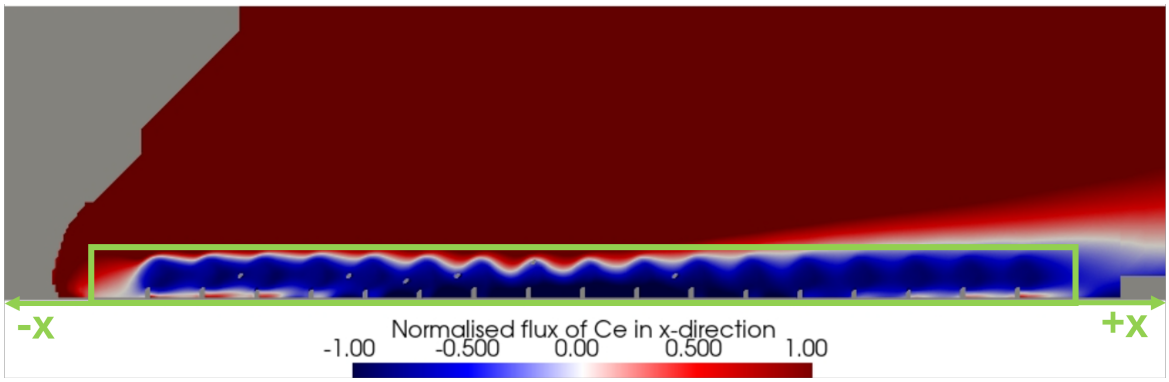

Figure 4.31: For parallel wind, lateral transport is also reduced in most of the canyon. If the normalised flux is smaller than -1, it indicates movement to the left. Otherwise it is movement to the right.

We can also plot where the C_e leaves the canyon through the top. This is shown in Figure 4.32. The plot for mass flux through the top of the canyon resembles the one for concentrations at the facades in Figure 4.21a. In the recirculation zone, significant vertical mixing occurs, driving vertical transport through the top, even though a substantial portion of the particles remains within the canyon, accumulating. After this zone, where the parallel flow starts stabilising again, the flux through the top is similar to that of the LAD = 0 case, which is evident from the normalised graphs in Figure 4.32b. The influence of the trees is also clear. Right before a tree, the vertical

flux is increased, as the air flow is partly redirected around the canopy. This also forces some C_e downwards. An investigation of the mass flux glyphs for the whole canyon, parallel wind, and $LAD = 2.2$ is shown in Figure 4.35.

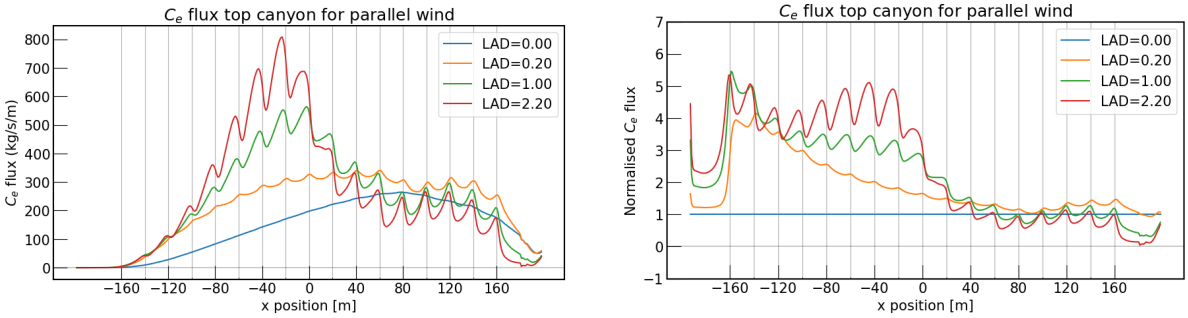

(a) Mass flux top canyon for parallel wind

(b) Normalised mass flux top canyon for parallel wind

Figure 4.32: Mass flux at the top of the canyon (18 m for parallel wind

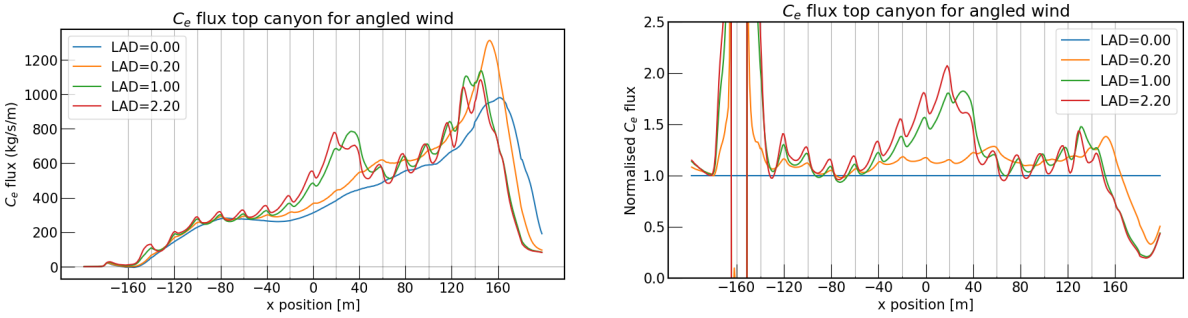

(a) Mass flux top canyon for angled wind

(b) Normalised mass flux top canyon for angled wind

Figure 4.33: Mass flux at the top of the canyon (18 m for angled wind

Like the cases for parallel wind, the flux through the top of the canyon for angled wind resembles its plot for concentrations along the length of the street. For angled winds, the same vertical particle velocities occur as for perpendicular wind, with upward transport on the windward side of the canyon and downward transport on the leeward side. This increases the flux of C_e through the top. Since there are no recirculation zones, as found for parallel wind, the pollutants accumulate for a longer part of the street length. This results in the end in higher absolute fluxes near the end of the canyon. Only at the end of the street, some recirculation occurs as a boundary effect, so here the values of C_e and J_{top} rise quickly.

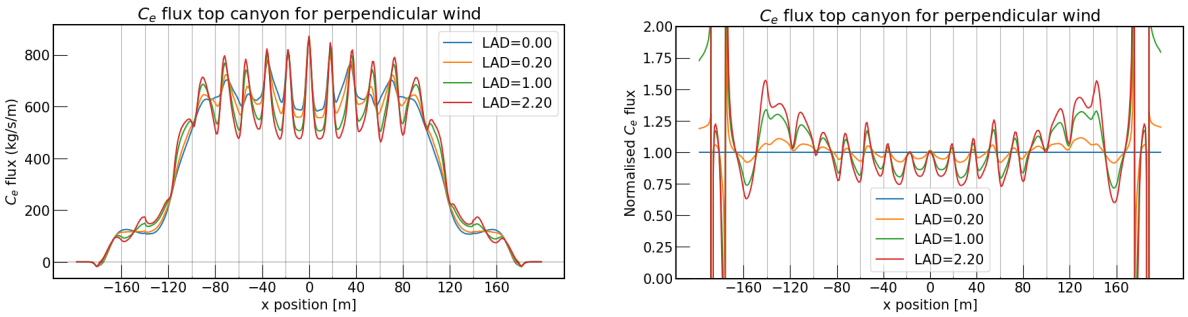

(a) Mass flux top canyon for perpendicular wind

(b) Normalised mass flux top canyon for perpendicular wind

Figure 4.34: Mass flux at the top of the canyon (18 m for perpendicular wind

At the trees' locations, the outflux of C_e spikes for perpendicular wind. The magnitude of this flux out of the canyon is similar for all LADs. In between trees, lower flux out the canyon is found with increasing LAD. This is because of lower absolute values of C_e and because of the higher flux of C_e re-entering the canyon.

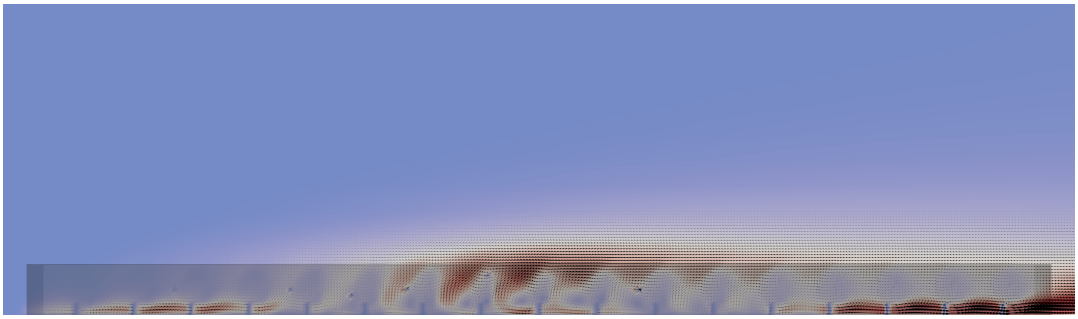

(a) The whole canyon can be split into three zones.

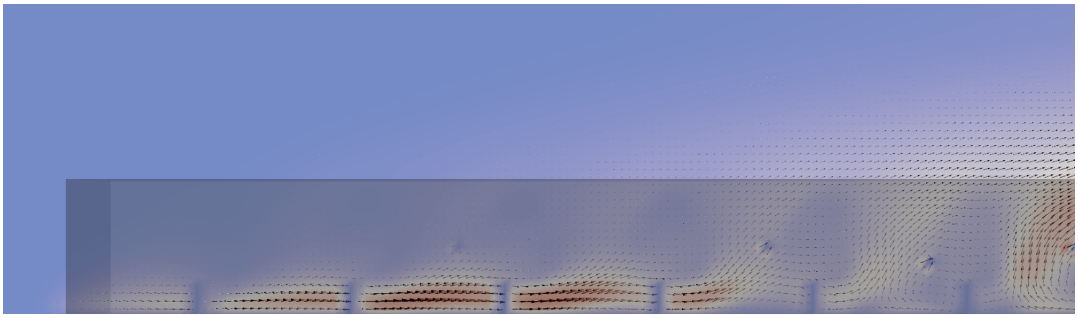

(b) The entering zone is characterised by first accumulation, but then a sudden vertical transport induced by the stagnated flow in the recirculation zone.

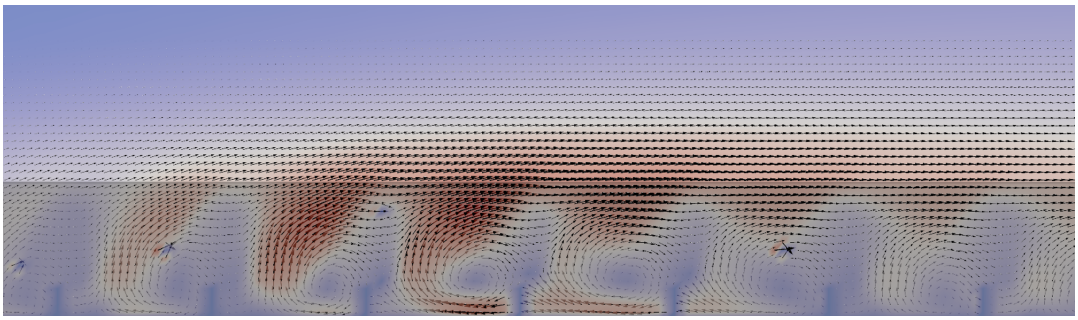

(c) In the recirculation zone reversed flows occur for U_{C_e} near ground level. Values of C_e rise, which results in a magnified flux through the top of the canyon.

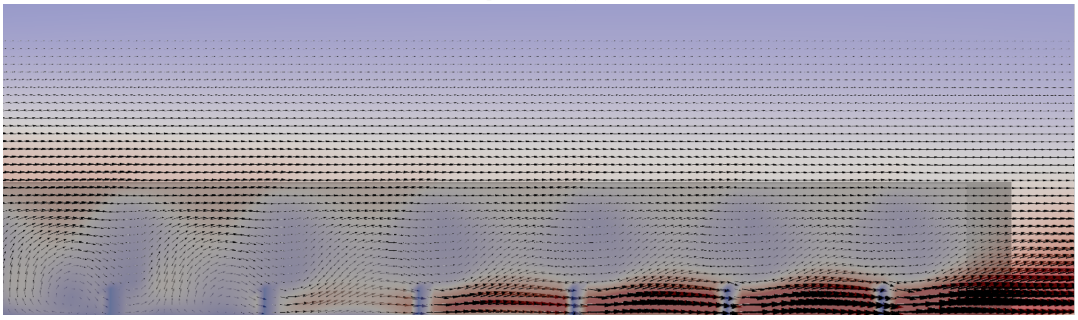

(d) In the accumulation zone, the flow has become more stable, meaning there is time and space for C_e to accumulate along the length of the canyon.

Figure 4.35: Glyphs for U_{C_e}, multiplied by quantity C_e to obtain the mass flux glyphs. The slice is taken halfway (through the trees)

4.5. Seasonality

The C_e results for the eastern facade, like in Figure 4.21 in section 4.3 are used in the calculations for a whole year. As mentioned in section 2.6, C_e and C_w are interchanged based on wind direction, but all values represent the concentrations of C_e on the nearest facade from the source. The average of the line at 2 m is put into the table, according to Equation 2.31. This is done for eight different street orientations from [0°, 45°, 90°, 135°, 180°, 225°, 270°, 315°], where 0° is the street facing north-south with the source on the east and every angle is into the clockwise direction. The monthly averages are computed for three different scenarios:

1. No trees ($LAD = 0$) vs. coniferous trees ($LAD = 0.2$) vs. deciduous trees ($LAD = 1.0$)
2. No trees ($LAD = 0$) vs. coniferous trees ($LAD = 0.2$) vs. deciduous trees ($LAD = 2.2$)
3. No trees ($LAD = 0$) vs. coniferous trees ($LAD = 1.0$) vs. deciduous trees ($LAD = 2.2$)

As explained in section 2.6, wind speed and direction are the most important meteorological variables used for estimating daily values of C_e. Since all weather stations in the Netherlands show the same trend in wind speed, with stronger wind speeds in winter than in summer (Figure 4.36), only one station was used for the plots. This is station 344 at Rotterdam Airport.

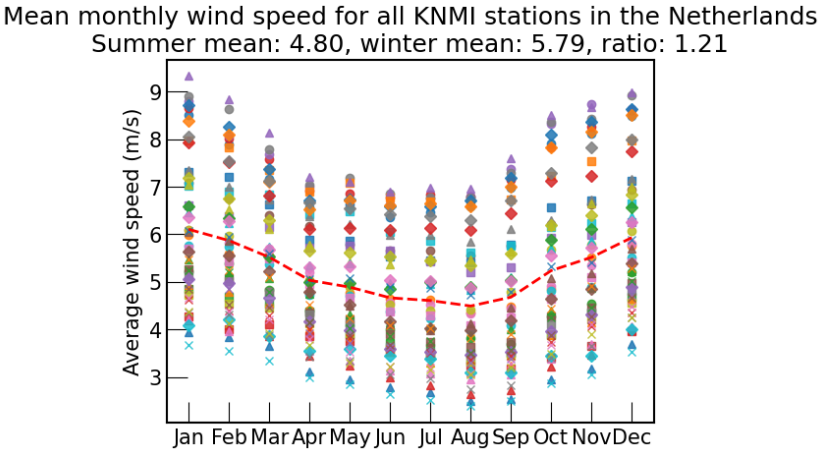

Figure 4.36: All weather stations in the Netherlands show the same trend of stronger winds in winter

The wind roses for station 344 are shown in Figure 4.37. There, some differences in wind can be seen per month. As said, wind speeds are stronger in winter. Also, there is a dominant wind direction from the south-west. This one is especially strong in the winter months. Additionally, during the months of November to March, the wind roses are remarkably similar to one another.

In section C.1, the plots are displayed for all above mentioned scenarios. Three plots are selected to summarise the conclusions, see Figure 4.39. Firstly, the scenarios for $LAD = 0$ and $LAD = 0.2$ (Figure 4.39a) are very similar in terms of mean facade concentration, as are the scenarios for $LAD = 1.0$ and $LAD = 2.2$ (Figure 4.39b). Hence, the lines almost exactly overlap for these LADs. Thus, the step from $LAD = 0.2$ to $LAD = 1.0$ is the most important and impactful.

Generally, lower concentrations are observed in winter due to increased wind speeds. Even though wind speeds are relatively low in the summer months, sometimes a dip in concentrations is found. This is, because wind direction plays an important role here. Some wind directions are worse than others for the concentrations of C_e on the facade closest to the source. Parallel wind is always bad for facade C_e. In the cases of angled and perpendicular wind, it depends on the way the wind circulates through the canyon. The vortex created within the street canyon either transports pollutants towards the facade or away from the facade. In Figure 4.38, the wind directions are depicted for an arbitrary canyon orientation. Any wind direction in red is in the bad zone. In months with relatively little wind from this zone, lower concentrations can be found. This applies, for example, to the month of July. If the street is oriented at 0°, 45°, or 315°, a dip in facade concentrations is found, see Figure 4.39c.

Over the whole year, streets with deciduous trees of LADs 1.0 and 2.2 are 10-17% worse than a street with no trees, in terms of facade concentrations. Coniferous trees have either a negligible impact for $LAD = 0.2$, or have a significant impact of 15-28% worse facade concentrations for $LAD = 1.0$.

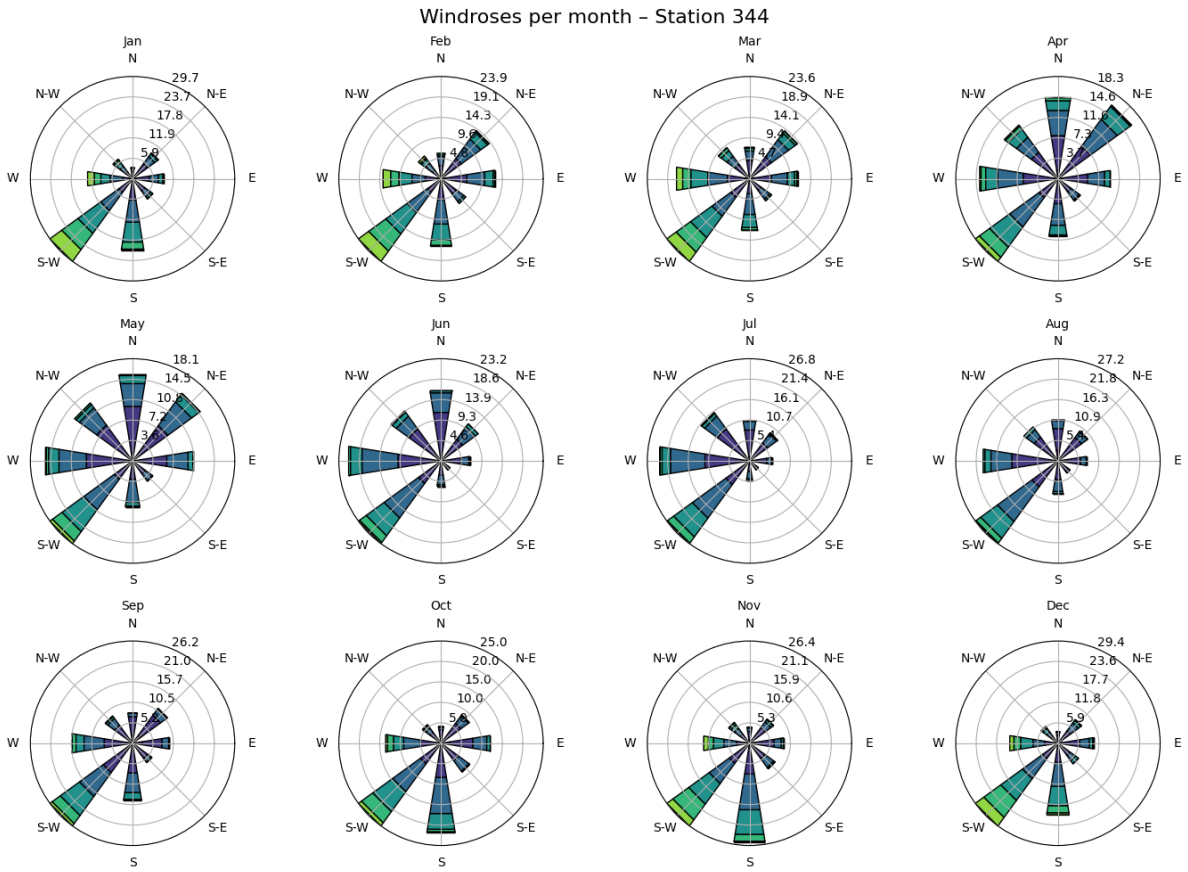

Figure 4.37: Wind roses for KNMI station 344 at Rotterdam Airport

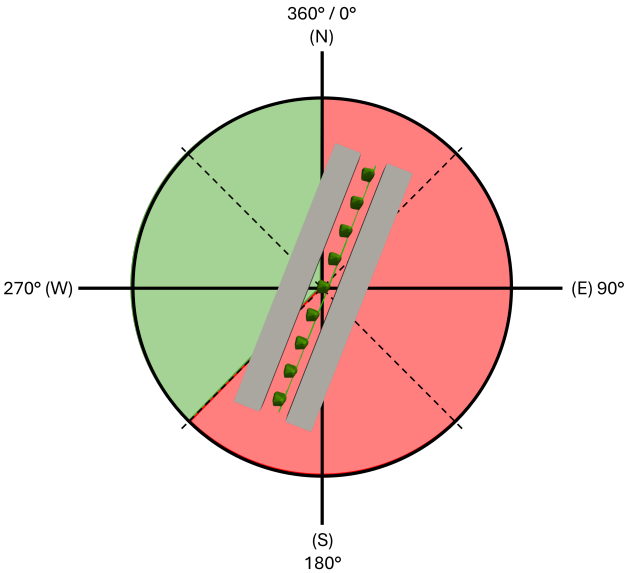

Figure 4.38: For the pollution from a source on the right-hand side of the trees, wind coming from the red region leads to significantly higher concentrations C_e on the right-hand side building. The angle in the illustration is arbitrary, and the regions rotate with the orientation of the street.

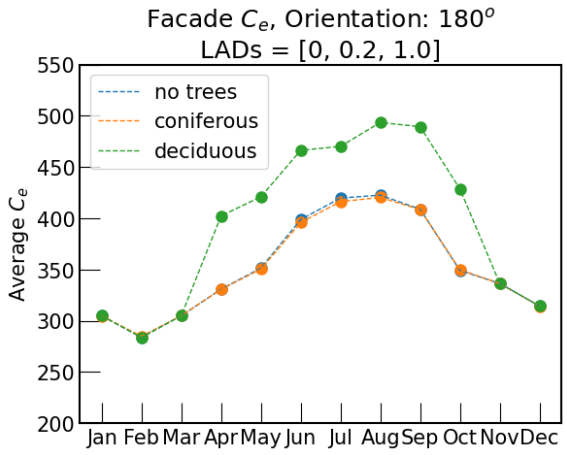

(a) Mean monthly facade concentrations C_e for LADs 0.0 vs. 0.2 vs. 1.0 and ϕ_{street} = 180°

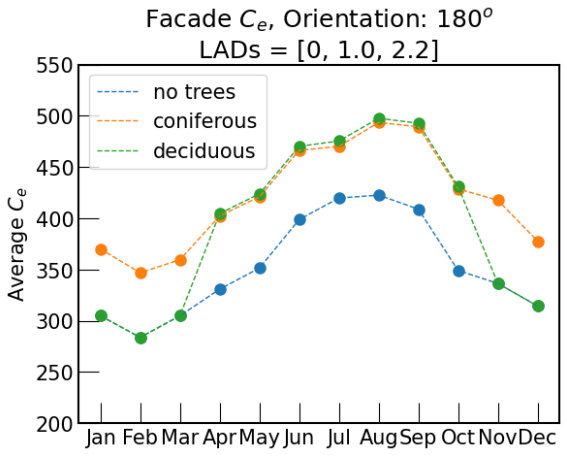

(b) Mean monthly facade concentrations C_e for LADs 0.0 vs. 1.0 vs. 2.2 and ϕ_{street} = 180°

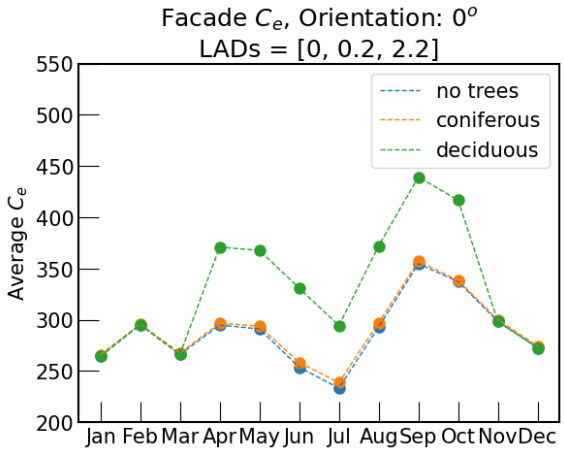

(c) Mean monthly facade concentrations C_e for LADs 0.0 vs. 0.2 vs. 2.2 and ϕ_{street} = 0°

Figure 4.39: Monthly mean facade C_e for different scenarios

Applying the same method, but using the mean value of C_e in the canyon below 2 m (Figure 4.40) gives similar results. The differences between LAD values are enhanced, so now there is a noticeable difference between $LAD = 0$ and $LAD = 0.2$. Coniferous trees with $LAD = 0.2$ are now 6-7% worse than no trees at all. Coniferous trees with $LAD = 1.0$ now reach yearly averages 24-36% higher than the case with no trees. Deciduous trees with $LAD = 1.0$ are now 15-22% worse, and those of $LAD = 2.2$ 16-23%. All plots are shown in section C.2 with a selection in Figure 4.41 for which the same situations were chosen as Figure 4.39.

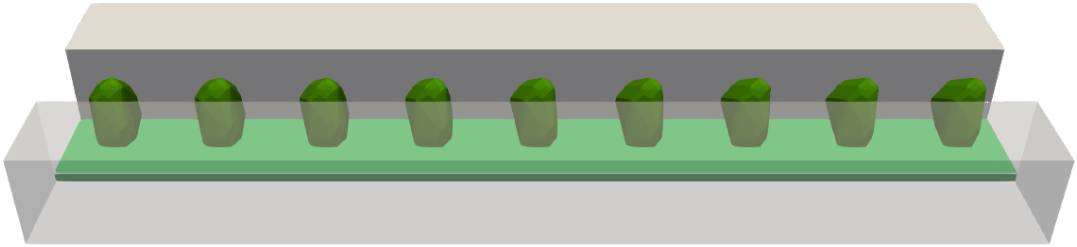

Figure 4.40: Volume of the street canyon section below 2 m

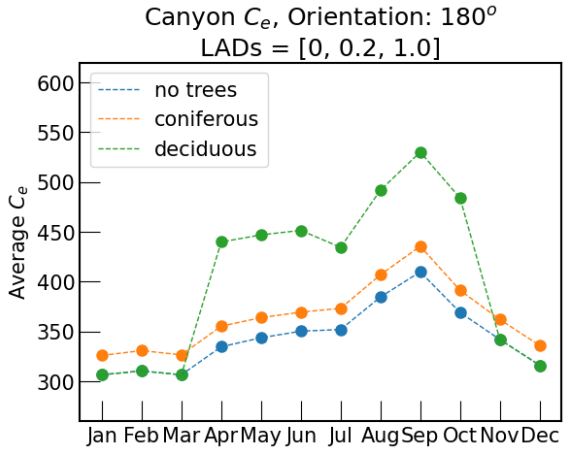

(a) Values for $LAD = 0$ and $LAD = 0.2$ differ more for the mean canyon concentration below 2 m

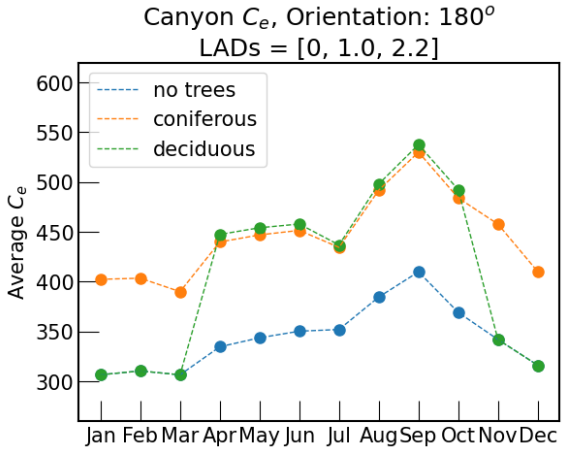

(b) Values for $LAD = 1.0$ and $LAD = 2.2$ are still almost identical for the mean canyon concentrations below 2 m

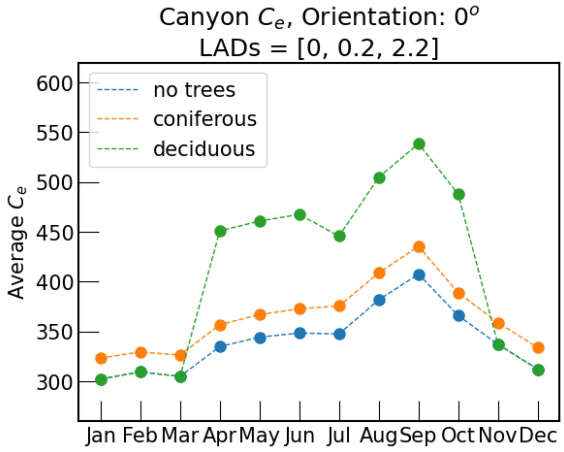

(c) In winter months, a lower concentration is observed, as well as for months with favourable wind

Figure 4.41: Different street canyon orientations and LAD configurations show different behaviour

5
Discussion

Model input and interpretations of results

This research was based on a steady RANS model of an atmospheric wind flow model. This method has its benefits and its limitations. It is the most simplistic of the considered models, which makes it computationally the only feasible one for the used domain and the number of simulations. However, the simplicity comes at a cost of detail. Due to averaging over a long time span, it does not account for any seasonal or diurnal variations. These include the height of the atmospheric boundary layer, convective mixing due to temperature differences and background pollution. These meteorological variables are all relevant to the pollution levels in the street, but not feasible to include in a time-independent steady RANS model. Thus, for the purpose of this research, excluding these variables is reasonable, but they are important to consider when interpreting the results.

Therefore, it is important to note that this research only describes the differences in how pollutants emitted within the street canyon disperse. If the results describe a 50% increase, for example, this does not imply a 50% increase in the actual air pollution. The actual air pollution in a real-life street is the sum of the pollution from the street itself, from other nearby sources, and background pollution. These other types of pollution are highly variable throughout the year. Considering the other seasonal variables, convective mixing and ABL height, it is assumed that within the canyon, turbulent mixing is dominant over convective mixing. That way, these seasonal differences are neglected.

Another modelling choice was not to include dry deposition of particles onto leaves. This was done under the assumption that the aerodynamic effects of trees outweigh the effects of deposition (Vos et al., 2013). However, some studies suggest that the effect of deposition is not negligible (Xue and Li, 2017). This could affect the results in a way that the pollutant concentrations are overestimated.

Finally, many formula constants used in the modelling are based on empirical values from literature. They may not be 100% applicable to this specific case, even though they may have been verified in real-life measurements. Also, the use of a $k-\varepsilon$ turbulence model, although most used for atmospheric simulations (Hargreaves and Wright, 2007), influences the obtained results.

Geometries

This research was conducted with specific design choices regarding the canyon. These choices have a significant impact on the obtained results and the way some aerodynamic behaviours occur. These design choices for geometries are:

- *Simplistic geometries*. The buildings used in this study are of the lowest level of detail. Thus, they do not accurately represent typical Dutch houses. This may lead to an over-prediction of wind speed, but an under-prediction of joint exceedance probability of velocity and turbulence levels in a study for pedestrian wind comfort by Patil and García-Sánchez (2025). This quantity is also relevant for pollutant transport.
- *No geometries around buildings*. This means that the wind is unobstructed before entering the canyon. This is rarely the case in real-life cities, which are fully built up. For this reason, the flow takes a long time to stabilise, and the effects of the open ends of the canyon are clearly visible for a long distance into the canyon.
- *Aspect ratio of* $1/1$. The aspect ratio of 1 is not an uncommon aspect ratio, but it is one out of many possibilities. The aspect ratio significantly affects the amount of air that enters the canyon and how the wind flows between the buildings. This aspect ratio is favourable here for perpendicular wind as it creates a single vortex with effective transport of C out of the canyon.
- *Trees*. These results are for one specific tree, which is a tall as the buildings around it. The trees are in the middle of the street, and the distance between the trees is approximately the same as their height. This

may again favour perpendicular wind and disadvantage parallel wind through the way recirculation vortices form between the trees.

- LAD *values of trees*. The chosen LAD values have been supported by the results being predictable with LAD for a single-length case. For example, the results of the $LAD = 0.6$ case were consistently between those of $LAD = 0.2$ and $LAD = 1.0$. The double-length case, however, exhibits different behaviours for parallel wind after $LAD = 1.0$. It introduces recirculation, which did not occur before. Without knowing what LAD value is critical for the recirculation effect to occur, it is impossible to predict anything about the behaviour for LADs between 0.2 and 1.0.
- $LAD = 0$ *case run with trunks*. The case 'with no trees' is not actually a case with no trees. It was modelled as a trunk with no leaves. This was done to improve running time by allowing the use of the same mesh. However, the influence of the trunks is significant, with visible spikes for the parallel wind cases. This is especially clear for the facade concentrations at 1.75 m height, since the trunks are 4 m tall themselves.
- *Source locations*. The sources are located close to the trees, with the tree canopies overhead. This does occur in real-life streets in the Netherlands, but more often, trees are next to the road and between the source and the buildings.
- *Wind directions*. More wind directions could give a more complete input for yearly results. Parallel wind and perpendicular wind result in very symmetrical cases. These cause extreme versions of the described phenomena, such as reduced lateral transport for perpendicular wind and extreme recirculation for parallel wind. These precise wind directions rarely occur, and having more nuanced angles would improve the results for seasonality.
- *Canyon length*. It is likely that the results could be even more general if we increase the canyon length even further, since boundary effects are still present for a large portion of the canyon. On the other hand, streets are rarely this long.

Output/processing

During the processing, some methodological choices were made that influence the results. Firstly, the choice of canyon length is a critical point. The single-length case does not exhibit the same aerodynamic phenomena as the longer cases, so it was not used for the results chapter. The triple-length simulations did not introduce new phenomena, so the double-length cases were chosen over the triple-length in favour of computing time.

A second important aspect is how the mean C was calculated and how it was used to explain what is happening. Different averaging domains within the canyon give different mean concentrations. Depending on the objective, certain domains were chosen. These include volume averages, plane averages, and line averages. Sometimes, only a section in the middle was taken, and sometimes, multiple of these domains were investigated to assess the impact of section choice. At all times, the section used for analyses was carefully considered to yield insightful results, but it is impossible to tell whether these choices were always the best.

Additionally, the interpolation of the *.vtk* results onto a Python mesh causes numerical inconsistencies. These were partly resolved by taking the extended volume box. However, this method is not ideal as assumptions need to be made as to where fluxes are coming from. Still, the error is not 0%, although it is deemed sufficiently small to draw conclusions.

For the seasonality investigation, some assumptions had to be made. For one, the scaling of C with U^{-1} is a very rigorous assumption that does not hold for much lower or much higher wind speeds. This is because the source and sink terms for U, k, and ε induced by trees are all non-linear with U. Phenomena like the recirculation for parallel wind would likely not occur with much lower wind speeds, even for high LAD. A. Jeanjean, Monks, and Leigh (2016) also found different results for low and high wind speeds, which confirms that this inverse linear relationship does not hold.

Additionally, three wind directions might not be sufficient. This gives only eight wind regions with drastically different results and occurring phenomena from one wind direction to the next.

Lastly, it is assumed that trees are leafless during the months of November to March. In the modelling, this is implemented in a binary way, where trees have all of their leaves in October, and the next day in November, they have lost them all. This is unrealistic, so the transition from summer to winter and back could be smoother, but would rely on even more assumptions about leaf loss.

6
Conclusion

The main question of this research is:

How does urban vegetation impact local air quality in an urban environment?

Answering the main question was approached by the following sub-questions:

1. How great is the influence of Leaf Area Density (LAD) on locally emitted $PM_{2.5}$ levels?
2. What are the concentration differences between a case with deciduous trees and one with coniferous trees, considering seasonal changes?

6.0.1. LAD

There is a clear difference in the aerodynamic effects for low LADs (0 and 0.2) and high LADs (1.0 and 2.2). For a low LAD of 0.2, the presence of trees gives similar results to a $LAD = 0$ case. The high values also give similar results to each other, but they are enhanced with the higher LAD.

Increasing Leaf Area Density has multiple effects on the dispersion of street emissions, depending on wind direction. In general, trees form an obstacle which reduces wind speeds within the canopy. This takes momentum out of the flow and forces more wind around. It limits airflow and mass flux in the x-direction (along the length of the canyon), but it stimulates the flow of vortices in the yz-plane, perpendicular to the x-axis, and induces vertical wind over or under the trees.

For perpendicular wind, in the middle region where both of these effects are most prevalent, this is advantageous, as it limits lateral accumulation and improves vertical pollutant transport. Increasing LAD reduces the pollutant concentrations in all investigated domains of the facades, the slice at 1.75 m ('nose-height') and the canyon volumes.

Parallel wind relies on wind in the x direction for its ventilation, so trees negatively affect this process. Furthermore, the reduced wind speeds in the x-direction and altered wind directions in the xz-plane (more upward wind upon entering the street, and more downward-directed wind soon after), cause recirculation zones where pollutant concentrations accumulate drastically, with facade values between 2-5 times as high as the $LAD = 0$ case. When the wind becomes more stable after the recirculation zone, trees limit vertical transport again, leading to accumulation along the length of the source.

For angled wind, both the limitation of ventilation in the x-direction and the increase of vertical transport occur. The facade experiences a spike in C due to reduced wind speeds along the length of the canyon, but it profits from the enhanced cross-street vortex ventilations. Thus, the effects lie somewhere between those for the other wind directions. For high LAD, facade concentrations are up to 50% worse in most parts of the canyon. In areas where the highest absolute values of air pollution are found, the effect of LAD can diminish or even improve air quality.

In terms of concentrations at 1.75 m and average canyon concentrations, perpendicular is the best wind direction, followed by angled wind. Parallel wind is, in this case, the worst by a factor of 3 for nose height (Figure 6.1a), and >2 for canyon mean.

Calculating mass fluxes provides an in-depth understanding of how pollutants move through the canyon, out of the canyon and back into the canyon. The total mass fluxes on the boundaries, however, are by themselves not a reliable indicator of what is happening inside. Improved fluxes through the top of the canyon do not imply improved vertical mixing or lower canyon concentrations. It mostly means that lateral ventilation is reduced, so

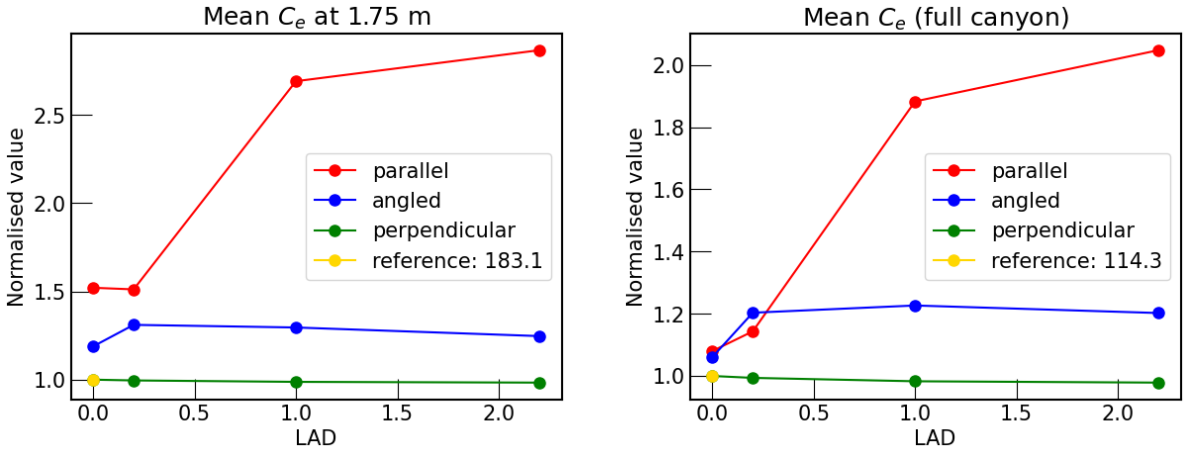

(a) Normalised values of mean C_e at *nose height*, for all wind directions and all LADs

(b) Normalised mean values of C_e within the entire canyon

Figure 6.1: Recalling Figure 4.14b and Figure 4.19b

more pollutants accumulate. This increase in C is what drives the flux. Mass fluxes within the canyon, on the other hand, are useful. They can explain why accumulation occurs in some scenarios, but not in others.

6.0.2. Seasonality

Since LAD increases the calculated pollutant concentrations in parallel and angled wind cases, the overall yearly means also increase with LAD. The positive effect of perpendicular wind is outweighed by the negative effects of the other winds. For this part of the research, it is especially important to note that the results only apply to the emissions from within the canyon.

For the yearly calculations, two pollutant inputs were tested:

1. Mean C_e on eastern facade at 2 m
2. Mean canyon C_e below 2 m

These are model choices. The same calculations could have been done with either C_e or C_w on either facade, or any defined domain. To emphasise the effect of this input, two scenarios were tested. Although this gives some insights with similar conclusions from both metrics, it is not entirely conclusive.

Some conclusions from the seasonality analysis were:

1. *Concentrations are lower in winter*. This is based on the wind speed, which is generally stronger in winter. Stronger wind speed increases the amount of air that dilutes the concentration. This does not necessarily mean that the total air quality in winter is better. Emissions from the canyon are dispersed better, but in general, background emissions are significantly higher during winter times. This is due to a smaller atmospheric boundary layer height, less convective mixing and more emissions from cars and homes.
2. *Concentrations are lower for favourable wind directions*. In the calculations, parallel wind and wind from the source-side direction lead to significantly higher facade concentrations. This is because all these winds induce fluxes from the source to the windward facade. Since some wind directions are more dominant than others, and these vary per month, street orientation is an important parameter when investigating monthly means. This is, again, not including background concentrations, which are also direction dependent. Wind coming from land has a higher background pollution than wind from the sea. This conclusion is also very dependent on the metric chosen for C. In the case of C_e on the eastern facade, this effect is very significant. For the case of mean C_e below 2 m, the effect is diminished.
3. *The concentrations are very LAD-dependent*. $LAD = 0$ and $LAD = 0.2$ cases give very similar results, as well as $LAD = 1.0$ and $LAD = 2.2$ cases. Since LAD is tree-dependent, coniferous trees and deciduous trees give different monthly results. For coniferous trees LADs of 0.2 and 1.0 were tested, where the first LAD has very little effect compared to the $LAD = 0$ case. $LAD = 1.0$ coniferous trees, on the other hand, have the worst effect over an entire year. These are 15-28% worse regarding facade concentrations, and

24-36% for canyon means. The behaviour of deciduous trees is season-dependent, because they lose their leaves in winter. In summer, they were tested with LADs 1.0 and 2.2. Even though the effect of deciduous trees is therefore always worse in summer, the reduced concentrations during the winter make deciduous trees only 10-17% worse on a yearly basis for facade concentration and 15-23% for canyon averages. All values are summarised in Table 6.1.

Tree type	**Coniferous**	**Coniferous**	**Deciduous**	**Deciduous**
LAD (m^2/m^3)	0.2	1.0	1.0	2.2
East facade at 2 m	0-1%	15-28%	10-17%	10-17%
Canyon mean below 2 m	6-7%	24-36%	15-22%	16-24%

Table 6.1: Increase in yearly C with respect to the LAD = 0 case

These are the values that were found for one specific station, Station 344 at Rotterdam Airport. Although it was concluded that the monthly trends in wind speed are similar for all stations in the Netherlands, the actual daily wind conditions vary per location. This means that the exact values found are not the same for the whole country, but the general conclusions do translate to other places.

6.0.3. Recommendations

For future work, it would be interesting to apply all methods to a real-life or a more complex geometric case. Many limitations of this research are related to the geometric design of the domain. Testing on a prototype would give more insight into how the conclusions from this research hold in other scenarios.

It is also necessary to run the simulations with a wider range of wind speeds to better understand the effect of LAD and to accurately capture seasonal variations. The inversely linear assumption of C with U was a convenient scaling available with the limited simulations, but for further research, it is highly recommended to run simulations with other wind speeds.

Also, to make statements about the real air quality, the results need to be related to background concentrations and other pollutant sources. It is challenging and time-consuming to calibrate these with field measurements, but it would allow for much more meaningful results.

This work could be improved with more realistic assumptions. It would likely have been better to incorporate dry deposition into the model. Also, with a mesh that would better match the Python grid, and even more time steps, some inaccuracies could be diminished. For example, the numerical errors on boundaries for mass fluxes could likely be reduced, allowing for more accurate calculations of transport and recirculation.

References

Bell, M. L. and K. Ebisu (2012). "Environmental Inequality in Exposures to Airborne Particulate Matter Components in the United States". In: *Environmental Health Perspectives* 120(12), pp. 1699–1704. DOI: https://doi.org/10.1289/ehp.1205201.

Blazek, J. (2005). "Chapter 7 - Turbulence Modelling". In: *Computational Fluid Dynamics: Principles and Applications (Second Edition)*. Ed. by J. Blazek. Second Edition. Oxford: Elsevier Science, pp. 227–270. ISBN: 978-0-08-044506-9. DOI: https://doi.org/10.1016/B978-008044506-9/50009-6.

Blocken, B. (2015). "Computational Fluid Dynamics for urban physics: Importance, scales, possibilities, limitations and ten tips and tricks towards accurate and reliable simulations". In: *Building and Environment* 91. Fifty Year Anniversary for Building and Environment, pp. 219–245. ISSN: 0360-1323. DOI: https://doi.org/10.1016/j.buildenv.2015.02.015.

Buccolieri, R. et al. (2018). "Review on urban tree modelling in CFD simulations: Aerodynamic, deposition and thermal effects". In: *Urban Forestry & Urban Greening* 31, pp. 212–220. ISSN: 1618-8667. DOI: https://doi.org/10.1016/j.ufug.2018.03.003.

Chen, G. et al. (2014). "OpenFOAM for computational fluid dynamics". In: *Notices of the AMS* 61.4, pp. 354–363. DOI: http://dx.doi.org/10.1090/noti1095.

Chen, J. and G. Hoek (2020). "Long-term exposure to PM and all-cause and cause-specific mortality: A systematic review and meta-analysis". In: *Environment International* 143, p. 105974. ISSN: 0160-4120. DOI: https://doi.org/10.1016/j.envint.2020.105974.

de Rooij, S. (2022). *Werk aan de winkel voor gezonde luchtkwaliteit voor alle Brusselaars*. URL: https://blog.uantwerpen.be/armoede-sociale-uitsluiting/werk-aan-de-winkel-voor-gezonde-luchtkwaliteit-voor-alle-brusselaars/.

European Commission (2021). *Pathway to a Healthy Planet for All - EU Action Plan: 'Towards Zero Pollution for Air, Water and Soil'*. URL: https://eur-lex.europa.eu/legal-content/EN/TXT/HTML/?uri=CELEX:52021DC0400.

European Environment Agency (2024a). *Exceedance of air quality standards in Europe*. URL: https://www.eea.europa.eu/en/analysis/indicators/exceedance-of-air-quality-standards#:~:text=More%20than%2083%25%20of%20urban,Organization%20air%20quality%20guideline%20values..

— (2024b). *Harm to human health from air pollution in Europe: burden of disease status, 2024*. URL: https://www.eea.europa.eu/en/analysis/publications/harm-to-human-health-from-air-pollution-2024#:~:text=In%202022%20in%20the%20EU,CI)%20was%20182%2C000%2D267%2C000..

— (2024c). *How air pollution affects our health*. URL: https://www.eea.europa.eu/en/topics/in-depth/air-pollution/eow-it-affects-our-health.

European Urban Initiative (2022). *Greening Cities*. URL: https://www.urban-initiative.eu/innovative-actions-greening-cities.

Fidelis (s.d.). *Turbulence Modeling Techniques In CFD – DNS vs LES vs RANS*. URL: https://www.fidelisfea.com/post/turbulence-modeling-techniques-in-cfd-dns-vs-les-vs-rans.

Franklin, J. (2024). *A Turbulence Modeling Deep-dive with Azore CFD's Lead Developer*. URL: https://www.azorecfd.com/blog/turbulence-modeling.

Fu, R., I. Pađen, and C. García-Sánchez (2024). "Should we care about the level of detail in trees when running urban microscale simulations?" In: *Sustainable Cities and Society* 101, p. 105143. ISSN: 2210-6707. DOI: https://doi.org/10.1016/j.scs.2023.105143.

Gromke, C. and B. Blocken (2015). "Influence of avenue-trees on air quality at the urban neighborhood scale. Part I: Quality assurance studies and turbulent Schmidt number analysis for RANS CFD simulations". In: *Environmental Pollution* 196, pp. 214–223. ISSN: 0269-7491. DOI: https://doi.org/10.1016/j.envpol.2014.10.016.

Gromke, C., B. Blocken, et al. (2015). "CFD analysis of transpirational cooling by vegetation: Case study for specific meteorological conditions during a heat wave in Arnhem, Netherlands". In: *Building and Environment* 83. Special Issue: Climate adaptation in cities, pp. 11–26. ISSN: 0360-1323. DOI: https://doi.org/10.1016/j.buildenv.2014.04.022.

Grylls, T. and M. van Reeuwijk (2022). "How trees affect urban air quality: It depends on the source". In: *Atmospheric Environment* 290, p. 119275. ISSN: 1352-2310. DOI: https://doi.org/10.1016/j.atmosenv.2022.119275.

Hargreaves, D. and N. Wright (2007). "On the use of the k–ε model in commercial CFD software to model the neutral atmospheric boundary layer". In: *Journal of Wind Engineering and Industrial Aerodynamics* 95.5, pp. 355–369. ISSN: 0167-6105. DOI: https://doi.org/10.1016/j.jweia.2006.08.002.

IdealSimulations (s.d.). *Turbulence models in CFD*. URL: https://www.idealsimulations.com/resources/turbulence-models-in-cfd/.

Itokazu, R. et al. (2025). "Exploring Ventilation Efficiency through Scalar Transport Equations with existing and new CFD-based indices". In: *Building and Environment* 277, p. 112942. ISSN: 0360-1323. DOI: https://doi.org/10.1016/j.buildenv.2025.112942.

Jbaily, A. et al. (2022). "Air pollution exposure disparities across US population and income groups". In: *Nature* 601(7892), pp. 228–233. DOI: https://doi.org/10.1038/s41586-021-04190-y.

Jeanjean, A., P. Monks, and R. Leigh (2016). "Modelling the effectiveness of urban trees and grass on PM2.5 reduction via dispersion and deposition at a city scale". In: *Atmospheric Environment* 147, pp. 1–10. ISSN: 1352-2310. DOI: https://doi.org/10.1016/j.atmosenv.2016.09.033.

Jeanjean, A. P. et al. (2017). "Air quality affected by trees in real street canyons: The case of Marylebone neighbourhood in central London". In: *Urban Forestry & Urban Greening* 22, pp. 41–53. ISSN: 1618-8667. DOI: https://doi.org/10.1016/j.ufug.2017.01.009.

Jin, S. et al. (2014). "Evaluation of impacts of trees on PM2.5 dispersion in urban streets". In: *Atmospheric Environment* 99, pp. 277–287. ISSN: 1352-2310. DOI: https://doi.org/10.1016/j.atmosenv.2014.10.002.

Kenjereš, S. and B. ter Kuile (2013). "Modelling and simulations of turbulent flows in urban areas with vegetation". In: *Journal of Wind Engineering and Industrial Aerodynamics* 123, pp. 43–55. ISSN: 0167-6105. DOI: https://doi.org/10.1016/j.jweia.2013.09.007.

KNMI (2025). *Daggegevens van het weer in Nederland*. URL: https://www.knmi.nl/nederland-nu/klimatologie/daggegevens.

Lalic, B. and D. T. Mihailovic (2004). "An Empirical Relation Describing Leaf-Area Density inside the Forest for Environmental Modeling". In: *Journal of Applied Meteorology* 43.4, pp. 641–645. DOI: 10.1175/1520-0450(2004)043<0641:AERDLD>2.0.CO;2.

Launder, B. and D. Spalding (1974). "The numerical computation of turbulent flows". In: *Computer Methods in Applied Mechanics and Engineering* 3.2, pp. 269–289. ISSN: 0045-7825. DOI: https://doi.org/10.1016/0045-7825(74)90029-2.

Madadi-Kandjani, E. (2016). *Cylinder mesh using blockMesh with m4 macro*. URL: https://www.ehsanmadadi.com/cylinder-mesh/.

Martín, F. et al. (2024). "Using dispersion models at microscale to assess long-term air pollution in urban hot spots: A FAIRMODE joint intercomparison exercise for a case study in Antwerp". In: *Science of The Total Environment* 925, p. 171761. ISSN: 0048-9697. DOI: https://doi.org/10.1016/j.scitotenv.2024.171761.

Mikati, I. et al. (2018). "Disparities in Distribution of Particulate Matter Emission Sources by Race and Poverty Status". In: *American journal of public health* 108(4), pp. 480–485. DOI: https://doi.org/10.2105/AJPH.2017.304297.

OpenCFD (2023). *Residuals*. URL: https://doc.openfoam.com/2306/tools/processing/numerics/solvers/residuals/.

OpenCFD Ltd 2025 and KEYSIGHT (2025). *OpenFOAM*. URL: https://www.openfoam.com/.

Our World in Data (2025). *Share of the population living in urban areas*. URL: https://ourworldindata.org/grapher/share-of-population-urban.

Patil, A. and C. García-Sánchez (2025). "Quantifying the impact of urban geometric detail for urban air mobility risk forecasting". In: *Sustainable Cities and Society* 132, p. 106750. ISSN: 2210-6707. DOI: https://doi.org/10.1016/j.scs.2025.106750.

Rentschler, J. and N. Leonova (2022). "Air Pollution and Poverty: PM2.5 Exposure in 211 Countries and Territories". In: *Policy Research Working Paper 10005*. URL: https://documents1.worldbank.org/curated/en/099338004182222681/pdf/IDU0972f137406bef043fa0bcbb0d345e0a30849.pdf.

RIVM (2025a). *Fijnstof 2022 (PM10)*. URL: https://nationaalgeoregister.nl/geonetwork/srv/dut/catalog.search#/metadata/ce00e887-19ef-497f-8582-02fb2f9db3c7.

RIVM (2025b). *Fijnstof 2022 (PM2,5)*. URL: https://nationaalgeoregister.nl/geonetwork/srv/dut/catalog.search#/metadata/68a93a15-8894-4c8b-a455-06cb2d029fe1/formatters/xsl-view?root=div&view=advanced.

— (2025c). *Luchtkwaliteit*. URL: https://www.rivm.nl/lucht.

— (2025d). *Stikstofdioxide 2022 (NO2)*. URL: https://nationaalgeoregister.nl/geonetwork/srv/dut/catalog.search#/metadata/43fe76cf-96c6-416c-8b7d-532936b46551/formatters/xsl-view?root=div&view=advanced.

Schatzmann, M. and B. Leitl (2011). "Issues with validation of urban flow and dispersion CFD models". In: *Journal of Wind Engineering and Industrial Aerodynamics* 99.4. The Fifth International Symposium on Computational Wind Engineering, pp. 169–186. ISSN: 0167-6105. DOI: https://doi.org/10.1016/j.jweia.2011.01.005.

Socolofsky, S. A. and G. H. Jirka (2002). *Environmental Fluid Mechanics Part I: Mass Transfer and Diffusion. Engineering - Lectures*. Institut für Hydromechanik, Universität Karlsruhe, pp. 23–25. URL: https://www.hailienene.com/resources/Environmental%20Fluid%20Mechanics%20Part%201.pdf.

Theeuwes, N. E. et al. (2014). "Seasonal dependence of the urban heat island on the street canyon aspect ratio". In: *Quarterly Journal of the Royal Meteorological Society* 140.684, pp. 2197–2210. DOI: https://doi.org/10.1002/qj.2289. eprint: https://rmets.onlinelibrary.wiley.com/doi/pdf/10.1002/qj.2289.

Tominaga, Y. and T. Stathopoulos (2007). "Turbulent Schmidt numbers for CFD analysis with various types of flowfield". In: *Atmospheric Environment* 41.37, pp. 8091–8099. ISSN: 1352-2310. DOI: https://doi.org/10.1016/j.atmosenv.2007.06.054.

United States Environmental Protection Agency (2024). *Benefits of Trees and Vegetation*. URL: https://www.epa.gov/heatislands/benefits-trees-and-vegetation.

Venderbos, J., K. Hosper, and T. van Loenen (2023). *Leefomgeving en gezondheidsverschillen*. Pharos. URL: https://www.pharos.nl/kennisbank/leefomgeving-en-gezondheidsverschillen/.

Vos, P. E. et al. (2013). "Improving local air quality in cities: To tree or not to tree?" In: *Environmental Pollution* 183. Selected Papers from Urban Environmental Pollution 2012, pp. 113–122. ISSN: 0269-7491. DOI: https://doi.org/10.1016/j.envpol.2012.10.021.

Vranckx, S. et al. (2015). "Impact of trees on pollutant dispersion in street canyons: A numerical study of the annual average effects in Antwerp, Belgium". In: *Science of The Total Environment* 532, pp. 474–483. ISSN: 0048-9697. DOI: https://doi.org/10.1016/j.scitotenv.2015.06.032.

Wang, Y. and H. Akbari (2016). "The effects of street tree planting on Urban Heat Island mitigation in Montreal". In: *Sustainable Cities and Society* 27, pp. 122–128. ISSN: 2210-6707. DOI: https://doi.org/10.1016/j.scs.2016.04.013.

Weichenthal, S. et al. (2022). "How low can you go? Air pollution affects mortality at very low levels". In: *ScienceAdvances* 8. DOI: https://doi.org/10.1126/sciadv.abo3381.

Xue, F. and X. Li (2017). "The impact of roadside trees on traffic released PM10 in urban street canyon: Aerodynamic and deposition effects". In: *Sustainable Cities and Society* 30, pp. 195–204. ISSN: 2210-6707. DOI: https://doi.org/10.1016/j.scs.2017.02.001.

A
Simulation names

Name	Description
single00parallel	180 m length, LAD 0.0, parallel
single02parallel	180 m length, LAD 0.2, parallel
single10parallel	180 m length, LAD 1.0, parallel
single22parallel	180 m length, LAD 2.2, parallel
single00angled	180 m length, LAD 0.0, angled
single02angled	180 m length, LAD 0.2, angled
single10angled	180 m length, LAD 1.0, angled
single22angled	180 m length, LAD 2.2, angled
single00perpendicular	180 m length, LAD 0.0, perpendicular
single02perpendicular	180 m length, LAD 0.2, perpendicular
single10perpendicular	180 m length, LAD 1.0, perpendicular
single22perpendicular	180 m length, LAD 2.2, perpendicular
double00parallel	360 m length, LAD 0.0, parallel
double02parallel	360 m length, LAD 0.2, parallel
double10parallel	360 m length, LAD 1.0, parallel
double22parallel	360 m length, LAD 2.2, parallel
double00angled	360 m length, LAD 0.0, angled
double02angled	360 m length, LAD 0.2, angled
double10angled	360 m length, LAD 1.0, angled
double22angled	360 m length, LAD 2.2, angled
double00perpendicular	360 m length, LAD 0.0, perpendicular
double02perpendicular	360 m length, LAD 0.2, perpendicular
double10perpendicular	360 m length, LAD 1.0, perpendicular
double22perpendicular	360 m length, LAD 2.2, perpendicular
triple00parallel	540 m length, LAD 0.0, parallel
triple02parallel	540 m length, LAD 0.2, parallel
triple10parallel	540 m length, LAD 1.0, parallel
triple22parallel	540 m length, LAD 2.2, parallel
triple00angled	540 m length, LAD 0.0, angled
triple02angled	540 m length, LAD 0.2, angled
triple10angled	540 m length, LAD 1.0, angled
triple22angled	540 m length, LAD 2.2, angled
triple00perpendicular	540 m length, LAD 0.0, perpendicular
triple02perpendicular	540 m length, LAD 0.2, perpendicular
triple10perpendicular	540 m length, LAD 1.0, perpendicular
triple22perpendicular	540 m length, LAD 2.2, perpendicular

Table A.1: Necessary simulations for sub-question 1.

B
Convergence

B.1. Residuals

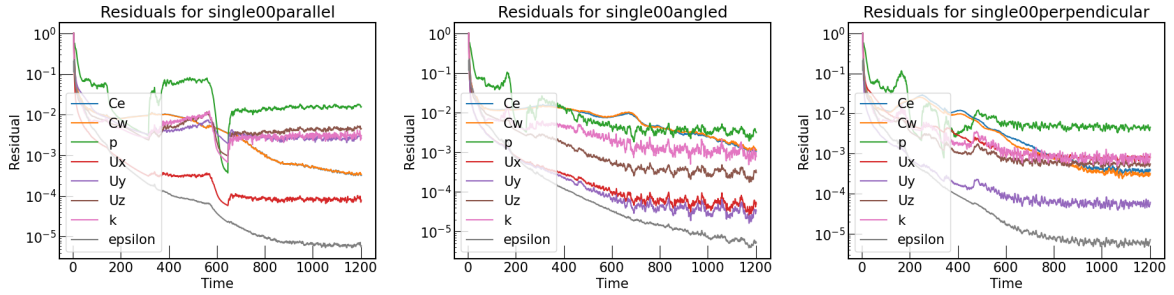

(a) parallel **(b)** angled **(c)** perpendicular

Figure B.1: Residuals for single-length and LAD=0.0 m^2/m^3

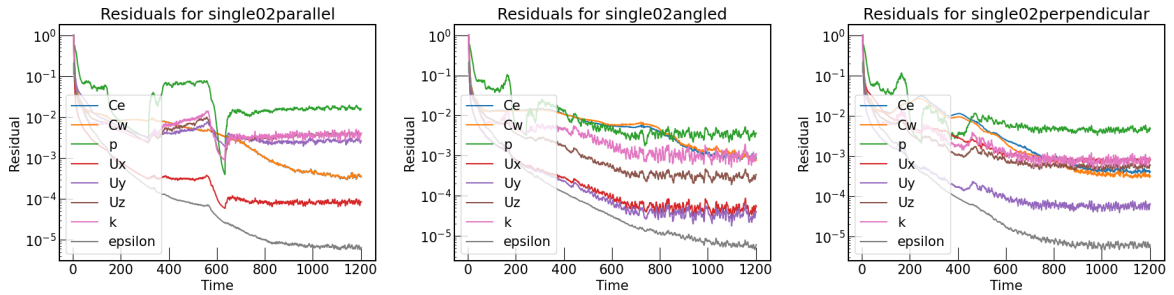

(a) parallel **(b)** angled **(c)** perpendicular

Figure B.2: Residuals for single-length and LAD=0.2 m^2/m^3

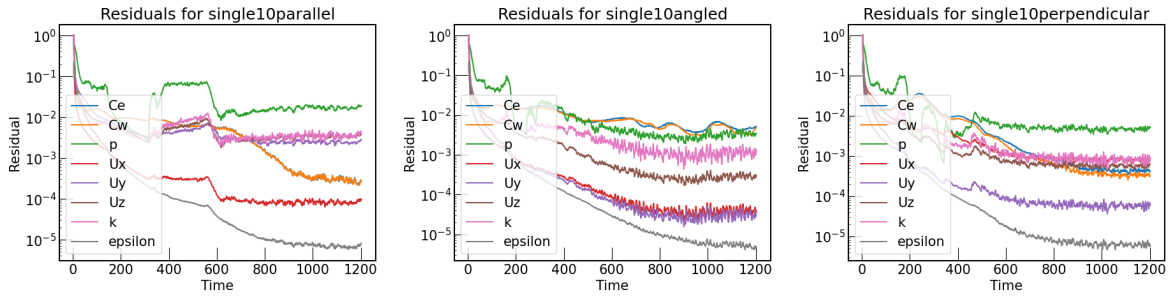

(a) parallel **(b)** angled **(c)** perpendicular

Figure B.3: Residuals for single-length and LAD=1.0 m^2/m^3

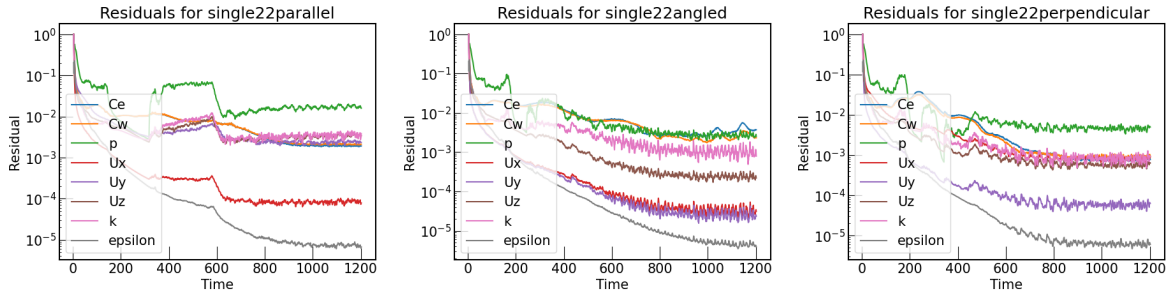

(a) parallel **(b)** angled **(c)** perpendicular

Figure B.4: Residuals for single-length and LAD=2.2 m^2/m^3

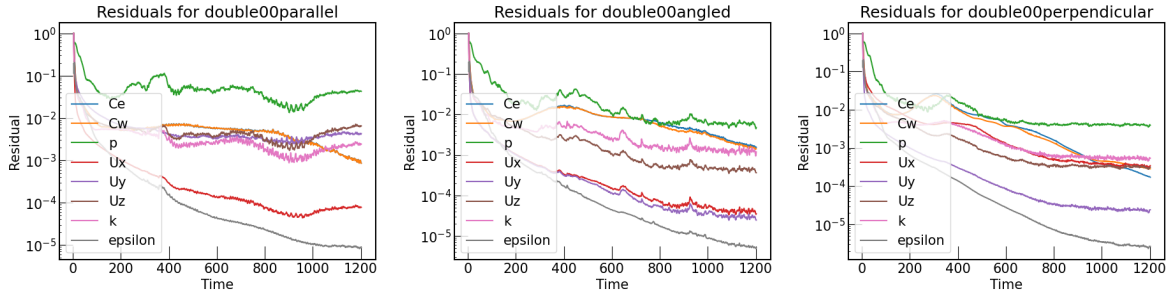

(a) parallel **(b)** angled **(c)** perpendicular

Figure B.5: Residuals for double-length and LAD=0.0 m^2/m^3

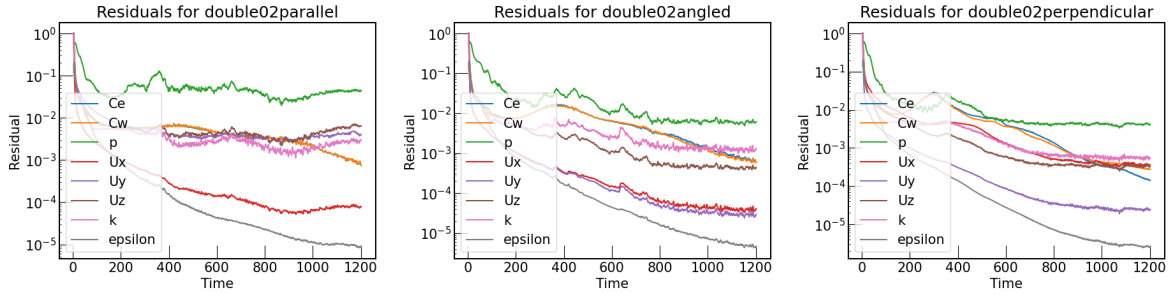

(a) parallel **(b)** angled **(c)** perpendicular

Figure B.6: Residuals for double-length and LAD=0.2 m^2/m^3

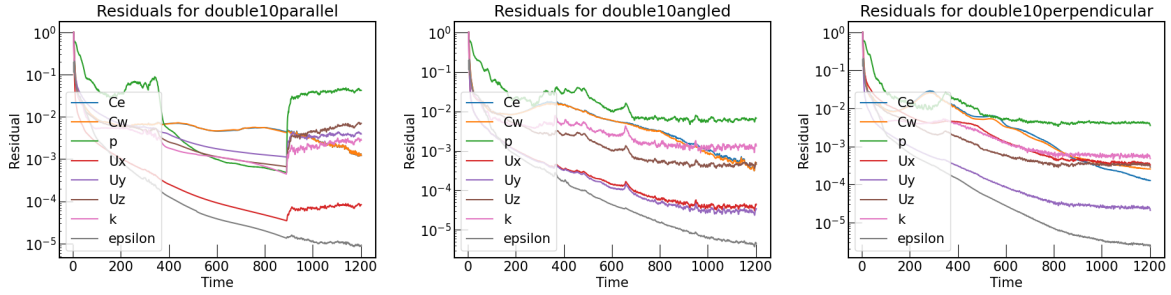

(a) parallel **(b)** angled **(c)** perpendicular

Figure B.7: Residuals for double-length and LAD=1.0 m^2/m^3

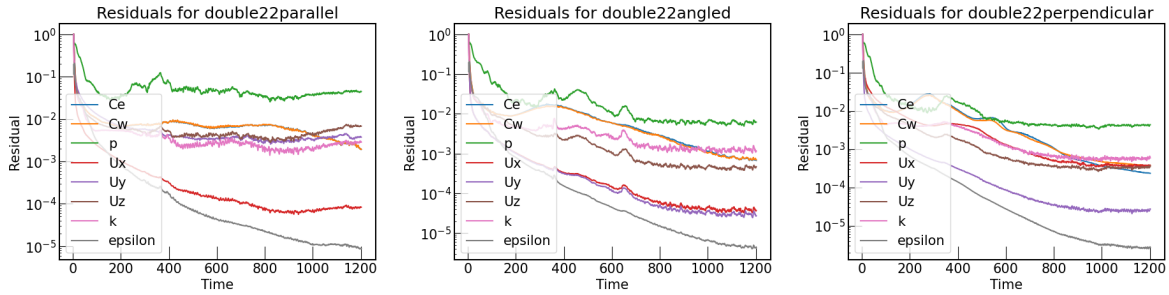

(a) parallel **(b)** angled **(c)** perpendicular

Figure B.8: Residuals for double-length and LAD=2.2 m^2/m^3

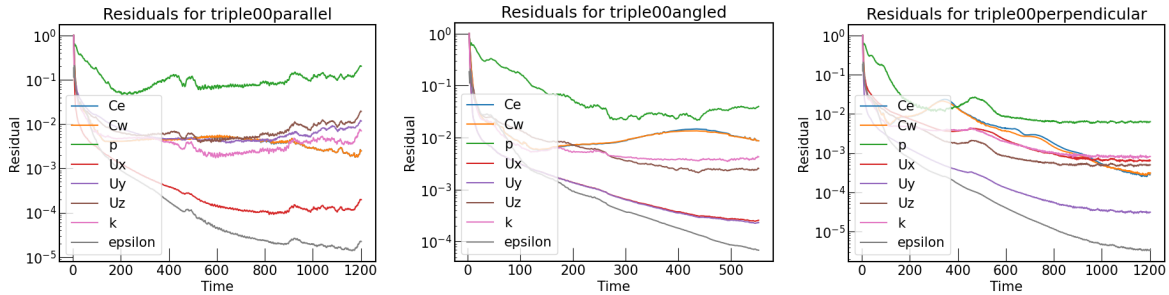

(a) parallel **(b)** angled **(c)** perpendicular

Figure B.9: Residuals for triple-length and LAD=0.0 m^2/m^3

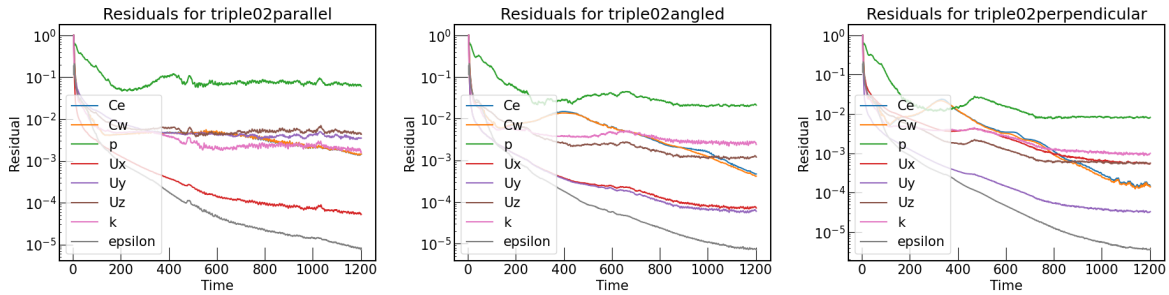

(a) parallel **(b)** angled **(c)** perpendicular

Figure B.10: Residuals for triple-length and LAD=0.2 m^2/m^3

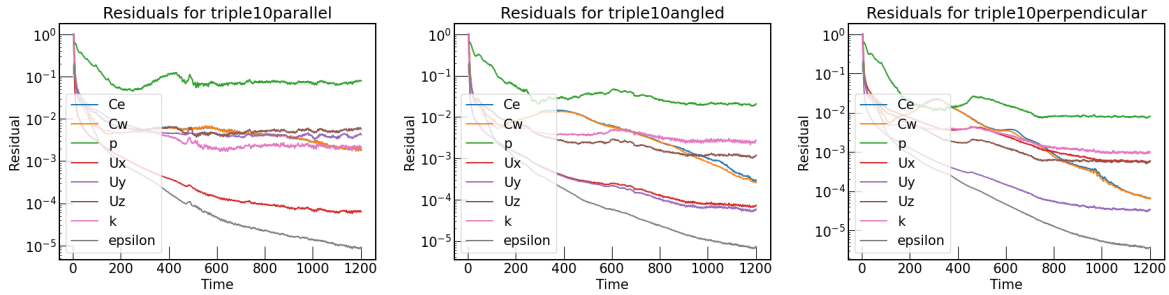

(a) parallel **(b)** angled **(c)** perpendicular

Figure B.11: Residuals for triple-length and LAD=1.0 m^2/m^3

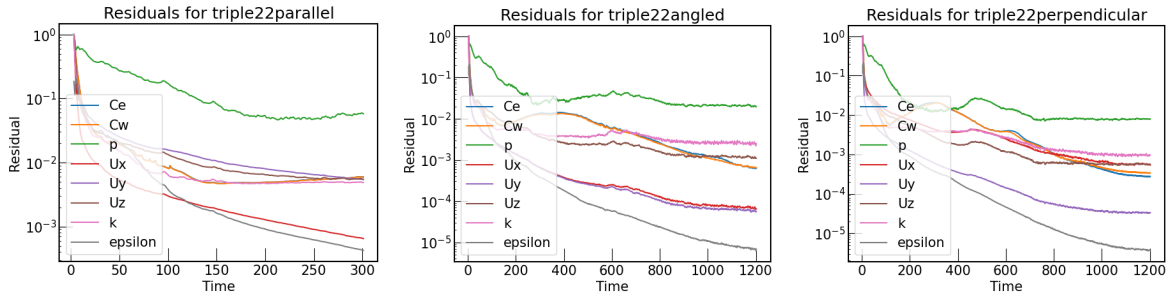

(a) parallel **(b)** angled **(c)** perpendicular

Figure B.12: Residuals for triple-length and LAD=2.2 m^2/m^3

B.2. Probes

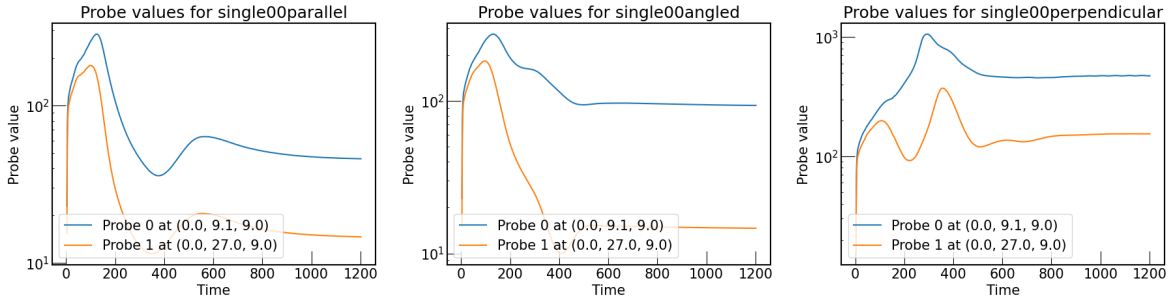

(a) parallel **(b)** angled **(c)** perpendicular

Figure B.13: Probes for single-length and LAD=0.0 m^2/m^3

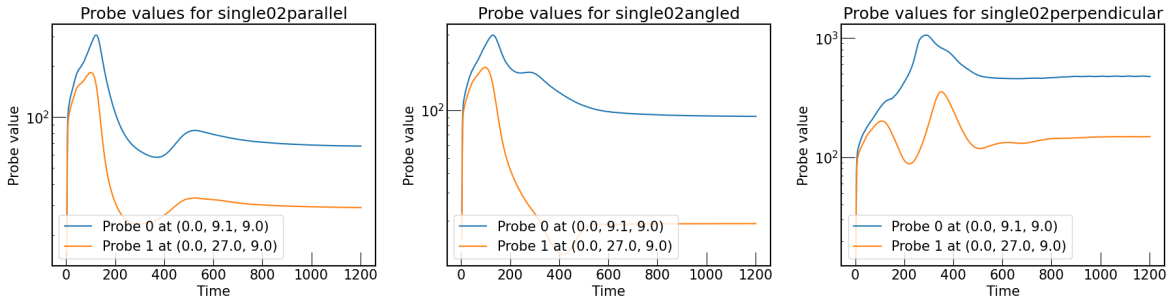

(a) parallel **(b)** angled **(c)** perpendicular

Figure B.14: Probes for single-length and LAD=0.2 m^2/m^3

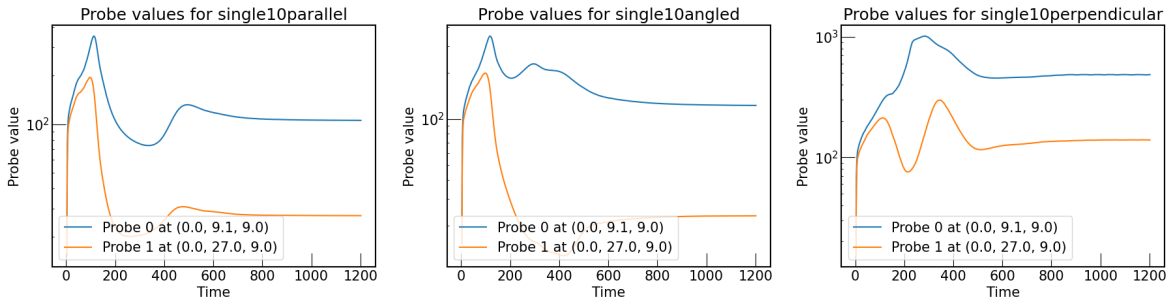

(a) parallel **(b)** angled **(c)** perpendicular

Figure B.15: Probes for single-length and LAD=1.0 m^2/m^3

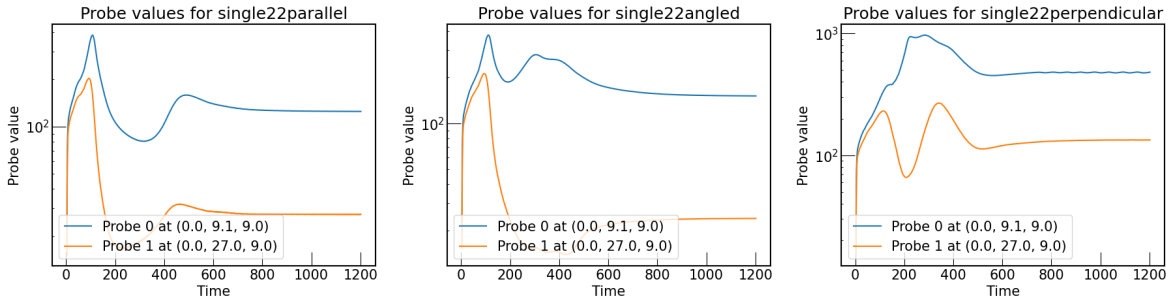

(a) parallel **(b)** angled **(c)** perpendicular

Figure B.16: Probes for single-length and LAD=2.2 m^2/m^3

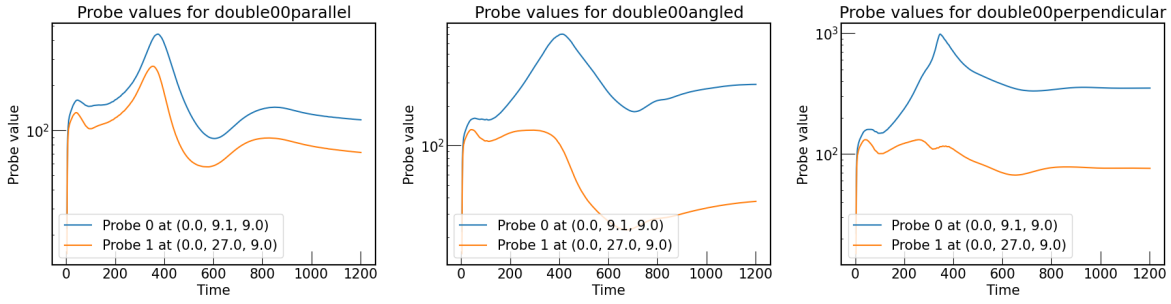

(a) parallel **(b)** angled **(c)** perpendicular

Figure B.17: Probes for double-length and LAD=0.0 m^2/m^3

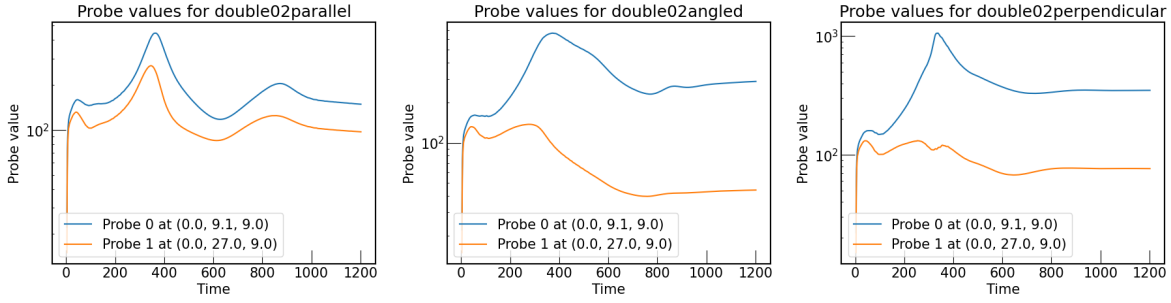

(a) parallel **(b)** angled **(c)** perpendicular

Figure B.18: Probes for double-length and LAD=0.2 m^2/m^3

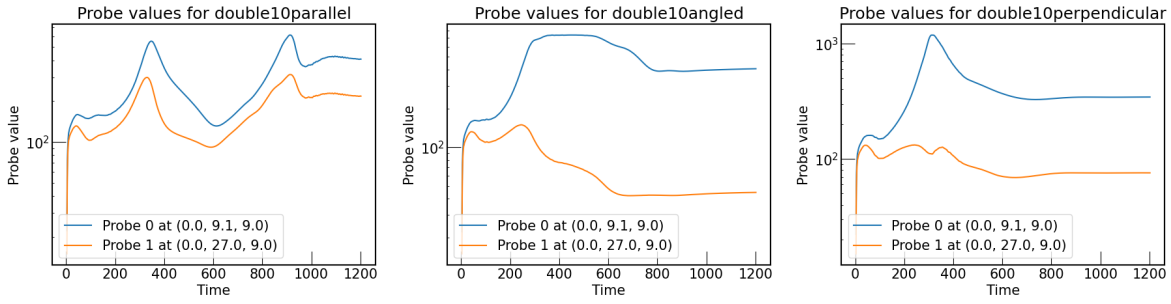

(a) parallel **(b)** angled **(c)** perpendicular

Figure B.19: Probes for double-length and LAD=1.0 m^2/m^3

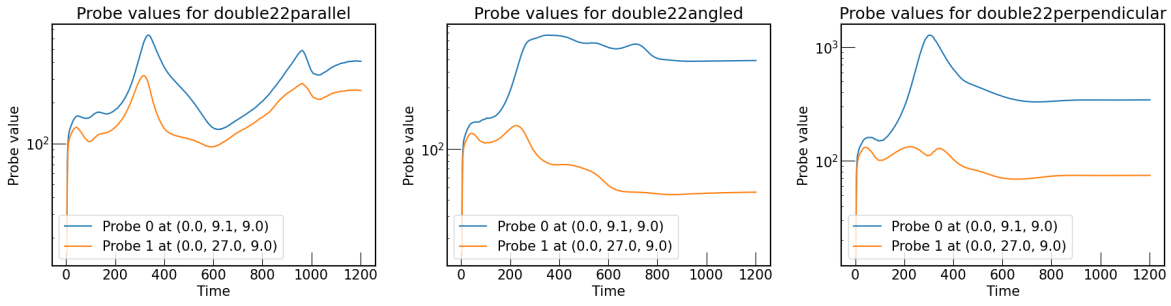

(a) parallel **(b)** angled **(c)** perpendicular

Figure B.20: Probes for double-length and LAD=2.2 m^2/m^3

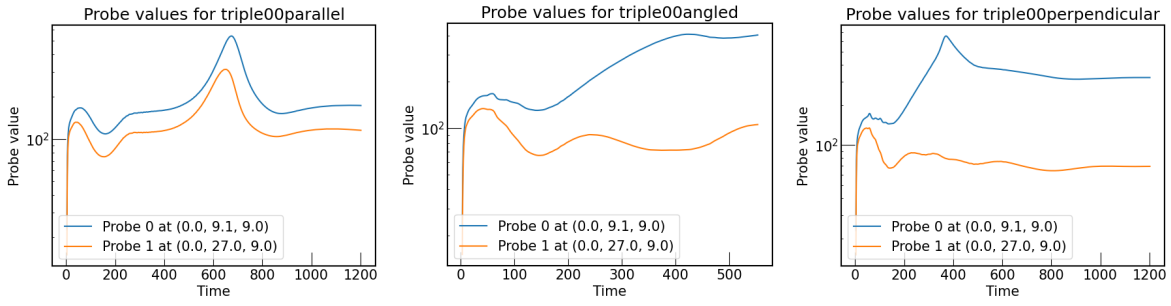

(a) parallel **(b)** angled **(c)** perpendicular

Figure B.21: Probes for triple-length and LAD=0.0 m^2/m^3

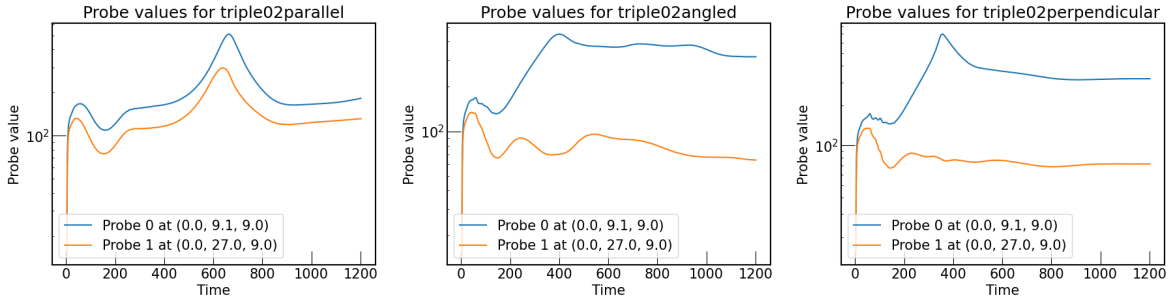

(a) parallel **(b)** angled **(c)** perpendicular

Figure B.22: Probes for triple-length and LAD=0.2 m^2/m^3

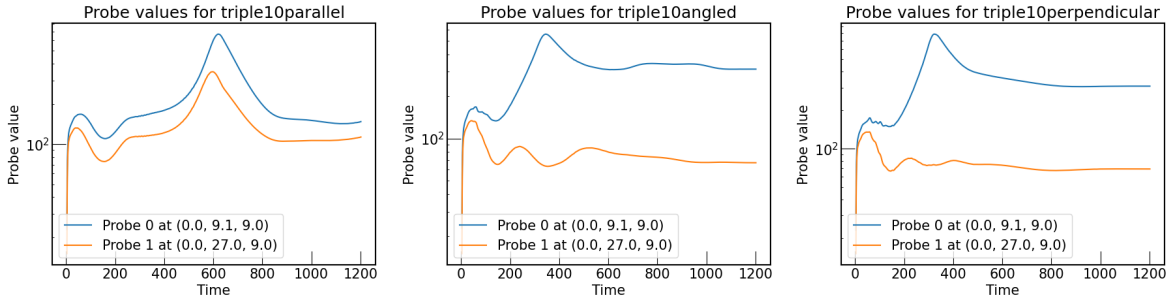

(a) parallel **(b)** angled **(c)** perpendicular

Figure B.23: Probes for triple-length and LAD=1.0 m^2/m^3

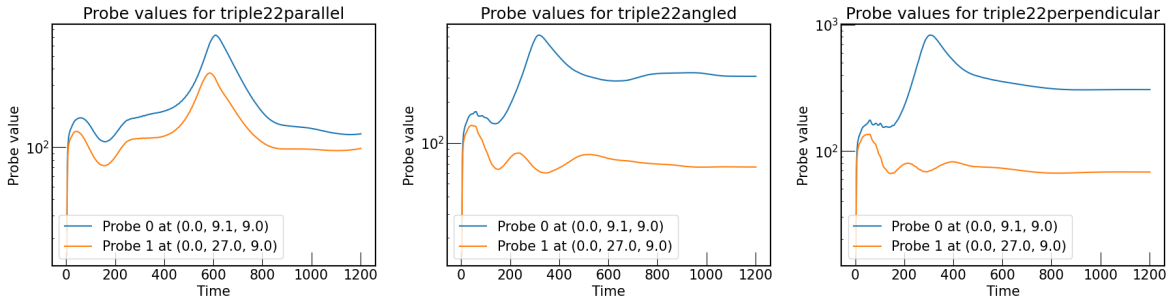

(a) parallel **(b)** angled **(c)** perpendicular

Figure B.24: Probes for triple-length and LAD=2.2 m^2/m^3

C
Seasonality plots

C.1. Mean C on facades at 2 m

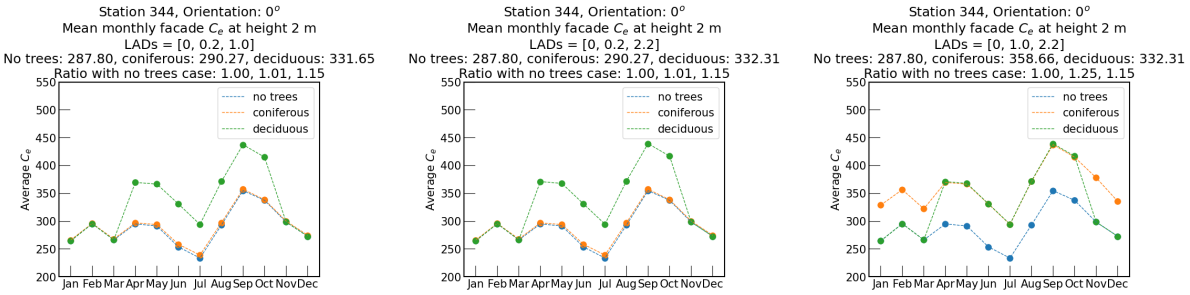

(a) 0 vs 0.2 vs 1.0 m^2/m^3 **(b)** 0 vs 0.2 vs 2.2 m^2/m^3 **(c)** 0 vs 1.0 vs 2.2 m^2/m^3

Figure C.1: Monthly average facade concentrations at 2 m for orientation 0° and different tree types

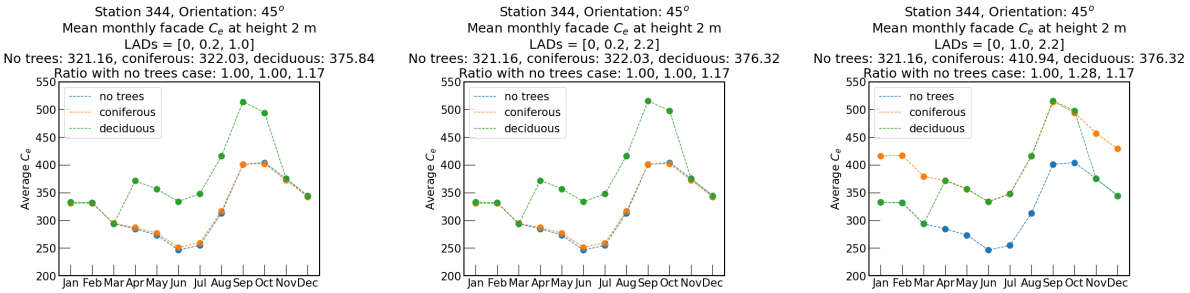

(a) 0 vs 0.2 vs 1.0 m^2/m^3 **(b)** 0 vs 0.2 vs 2.2 m^2/m^3 **(c)** 0 vs 1.0 vs 2.2 m^2/m^3

Figure C.2: Monthly average facade concentrations at 2 m for orientation 45° and different tree types

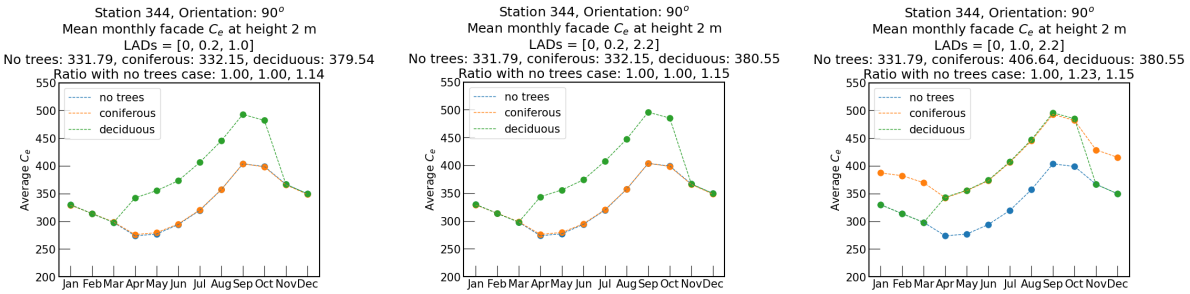

(a) 0 vs 0.2 vs 1.0 m^2/m^3 **(b)** 0 vs 0.2 vs 2.2 m^2/m^3 **(c)** 0 vs 1.0 vs 2.2 m^2/m^3

Figure C.3: Monthly average facade concentrations at 2 m for orientation 90° and different tree types

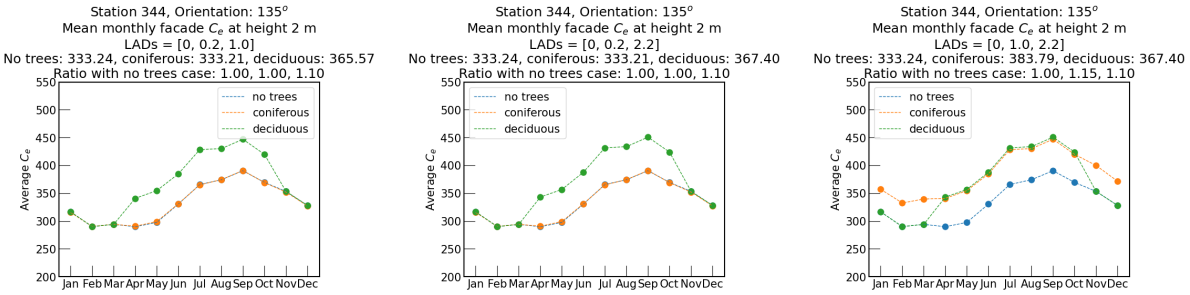

(a) 0 vs 0.2 vs 1.0 m^2/m^3 **(b)** 0 vs 0.2 vs 2.2 m^2/m^3 **(c)** 0 vs 1.0 vs 2.2 m^2/m^3

Figure C.4: Monthly average facade concentrations at 2 m for orientation 135° and different tree types

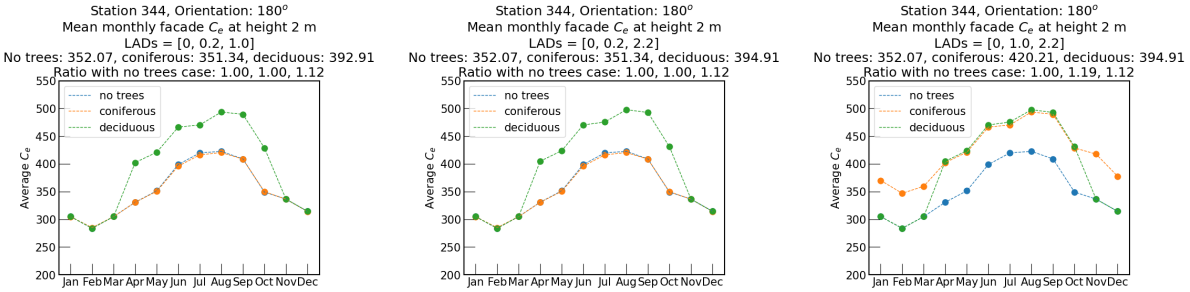

(a) 0 vs 0.2 vs 1.0 m^2/m^3 **(b)** 0 vs 0.2 vs 2.2 m^2/m^3 **(c)** 0 vs 1.0 vs 2.2 m^2/m^3

Figure C.5: Monthly average facade concentrations at 2 m for orientation 180° and different tree types

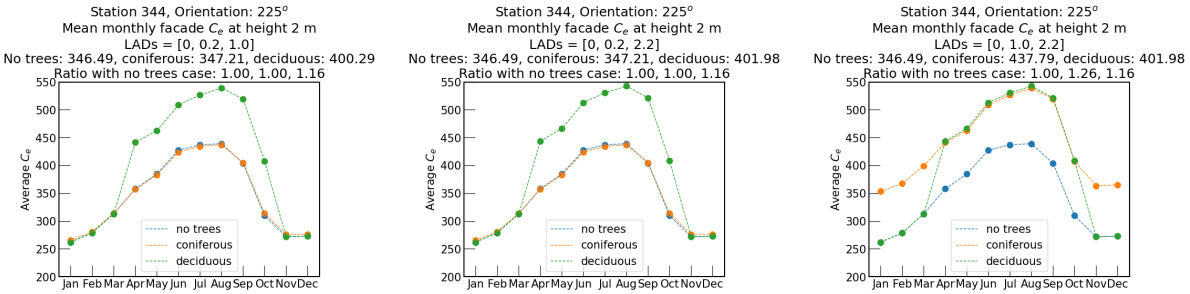

(a) 0 vs 0.2 vs 1.0 m^2/m^3 **(b)** 0 vs 0.2 vs 2.2 m^2/m^3 **(c)** 0 vs 1.0 vs 2.2 m^2/m^3

Figure C.6: Monthly average facade concentrations at 2 m for orientation 225° and different tree types

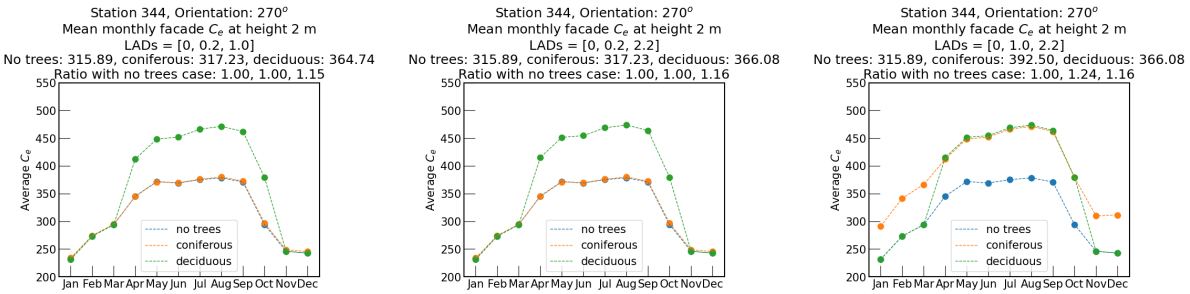

(a) 0 vs 0.2 vs 1.0 m^2/m^3 **(b)** 0 vs 0.2 vs 2.2 m^2/m^3 **(c)** 0 vs 1.0 vs 2.2 m^2/m^3

Figure C.7: Monthly average facade concentrations at 2 m for orientation 270° and different tree types

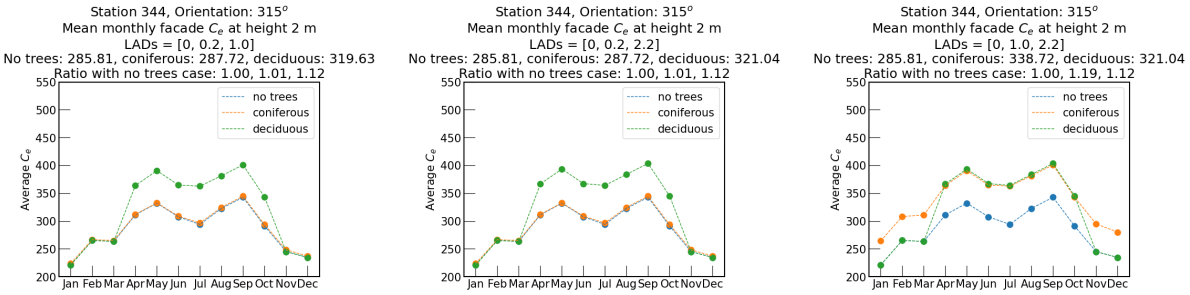

(a) 0 vs 0.2 vs 1.0 m^2/m^3 **(b)** 0 vs 0.2 vs 2.2 m^2/m^3 **(c)** 0 vs 1.0 vs 2.2 m^2/m^3

Figure C.8: Monthly average facade concentrations at 2 m for orientation 315° and different tree types

C.2. Mean C in canyon below 2 m

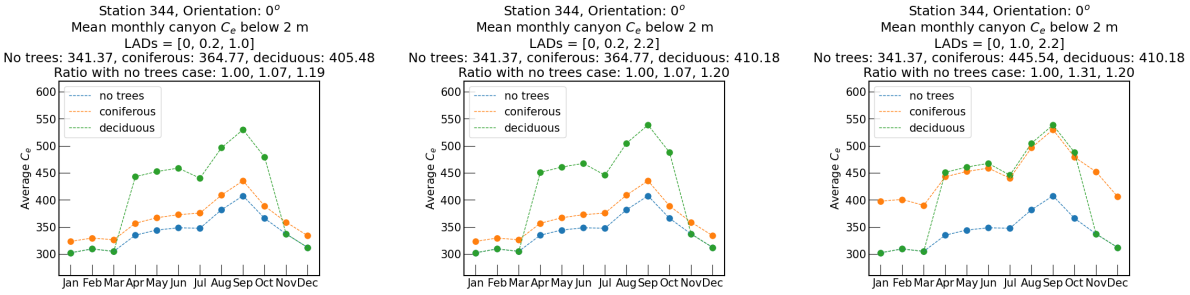

(a) 0 vs 0.2 vs 1.0 m^2/m^3 **(b)** 0 vs 0.2 vs 2.2 m^2/m^3 **(c)** 0 vs 1.0 vs 2.2 m^2/m^3

Figure C.9: Monthly average canyon concentrations below 2 m for orientation 0° and different tree types

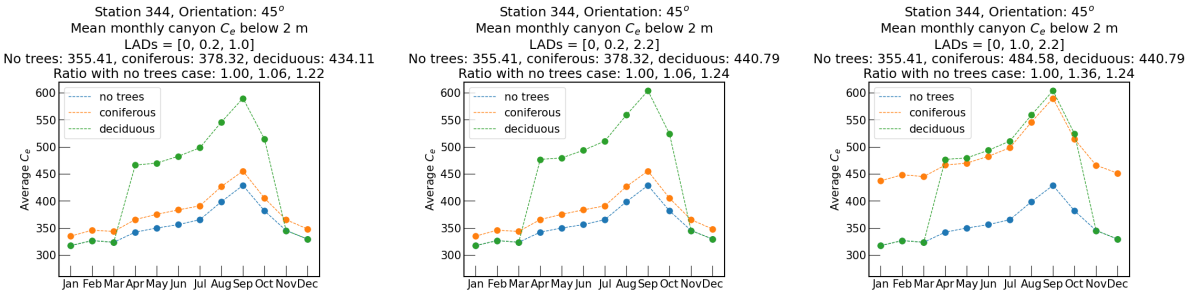

(a) 0 vs 0.2 vs 1.0 m^2/m^3 **(b)** 0 vs 0.2 vs 2.2 m^2/m^3 **(c)** 0 vs 1.0 vs 2.2 m^2/m^3

Figure C.10: Monthly average canyon concentrations below 2 m for orientation 45° and different tree types

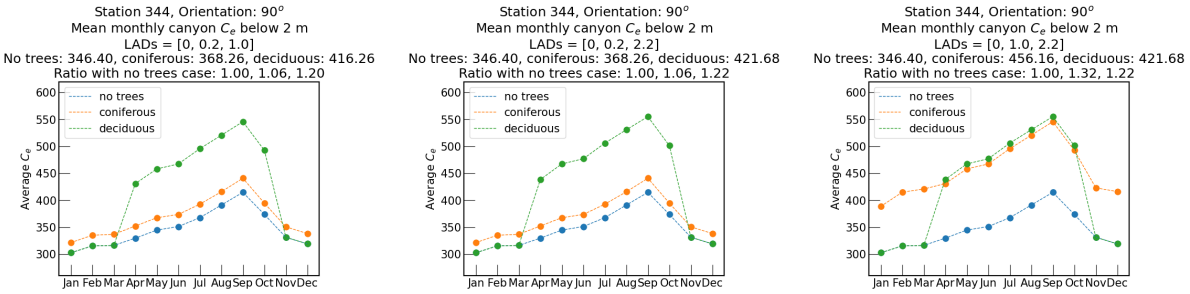

(a) 0 vs 0.2 vs 1.0 m^2/m^3 **(b)** 0 vs 0.2 vs 2.2 m^2/m^3 **(c)** 0 vs 1.0 vs 2.2 m^2/m^3

Figure C.11: Monthly average canyon concentrations below 2 m for orientation 90° and different tree types

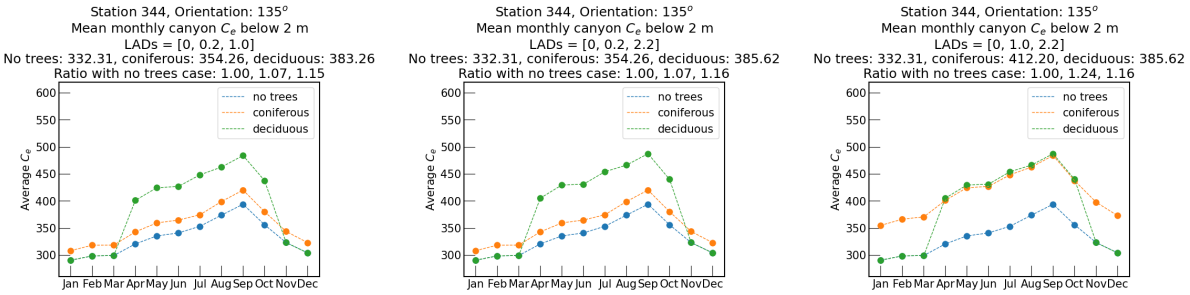

(a) 0 vs 0.2 vs 1.0 m^2/m^3 **(b)** 0 vs 0.2 vs 2.2 m^2/m^3 **(c)** 0 vs 1.0 vs 2.2 m^2/m^3

Figure C.12: Monthly average canyon concentrations below 2 m for orientation 135° and different tree types

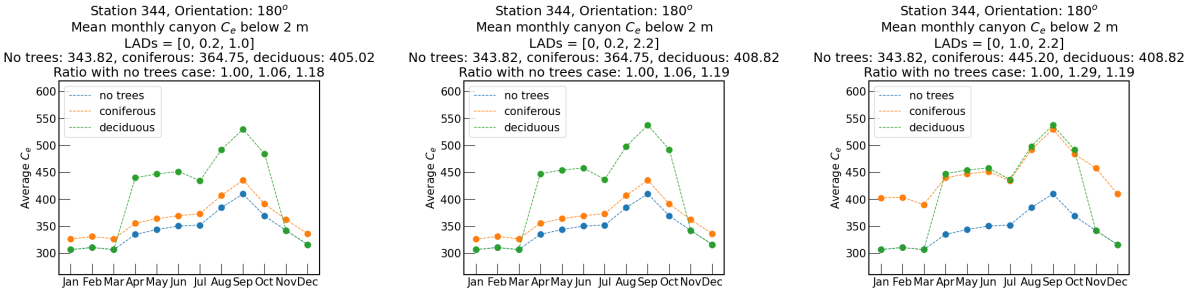

(a) 0 vs 0.2 vs 1.0 m^2/m^3 **(b)** 0 vs 0.2 vs 2.2 m^2/m^3 **(c)** 0 vs 1.0 vs 2.2 m^2/m^3

Figure C.13: Monthly average canyon concentrations below 2 m for orientation 180° and different tree types

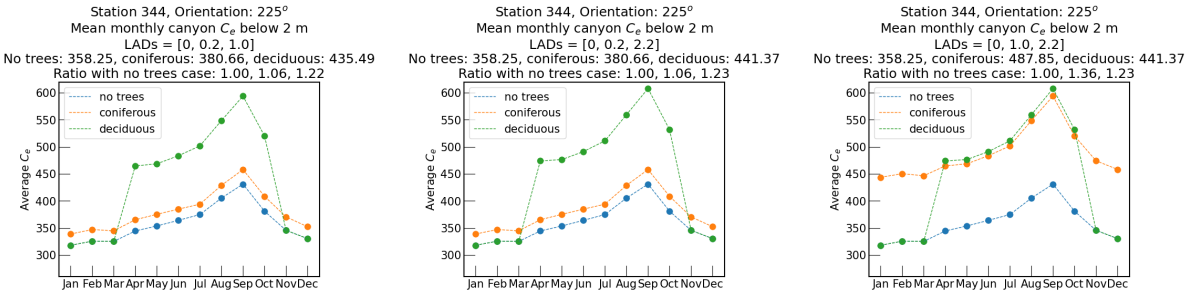

(a) 0 vs 0.2 vs 1.0 m^2/m^3 **(b)** 0 vs 0.2 vs 2.2 m^2/m^3 **(c)** 0 vs 1.0 vs 2.2 m^2/m^3

Figure C.14: Monthly average canyon concentrations below 2 m for orientation 225° and different tree types

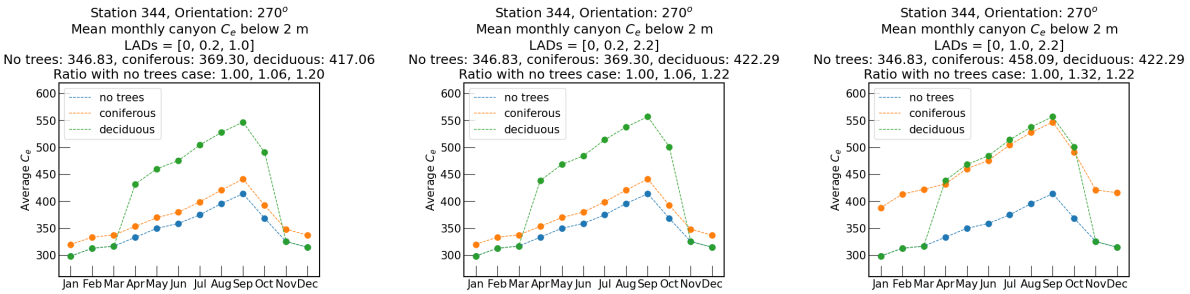

(a) 0 vs 0.2 vs 1.0 m^2/m^3 **(b)** 0 vs 0.2 vs 2.2 m^2/m^3 **(c)** 0 vs 1.0 vs 2.2 m^2/m^3

Figure C.15: Monthly average canyon concentrations below 2 m for orientation 270° and different tree types

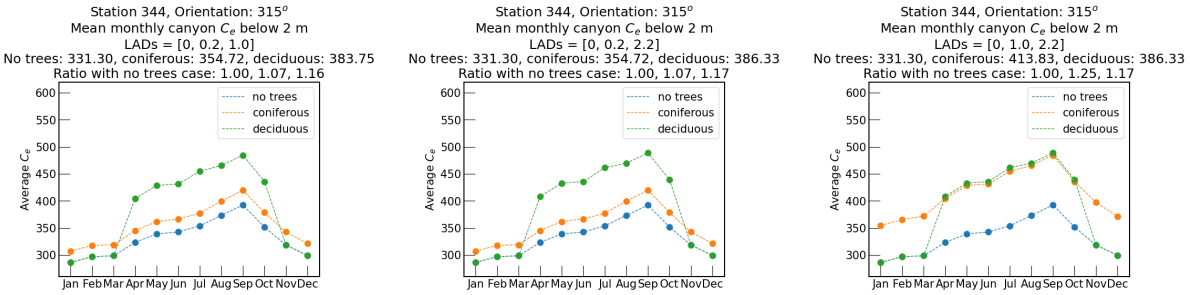

(a) 0 vs 0.2 vs 1.0 m^2/m^3 **(b)** 0 vs 0.2 vs 2.2 m^2/m^3 **(c)** 0 vs 1.0 vs 2.2 m^2/m^3

Figure C.16: Monthly average canyon concentrations below 2 m for orientation 315° and different tree types

D

Extra info for figures

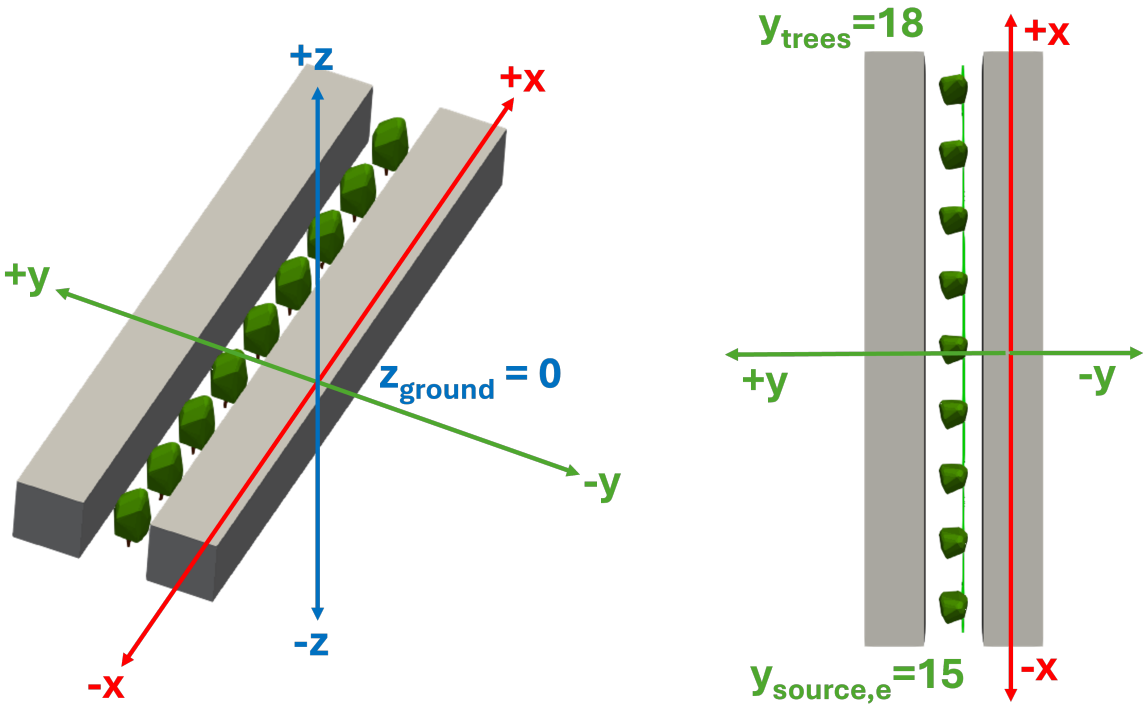

Figure D.1: The north-south direction aligns with the x-axis, and the east-west direction with the y-axis

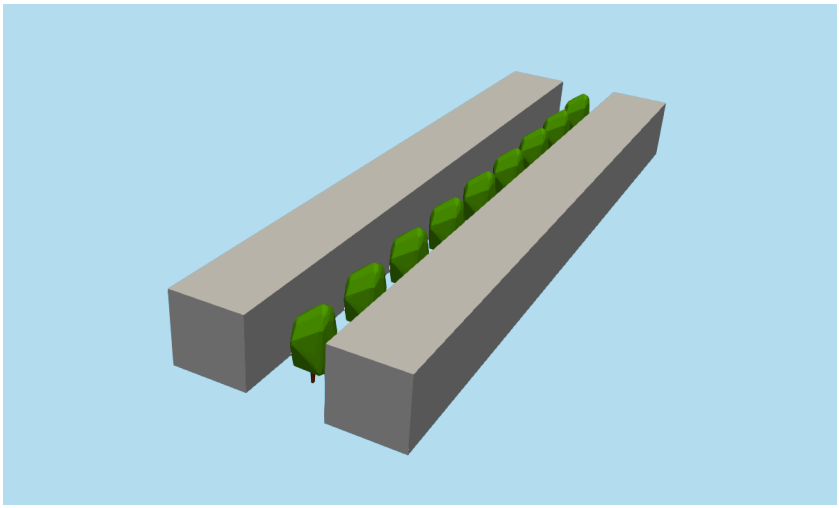

Figure D.2: The xy-plane is the plane for $z = 0$ (ground level)

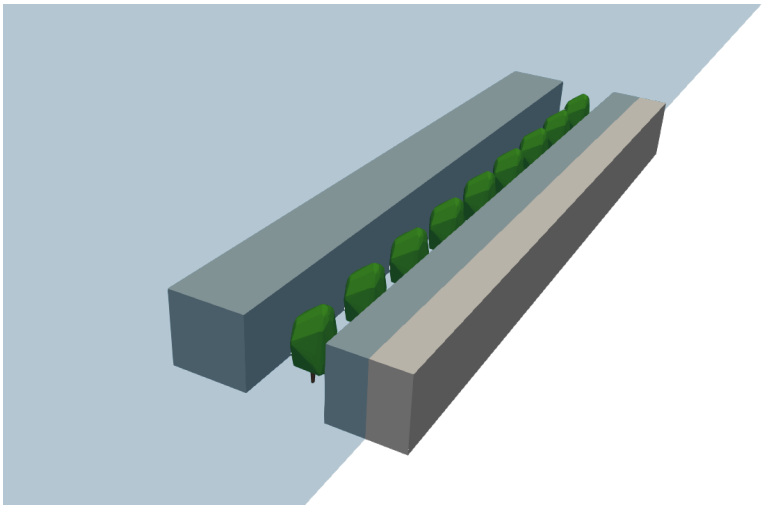

Figure D.3: The xz-plane is the plane for $y = 0$

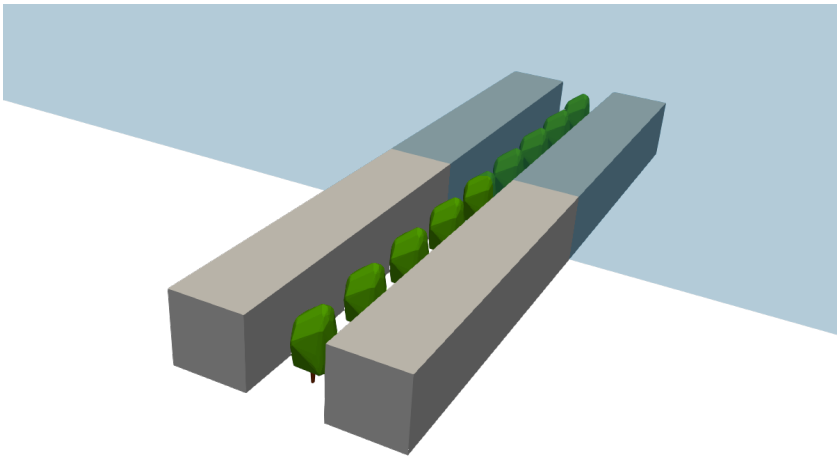

Figure D.4: The yz-plane is the plane for $x = 0$